新制
工
1183

Control of Interface Properties in ZnSe-GaAs Heterovalent Heterostructures Grown by Metalorganic Vapor Phase Epitaxy

Mitsuru FUNATO

December 1999

Control of Interface Properties in ZnSe-GaAs Heterovalent Heterostructures Grown by Metalorganic Vapor Phase Epitaxy

Mitsuru FUNATO

December 1999

Abstract

Heterovalent heterostructures, where different materials with different valency such as II-VI ZnSe and III-V GaAs are joined together, have possibilities to show novel characteristics never achieved with the conventional isovalent heterostructures such as an AlGaAs-GaAs system. This is due to electron-excess and electron-deficient bonds at the interface. Those nonoctet bonds form electronic dipoles, which play an important role in determining the interface properties. Therefore, if the strength and direction of the electronic dipoles can be tuned in some way, that may lead to the controllability of the interface properties. In this study, aiming at exploring the potential of the heterovalent heterostructures, their growth processes during metalorganic vapor phase epitaxy (MOVPE) and the controllability of the interface properties were investigated. As the constituents of the heterovalent heterostructure, we selected ZnSe and GaAs because this combination satisfies nearly perfect lattice matching and is suitable to concentrate the discussion on heterovalency.

In the MOVPE growth of ZnSe-on-GaAs heterostructures, it was found that the growth of ZnSe on an atomically flat GaAs surface was in either the two-dimensional (2D) or the three-dimensional (3D) mode, depending chiefly on the growth temperature. In particular, when the growth temperature was 450°C, the ZnSe surface became atomically flat. The initial nucleation processes at this growth temperature depended on the source precursor starting the ZnSe growth, although the 2D growth could be maintained regardless of the starting precursors. This 2D growth characteristic is quite favorable for the atomic level control of the interface and was utilized for the control of the interface properties.

As the controllability of the interface properties, we concentrated in this study on that of the band offsets because the band offsets determine the interface properties such as carrier transport and confinement important for heterostructure devices. In ZnSe-on-GaAs, the band offsets were successfully tuned by controlling the flow sequence of the source precursors at the interface; the valence band offset was 0.6 eV when the growth was initiated by the Se precursor, while that increased toward 1.1 eV as the Zn-exposure duration in the Zn-initiated growth. This is considerably different from the situation in the isovalent heterostructures where the band offset has been considered to be constant for a given heterostructure. The interface was investigated structurally and optically, and it was proved that the interfacial electronic dipoles originating from the electron-excess and

electron-deficient bonds played a crucial role in the control of the band offsets.

In the MOVPE of the inverse heterostructure, that is, GaAs-on-ZnSe, the flow sequences of the source precursors at the interfaces were, first, optimized, and then, the growth characteristics were clarified. One of the most important results obtained here is that the As precursor etches the ZnSe surface, which provides a possibility in controlling the interface atomic configuration, and hence, the band offsets. The growth mode of GaAs on ZnSe strongly depended on growth conditions and was explained well in terms of migration of Ga. Under the condition enhancing the migration, the growth was in the 3D Volmer-Weber mode, while by suppressing the migration, the growth tended to be two-dimensional in the atomic level. The 2D growth mode was used for the atomic level control of the interface.

For the control of the band offsets in GaAs-on-ZnSe, the properties that ZnSe is etched in a hydrogen ambient and, more drastically, in an As precursor ambient were applied. By changing the etching durations, the valence band offsets could be tuned between 0.6 and 1.1 eV. As the mechanism behind it, the interface atomic configuration was considered to be controlled precisely with the assistance of the layer-by-layer manner of the etching, by which Zn and Se atoms appear alternately on ZnSe. The surface of GaAs-on-ZnSe maintained atomically flat during the experiment supported this consideration.

Finally, all the above results were summarized in ZnSe-GaAs multilayered quantum structures. Namely, the structurally well-defined quantum structures were fabricated, in which the band offsets on both sides of GaAs wells were designed independently, and were characterized by optical-absorption measurements. As a result, it was found that the absorption edges were shifted toward lower energies by enlarging the difference of the valence band offsets at both sides of the GaAs wells. This is a quite unique characteristic originating from heterovalency, and never realized by the conventional isovalent quantum structures. The cause for the observed redshift was attributed to the electric field induced by the difference of the valence band offsets, which was supported by theoretical analyses. On the other hand, the barrier width dependence could not be explained theoretically and was interpreted well by considering the charge transfer within the ZnSe barrier region. In any cases, the obtained results indicate the capability of controlling the optical properties in a quantum structure without changing its structure and imply tremendous increase of flexibility in device design.

Acknowledgments

The author wishes to express his sincere gratitude to Professor Shigeo Fujita for his continuous guidance, supervision, and fruitful discussions throughout this work. The author acknowledges Professor Hiroyuki Matsunami and Professor Kazumi Matsushige for their critical reading of the manuscript and valuable comments.

The author is deeply indebted to Associate Professor Shizuo Fujita for his stimulating discussions, continuous encouragement throughout this work, and the critical reading of the manuscript. The author is also grateful to Associate Professor Yoichi Kawakami for his helpful suggestions and comments on this study.

He is also very much obliged to Professor Yoshikazu Takeda, Associate Professor Yasufumi Fujiwara, and Lecturer Masao Tabuchi at Nagoya University for their collaborations and stimulating discussions on the characterization of ZnSe/GaAs interfaces.

Thanks are due to all members of Fujita Laboratory. In particular, he expresses great appreciation to Mr. Masahiro Ishii, Mr. Daisuke Hanaoka, Mr. Gaku Sugahara, Mr. Tomokazu Nakamura, Mr. Masao Mikamo, Mr. Hiroaki Kitani, Mr. Satoshi Aoki, Mr. Hiroyuki Tachibana, and Mr. Taichi Ikuma for their collaborations: Mr. M. Ishii characterized ZnSe/GaAs heterointerfaces electrically. Mr. D. Hanaoka, Mr. M. Mikamo, and Mr. H. Kitani studied n-Zn(S)Se/p^+-GaAs and n-Zn(S)Se/n-GaAs heterojunctions. Mr. G. Sugahara, Mr. H. Tachibana, and Mr. T. Ikuma performed optical-absorption measurements of ZnSe-GaAs quantum structures. Mr. T. Nakamura conducted electrical characterization of p^+-GaAs/n-ZnSe diodes. Mr. S. Aoki studied surface structures and controllability of the band offsets in ZnSe/GaAs and GaAs/ZnSe heterostructures.

Experiments were partially assisted by facilities of Sasaki Laboratory (presently Quantum Optoelectronics Laboratory), Matsunami Laboratory, Yamada Laboratory, and Kyoto University Venture Business Laboratory.

This work was financially supported in part by the Ministry of Education, Science, Sports and Culture, and also by the Murata Science Foundation, the Nippon Sheet Glass Foundation for Materials Science, the Casio Science Promotion Foundation, the Mazda Foundation, and the Ozawa and Yoshikawa Memorial Electronics Research Foundation.

Finally, the author really thanks his parents and wife for their understanding, support, and warm encouragement.

This thesis is based on the research work to which the author devoted himself at

KYOTO UNIVERSITY,

DEPARTMENT of ELECTRONIC SCIENCE and ENGINEERING.

Contents

1 Introduction **1**

2 MOVPE Growth of ZnSe on GaAs **11**

2.1 Introduction 11

2.2 MOVPE Growth 12

2.3 Preparation of GaAs Surfaces 14

2.4 Nucleation Processes of ZnSe on GaAs 17

2.4.1 Rate-limiting steps 17

2.4.2 Effects of growth parameters 20

2.4.3 Initial nucleation processes 24

2.4.4 Nucleation processes during quasi-homoepitaxial growth 32

2.5 Post-Growth Annealing 34

2.6 Summary 35

3 Control of Interface Properties in ZnSe-on-GaAs Heterovalent Heterostructures **39**

3.1 Introduction 39

3.2 Preparation of ZnSe/GaAs Heterointerfaces 40

3.3 Control of Band Offsets 41

3.3.1 XPS measurements 41

3.3.2 Heterojunction diodes 49

3.4 Interface Structures 52

3.5 Electric Field at the Interface 61

3.6 Summary 67

4 **MOVPE Growth of GaAs on ZnSe** **71**
4.1 Introduction 71
4.2 Flow Sequence of GaAs Source Precursors at the Interface 72
4.2.1 Ga precursor 73
4.2.2 As precursor 74
4.2.3 Surface morphology of GaAs on ZnSe 78
4.3 Growth Mechanism of GaAs on ZnSe 80
4.3.1 Growth mode 80
4.3.2 Initial growth rate 87
4.4 Nucleation Processes of GaAs on ZnSe 89
4.4.1 Two-dimensional growth 89
4.4.2 Three-dimensional growth 91
4.5 Application to Low Dimensional Structures 94
4.6 Summary 96

5 **Control of Interface Properties in GaAs-on-ZnSe Heterovalent Heterostructures** **99**
5.1 Introduction 99
5.2 Preparation of GaAs/ZnSe Heterointerfaces 100
5.3 Control of Band Offsets 101
5.3.1 XPS measurements 101
5.3.2 Effects of interval duration 102
5.3.3 Effects of As exposure duration 106
5.4 Summary 109

6 **Quantum Structures with Engineered Interface Properties** **111**
6.1 Introduction 111
6.2 Fabrication of ZnSe-GaAs Quantum Structures 112
6.3 Structural Properties 117
6.3.1 Surface morphology 117
6.3.2 Crystalline properties 117
6.4 Optical-Absorption Properties 119
6.4.1 Theoretical backgrounds 119

6.4.2 Optical-absorption measurements 127
6.5 Summary 134

7 Conclusions 137

Appendix 141

Addendum 143

Chapter 1

Introduction

Semiconductor heterostructures, where different materials are joined together, are a fundamental structure in the field of (opto)electronic devices. Devices such as quantum well lasers, light emitting diodes, and heterojunction bipolar transistors, which already arise a significant technological impact, cannot be realized without the heterostructures. So far, these devices have been fabricated using the material combinations such as GaAs-AlGaAs and InGaP-InGaAlP [1]. The reason why such heterostructures are widely utilized is that those satisfy "matching" in lattice parameters and chemical valency as shown in Fig. 1.1. Here, chemical valence matching, *i.e.*, isovalency, denotes that the constituent materials of a heterostructure belong to the same group such as III-V, IV, and II-VI. The lattice matching and isovalency have been regarded to be of first-order importance to obtain the heterostructure with high crystalline quality, low interface state density, and abrupt interfaces, because generation of dislocations and dangling bonds are effectively avoided by lattice matching and valence matching, respectively. At the same time, however, the matching may be a limit for material combinations and, thus, for device performances to be realized.

In order to break through the limit, recently, mismatch epitaxy attains an increasing interest. "Lattice mismatch" heteroepitaxy with "isovalent" materials is extensively studied as a novel approach to fabricate quantum dot structures. A representative heterostructure is an InAs-GaAs system, which includes large strain due to the lattice mismatch (see Fig. 1.1). Heteroepitaxy accommodating strain generally exhibits three-dimensional (3D) growth during strain release processes. For devices with two-dimensional layered structures, 3D growth should be avoided, although, from a different viewpoint, it has been found that the 3D islands work as quantum dots [2-4]. An advantage of the use of the self-formed 3D

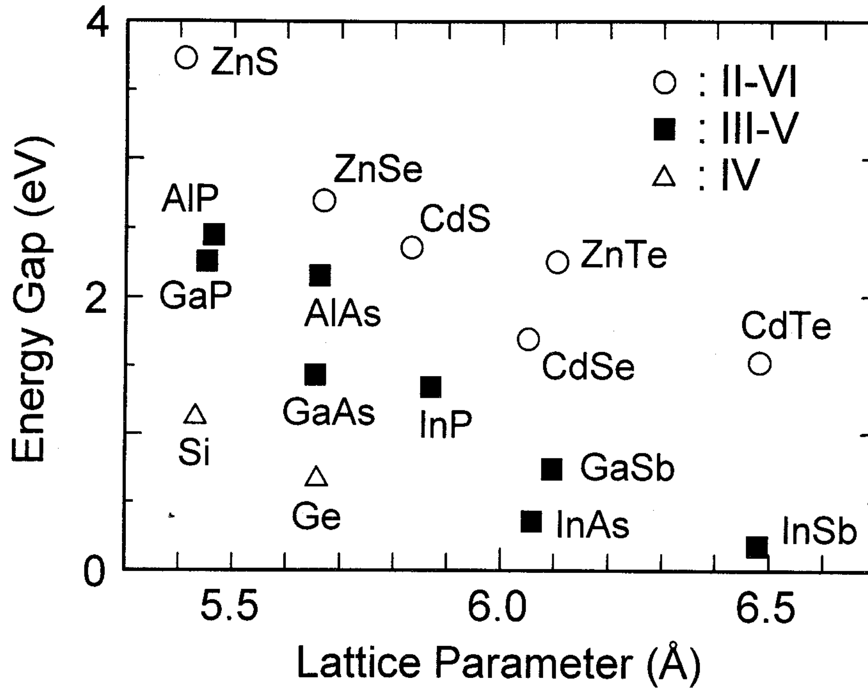

Figure 1.1: Relation between lattice parameters and energy gaps for various semiconductors at room temperature.

islands is that this procedure does not require any *ex situ* processes such as lithography and etching, which makes the crystalline quality of the quantum dots equivalent to that of their bulk crystal. Although control and uniformity of the dot size are the remaining issues to be solved, this is one of the potential applications of the mismatch epitaxy.

On the other hand, in this work, we shall note frontier of "heterovalent" heteroepitaxy. Owing to large tolerance of material combination, the heterovalent heterostructures may provide large band discontinuities and large differences in the dielectric constant, which is expected to lead to novel devices as well as improvement of device performances. Recently, several theoretical analyses have shown interesting properties and potential applications of the heterovalent heterostructures [5-8]. Kumagai and Takagahara [5] proposed a dielectric quantum well (QW) in which the large difference in the dielectric constants between the well and barrier layers is positively utilized to enhance exciton binding energy. They introduced a ZnSe-GaAs QW as one of the realistic examples, where ZnSe acts as a barrier layer. Compared with the dielectric constant of Al(Ga)As in the Al(Ga)As-GaAs isovalent QW, that of the ZnSe barrier layer is smaller, which makes the exciton binding energy larger. For example, when the GaAs well width is 50 Å, the exciton binding energy was calculated to

be 24 meV for the ZnSe-GaAs QW, while 14 meV for the $Al_{0.3}Ga_{0.7}As$-GaAs QW. Khurgin [6] revealed that the nonlinear and electrooptic coefficients of ZnSe-GaAs heterostructures are substantially larger than those in conventional materials such as AlGaAs-GaAs heterostructures; the second harmonic generation (SHG) coefficient and the Pockels coefficient of the ZnSe-GaAs asymmetric coupled QW's were calculated to be eight times and twice as large as those of the $Al_{0.4}Ga_{0.6}As$-GaAs system, respectively. This is due to the larger band offset in the ZnSe-GaAs heterostructures. Yu and McGill [7] have predicted theoretically that (II-VI)-(III-V) double-barrier resonant tunneling structures can be faster and can possess greater peak-to-valley ratios than AlGaAs-GaAs tunnel structures. In the ZnSe-GaAs system, the increase in speed is expected. This is because the capacitance, and therefore the RC time constant, which is a parameter relevant to the device speed, should be reduced by replacing AlGaAs with ZnSe owing to the smaller dielectric constant in ZnSe than in AlGaAs (9.1 vs. 12.0). In the ZnTe-InAs system, on the other hand, the increase in speed is due to the small dielectric constant in ZnTe (10.4) and, in addition, the higher mobility in InAs than in GaAs [33000 vs. 8500 cm^2/Vs at 300 K]. Furthermore, the larger peak-to-valley ratio due to the larger conduction band offset was predicted ($\sim$1700 for ZnTe-InAs vs. 92 for AlGaAs-GaAs). Morrison *et al.* have proposed a ZnTe-InAs QW as a novel structure which could realize the large nonlinear optical susceptibility in the third-order tensor $\chi^{(3)}$. They pointed out that $\chi^{(3)}$ is greatly enhanced when the separation of the lowest two conduction minibands is comparable to the magnitude of the principal gap. This condition is never fulfilled in the GaAs-AlGaAs system but is satisfied in the ZnTe-InAs system by utilizing the large difference in their band gap energies.

The examples shown above place their basis on the large difference in the physical parameters of the constituents. Another important characteristic of the heterovalent heterostructures is the formation of electron-excess and electron-deficient chemical bonds at the interfaces. For instance, the electronic structures of the ZnSe-GaAs superlattices have theoretically been investigated and revealed to be considerably different from the isovalent superlattices owing to the presence of the donating Ga-Se and accepting Zn-As bonds [9-12]. Eppenga found in the process of the first-principle calculation of the band offsets that the ZnSe-GaAs superlattice grown on the polar (001) plane with alternating deposition of the Ga-Se interface and the Zn-As interface contains an electric field, while that on the nonpolar (110) plane does not [11]; though the difference in the layer ionicity of ZnSe and GaAs

as well as nonoctet bonds plays a role in determining the electronic structures. According to the calculation of Oda and Nakayama based on the semiempirical sp^3s^* tight-binding method [12], the band gap energy of the ZnSe-GaAs superlattice grown along the [001] direction changes largely (~0.3 eV) with varying configuration of Ga-Se donor and Zn-As acceptor bonds at the interfaces. In contrast, in the isovalent AlAs-GaAs superlattices, there is little variation of the band gap energy due to interface atomic configurations.

As a practically more important feature, the capability of controlling the band offsets must be pointed out. Although the band offset, which determines the carrier transport and confinement properties in the heterostructures, has been recognized to be an intrinsic property for a given heterostructure, a number of recent works revealed that it depends on the interface properties [13-23]. In the case of the isovalent heterostructures, however, the variation of the band offset is small in principle. Theoretical studies showed that, for example, the valence band offsets in InAs/GaSb(001) heterostructures differ by only 0.15 eV with different interface compositions [13]. In contrast, the heterovalent heterostructures have been theoretically predicted to show large variations of the band offsets, *e.g.*, 1.0, 0.6, and 0.8 eV for ZnSe-GaAs(001) [14,15], Ge-GaAs(001) [16,17], and Si-GaP(001) [16], respectively. The large variation in the band offsets at the heterovalent interfaces originates from the existence of nonoctet bonds which form donor and acceptor states. Let us explain the mechanism for this referring to Fig. 1.2, in which the ZnSe-GaAs heterointerfaces are used as a model.

From the viewpoint of stability, no charges should be accumulated at interfaces, that is, interfaces should be completely "compensated" to achieve the charge neutrality [24,25]. This is because the charge accumulation brings the electric field that enlarges the energy in the system. In order to compensate the chemical valence mismatch and to achieve the charge neutrality in the heterovalent heterostructures, the same number of donor and acceptor bonds must exist at the interface. Figure 1.2 shows some of the most simplified examples satisfying this situation; (a) a mixed Ga-Zn plane with 50-50 composition and (b) an As-Se plane with the same composition at the interface. Owing to the transfer of excess electrons from the Ga-Se donor states to the Zn-As acceptor states, the dipole moments pointing toward GaAs (a) and ZnSe (b) are induced. The dipoles in Fig. 1.2(a) raise the potential of GaAs and make the valence band offset large, while by the dipoles in the opposite direction [Fig. 1.2(b)], the valence band offset becomes small. The first-principle

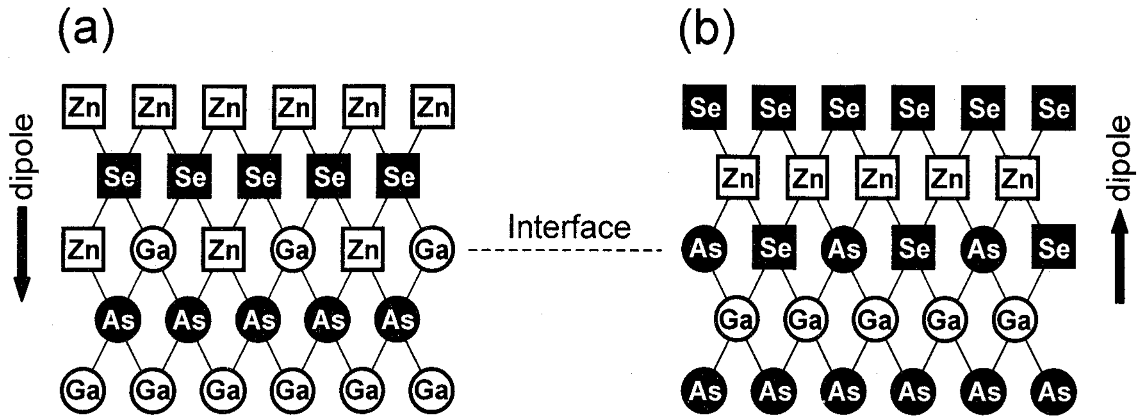

Figure 1.2: Formation of the electronic dipoles at the ZnSe-GaAs interfaces. The compensated neutral interfaces are formed with (a) a mixed Ga-Zn plane with 50-50 composition and (b) an As-Se plane with the same composition.

calculation by Nicolini *et al.* indicated that the valence band offsets in Figs. 1.2(a) and (b) are 1.59 and 0.62 eV, respectively [14], and also, similar calculation by Kley *et al.* indicated that those are 1.75 and 0.72 eV, respectively [15]. As is easily deduced, the strength and direction of the dipoles depend sensitively on the microscopic interface atomic configuration and, thus, so do the band offsets.

Experimentally, it has been revealed for several prototypical lattice-matched and theoretically well-understood heterostructures that the band offsets depend on the crystallographic orientation, the growth sequence, and the growth conditions [14, 18-23]. However, tunability via intentional control of the interface atomic configuration has never been achieved yet for any heterostructures. Since the band offset is a crucial parameter which determines the electronic behavior of the heterointerface, and thus device performance [26], the flexibility in designing new devices would be tremendously increased by the tunable band offsets.

From the above background, efforts are devoted in this study to control the band offsets through the interface engineering in the heterovalent heterostructures. Among a number of heterovalent material combinations, the heterostructure consisting of ZnSe and GaAs was selected. In order to emphasize the heterovalency, lattice mismatch should be avoided and, in this sense, ZnSe-GaAs [1] is an appropriate material combination because of small lattice mismatch of 0.27% at room temperature, which may provide structurally

ideal interfaces.

Toward the goal, there are two central problems to be solved; (1) how to fabricate the structure and (2) how to control the interface properties. Considering that many of the present-day heterostructure devices consist of multilayered structures, ZnSe and GaAs should also be grown alternately. However, the growth of GaAs on ZnSe is considerably more difficult than the much-studied inverse growth of ZnSe on GaAs, and therefore, fabrication of the ZnSe-GaAs multilayered structures has hardly been reported [27,28]. There are several reasons for this. Unfortunately, if a material A is grown two-dimensionally on a material B, the growth of the inverse heterostructure, B/A, is generally three-dimensional. This is explained well in terms of the force balance equation for the liquid-drop model of a nucleus, $\sigma_{\mathrm{u}} = \sigma_{\mathrm{eu}} + \sigma_{\mathrm{e}} \cos \eta$, where σ_{u} is the energy per unit area of the underlying layer-vapor interface, σ_{e} is the energy per unit area of the epilayer-vapor interface, σ_{eu} is the energy per unit area of the underlying layer-epilayer interface, and η is the contact angle between epilayer and underlying layer. The two-dimensional (2D) growth ($\eta = 0°$) of A/B satisfies $\sigma_{\mathrm{B}} = \sigma_{\mathrm{AB}} + \sigma_{\mathrm{A}}$, and with this equation, the contact angle η for the B/A growth satisfies $\cos \eta = (\sigma_{\mathrm{A}} - \sigma_{\mathrm{AB}})/\sigma_{\mathrm{B}} = 1 - 2\,\sigma_{\mathrm{AB}}/\sigma_{\mathrm{B}}$. This quantity cannot be unity, that is, the growth of B/A cannot be in the 2D growth mode. The liquid-drop model, however, assumes the equilibrium state and the actual growth, which is in a non-equilibrium state, might exhibit more complicated behavior. In turn, that may be a key to overcome the difficulty of the growth. Another issue specific for ZnSe-GaAs is the widely differing optimum growth temperatures; high-quality ZnSe is grown on GaAs at temperatures below 500°C, whereas GaAs with superior properties is grown at temperatures above 600°C in the case of metalorganic vapor phase epitaxy (MOVPE).

Let us introduce several reports on the growth of GaAs on ZnSe. Kobayashi and Horikoshi investigated GaAs molecular beam epitaxy (MBE) on ZnSe [27]. The growth was highly three-dimensional owing to the low sticking coefficient of GaAs on ZnSe, and to overcome this problem, the combination of solid-phase epitaxy (SPE) and migration-enhanced epitaxy (MEE) was employed. The uniform layer of GaAs was obtained by initiating the growth with As_4 adsorption on ZnSe and deposition of 2 atomic layers of Ga at room temperature followed by SPE and MEE. Farrell *et al.* examined the correlation between interface structures and the growth behavior of GaAs MBE onto ZnSe [29]. They pointed out that a ZnSe(100)$c(2 \times 2)$-Zn surface, which is terminated with 1/2 atomic

layer of Zn, is optimized by a sequence of steps involving a predeposition of excess Se and a low-temperature deposition of 1/2 atomic layer of Ga prior to the GaAs epitaxy. It is interesting to note that this procedure would provide equal numbers of Ga-Se and Zn-As bonds at the interface, resulting in charge neutrality.

In this work, on the other hand, we selected MOVPE as a growth method, expecting that the higher chemical reactivity in MOVPE may improve the low sticking probability of GaAs on ZnSe and enables us to avoid the complicated procedures involved in MBE. With respect to the artificial control of the band offsets, intuition appeals that MBE is more favorable for the atomic level control of the interface atomic configuration; *in situ* and/or *in line* monitoring of the interface formation is possible in MBE, for example, by reflection high energy electron diffraction (RHEED) and coaxial impact collision ion scattering spectroscopy (CAICISS). However, the procedures providing the high quality heterointerface are quite limited in MBE as mentioned above, which may affect the controllability of the band offset with keeping the quality of the heterostructures. In the case of MOVPE, we will demonstrate that the artificial control of the band offsets is successfully achieved with the help of its high reactivity.

Following this chapter, chapter 2 describes the MOVPE system, GaAs homoepitaxy, and ZnSe heteroepitaxy on GaAs. In particular, the nucleation processes of ZnSe on GaAs are investigated in detail and the condition that realizes atomically flat surfaces of ZnSe is revealed. The flat surface in the atomic level is ideal for manipulating the interface atomic configuration and, in chapter 3, this surface is used for the control of the band offsets. In chapters 4 and 5, the nucleation mechanisms and the control of the band offsets in GaAs/ZnSe are discussed, respectively. In chapter 6, the tunability of the band offsets in ZnSe/GaAs and GaAs/ZnSe attained in chapters 3 and 5 is applied to ZnSe-GaAs multilayered quantum structures. Unique characteristics which cannot be realized in the conventional isovalent material systems are demonstrated. The results of this study are summarized in chapter 7.

References

[1] In this study, a heterostructure consisting of (material A) and (material B), which includes a multilayered structure, is denoted as A-B and, in particular, a (material

A)-on-(material B) single-heterostructure as A/B.

[2] D. Leonard, M. Krishnamurthy, C. M. Reaves, S. P. DenBaars, and P. M. Petroff, Appl. Phys. Lett. **63**, 3203 (1993).

[3] J. Oshinowo, M. Nishioka, S. Ishida, and Y. Arakawa, Appl. Phys. Lett. **65**, 1421 (1994).

[4] Y. Nabetani, T. Ishikawa, S. Noda, and A. Sasaki, J. Appl. Phys. **76**, 347 (1994).

[5] M. Kumangai and T. Takagahara, Phys. Rev. B **40**, 12359 (1989).

[6] J. Khurgin, Phys. Rev. B **38**, 4056 (1988).

[7] E. T. Yu and T. Ç. McGill, Appl. Phys. Lett. **53**, 60 (1988).

[8] I. Morrison, M. Jaros, and A. W. Beavis, Appl. Phys. Lett. **55**, 1609 (1989).

[9] J. Ihm and M. L. Cohen, Phys. Rev. B **20**, 729 (1979).

[10] D. Shen, K. Zhang, and R. F. Fu, Appl. Phys. Lett. **53**, 500 (1988).

[11] R. Eppenga, Phys. Rev. B **40**, 10402 (1989).

[12] K. Oda and T. Nakayama, Jpn. J. Appl. Phys. **31**, 2359 (1992).

[13] L. A. Hemstreet, C. Y. Fong, and J. S. Nelson, J. Vac. Sci. Technol. B **11**, 1693 (1993).

[14] R. Nicolini, L. Vanzetti, G. Mula, G. Bratina, L. Sorba, A. Franciosi, M. Peressi, S. Baroni, R. Resta, A. Baldereschi, J. E. Angelo, and W. W. Gerrich, Phys. Rev. Lett. **72**, 294 (1994).

[15] A. Kley and J. Neugebauer, Phys. Rev. B **50**, 8616 (1994).

[16] R. G. Dandrea, S. Froyen, and A. Zunger, Phys. Rev. B **42**, 3213 (1990).

[17] K. Kunc and R. M. Martin, Phys. Rev. B **24**, 3445 (1981).

[18] G. Bratina, L. Vanzetti, A. Bonanni, L. Sorba, J. J. Paggel, A. Franciosi, T. Peluso, and L. Tapfer, J. Crystal Growth **159**, 703 (1996).

[19] R. W. Grant, J. R. Waldrop, and E. A. Kraut, J. Vac. Sci. Technol. **15**, 1451 (1978).

[20] R. W. Grant, J. R. Waldrop, S. P. Kowalczyk, and E. A. Kraut, J. Vac. Sci. Technol. B **3**, 1295 (1985).

[21] S. P. Kowalczyk, E. A. Kraut, J. R. Waldrop, and R. W. Grant, J. Vac. Sci. Technol. **21**, 482 (1982).

[22] P. Zurcher and R. S. Bauer, J. Vac. Sci. Technol. A **1**, 695 (1983).

[23] M. Dahmen, U. Rau, M. Kawanaka, J. Sone, and J. H. Werner, Appl. Phys. Lett. **62**, 261 (1993).

[24] W. A. Harrison, E. A. Kraut, J. R. Waldrop, and R. W. Grant, Phys. Rev. B **18**, 4402 (1978).

[25] R. M. Martin, J. Vac. Sci. Technol. **17**, 978 (1980).

[26] *Heterojunction Band Discontinuities, physics and device applications*, edited by F. Capassso and G. Margaritondo (North-Holland, Amsterdam, 1987).

[27] N. Kobayashi and Y. Horikoshi, Jpn. J. Appl. Phys. **29**, L236 (1990).

[28] S. Zhang and N. Kobayashi, Appl. Phys. Lett. **60**, 883 (1992).

[29] H. H. Farrell, M. C. Tamargo, J. L. de Miguel, F. S. Turco, D. M. Hwang, and R. E. Nahory, J. Appl. Phys. **69**, 7021 (1991).

Chapter 2

MOVPE Growth of ZnSe on GaAs

2.1 Introduction

Unlike isovalent heterostructures, an ideal planar geometry is not allowed at polar heterovalent interfaces, because that causes charge imbalance. Therefore, various interface atomic configurations such as intermixing, interfacial compounds like Ga_2Se_3 [1, 2], and interface reconstruction structures [3] may appear to attain the charge neutrality. These interface structures remarkably influence the subsequent nucleation processes and the properties of heterostructures [4-6]. Reflection high energy electron diffraction (RHEED) observation has shown [4] that the nucleation processes of ZnSe on GaAs(001) during molecular beam epitaxy (MBE) can be varied from a two-dimensional (2D) layer-by-layer mode to a three-dimensional (3D) island formation by modifying the stoichiometry of the starting GaAs surface. Furthermore, it has been reported that the dislocation configuration and the crystalline quality of ZnSe epilayers depend on the initial nucleation processes [5, 6]; the 3D initial nucleation brings a high density of threading dislocations, while the increasingly 2D nucleation results in fewer threading dislocations.

However, it should be noted that the correlation between the interface structures and the following growth remains uncertain. This is because interface structures can be modified by changing the growth conditions and the growth techniques, which leads to various nucleation processes. In particular, there is no report on the detailed nucleation behavior of ZnSe during metalorganic vapor phase epitaxy (MOVPE), although the presence of hydrogen and hydrocarbons during the growth can make a considerable difference between MOVPE and MBE. Toward a comprehensive understanding of the nucleation processes, we investigate, chiefly by means of atomic force microscope (AFM) [7], the surface morphology

of ZnSe grown on GaAs(001) by MOVPE. In order to facilitate the observation of the nucleation, the GaAs surfaces before the ZnSe growth are carefully manipulated to consist of atomically flat terraces and monolayer (ML) steps. Then, the nucleation processes of ZnSe on GaAs are discussed. The growth conditions under which an atomically flat surface is obtained are revealed for the first time in this material system.

2.2 MOVPE Growth

The epitaxial growth was carried out using an atmospheric-pressure MOVPE system which was specially designed and constructed for this study. The MOVPE system is schematically illustrated in Fig. 2.1. Triethylgallium (TEGa) and tertiarybutylarsine (TBAs) were used as source precursors for the GaAs growth, and diethylzinc (DEZn) and dimethylselenium (DMSe) for the ZnSe growth. The flow rates were precisely controlled by mass flow controllers. The cation sources (TEGa and DEZn) and the anion sources (TBAs and DMSe) were separately transferred from the bubblers to the reactor by hydrogen passed through a Pd hydrogen purifier, and mixed at the very entrance of the reactor. The total hydrogen flow rate was about 3 SLM, which corresponded to the flow velocity of 15 cm/s just above a substrate. The reactor was made of transparent quartz and was in the vertical configuration. In order to absorb unfavorable reaction products during growth, the reactor was cooled with water.

Substrates were set on a SiC-coated graphite susceptor and heated by radio frequency (RF) induction with a 29-kHz, 5-kW RF generator. The susceptor temperature was monitored using a Pt-PtRh(13%) thermocouple. The difference between the measured and the real temperature was adjusted in advance using the melting points of Pb (327.5°C), Zn (420.0°C), and Al (660.5°C).

The typical flow rates for TEGa and TBAs were 10 and 100 μmol/min, respectively, while those for DEZn and DMSe were 1.2 and 12 μmol/min, respectively. These flow rates realized the anion-excess growth ambient which is desirable for obtaining high crystalline quality. The growth rate of GaAs under these flow rates was 1.0 μm/h for growth temperatures between 450 and 700°C and was decreased to 0.8 μm/h at 400°C. Regarding ZnSe, the growth rate depended on the growth temperature. At a typical growth temperature of 450°C, the growth rate under the above flow rates was 0.2 ML/s (= 0.57 Å/s). Both ZnSe

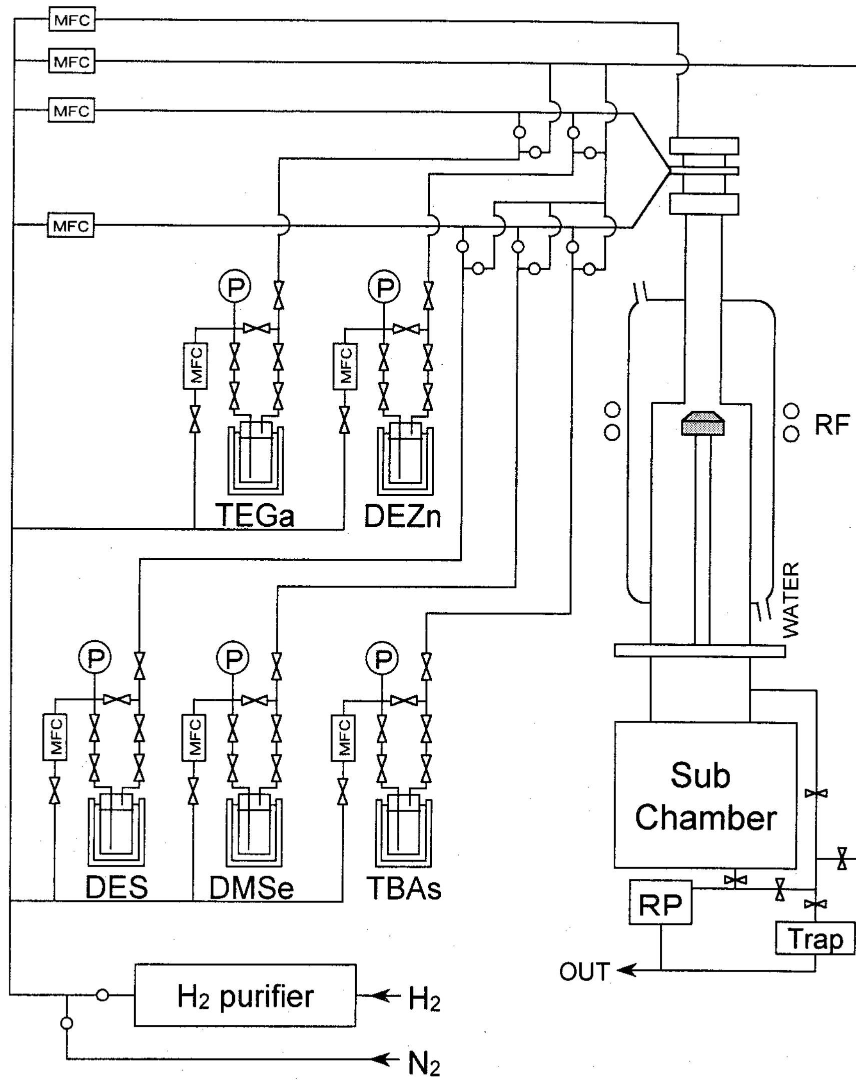

Figure 2.1: Schematic diagram of the MOVPE system.

and GaAs layers were grown in the same reactor.

2.3 Preparation of GaAs Surfaces

The substrates used in this study were GaAs(001) nominally singular substrates. The unintentional misorientation angle of the substrates from the (001) singular surface was less than 0.05°. Prior to the growth, the substrates were cleaned by degreasing in acetone and methanol followed by chemical etching in an acidic solution of $H_2SO_4 : H_2O_2 : H_2O = 5 : 1 : 1$ (by volume) at 40°C for 1 min. After being etched chemically, the GaAs substrates were subjected to thermal annealing in the MOVPE reactor to desorb the surface oxide layer. The effect of annealing conditions on surface structures of GaAs was examined.

Figure 2.2 compares AFM images of the GaAs substrates annealed at 590°C for 10 min in (a) nitrogen, (b) hydrogen, and (c) a mixture of TBAs/hydrogen. It is clearly seen that annealing in the nitrogen ambient resulted in a rough surface covered with a significant number of nuclei. Moreover, the detailed observation revealed the existence, in places, of holes 2 nm in depth, which developed deeper as the annealing temperature was raised to 630°C.

On the other hand, all steps observed in Fig. 2.2(b) are 1-ML high and no nuclei

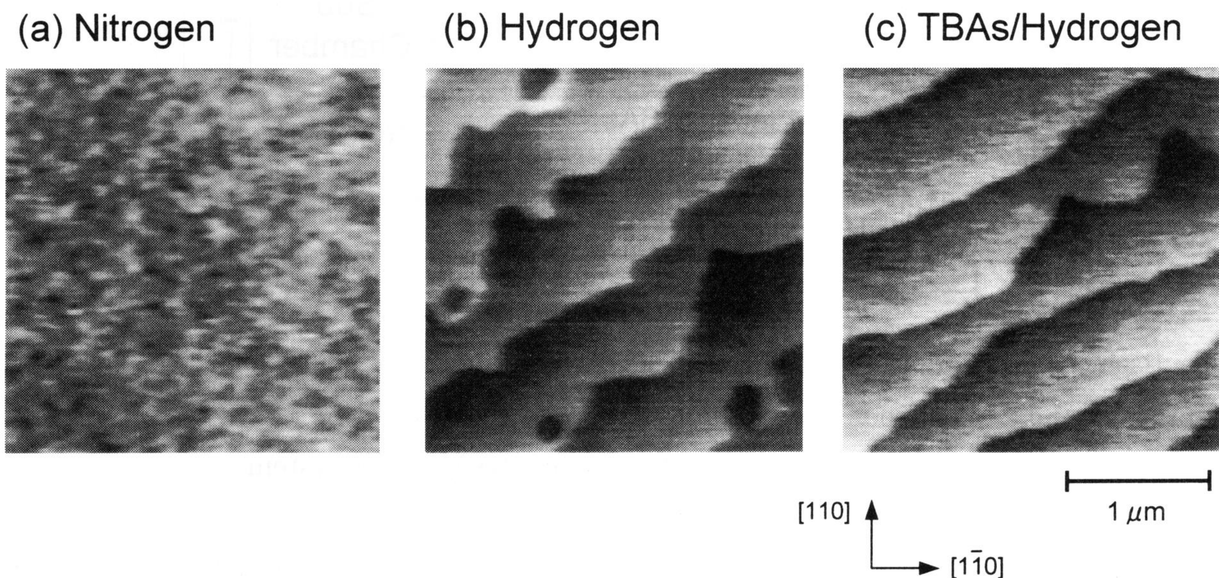

Figure 2.2: AFM images of the GaAs substrates annealed at 590°C for 10 min in (a) nitrogen, (b) hydrogen, and (c) a mixture of TBAs/hydrogen.

are detected on the terraces, indicating that the hydrogen ambient makes the surface atomically flat. A terrace width about 500 nm is equivalent to a 0.03° misorientation from the [001] direction. Therefore, the density and direction of the steps reflect the unintentional misorientation of the substrate. The surface-terminating atoms must be Ga owing to the absence of As flow. A similar surface could be obtained by annealing in the temperature region between 590 and 630°C. However, annealing at a higher temperature of 700°C formed hillocks, presumably Ga-droplets, although terraces and ML steps were still preserved.

Let us consider the mechanism for the formation of the flat surface by annealing in the hydrogen ambient at 590 – 630°C [Fig. 2.2(b)]. If Ga atoms detach from step edges for migration, As evaporation follows immediately owing to the higher vapor pressure of As and the lack of As in the ambient. Under this situation, migrating Ga atoms no longer have places to be incorporated into GaAs again, resulting in the formation of 3D Ga-droplets. Therefore, it is reasonable to consider that there are few Ga atoms which desorb from the step edges and are migrating on the GaAs surface. In order to clarify whether desorption of Ga atoms from the step edges is suppressed by hydrogen or promoted by nitrogen, annealing was performed using a MBE chamber. Consequently, we have found it difficult to obtain an atomically flat surface of GaAs under ultra high vacuum without an As flux. This indicates that hydrogen plays an important role in suppressing desorption of Ga and in forming an atomically flat surface. Recently, Koukitu *et al.* reported that, in halogen transport atomic layer epitaxy, Ga atoms on a GaAs surface were terminated by hydrogen from the carrier gas [8]. Analogically, the surface Ga atoms during annealing in the hydrogen ambient seem to be terminated by hydrogen. Since bonding with a hydrogen well reduces the number of dangling bonds and lowers the surface energy, the surface terminated by hydrogen is relatively stable and desorption of Ga, which increases the surface energy, is suppressed.

Introduction of TBAs into the hydrogen ambient also resulted in the formation of atomically flat terraces and ML steps, as shown in Fig. 2.2(c). Annealing between 590 and 700°C provided similar surface structures. No hillocks were formed even at 700°C under the TBAs flow and this finding supports the previous hypothesis that the hillocks generated by annealing at 700°C without As are Ga-droplets. Comparing Figs. 2.2(b) and (c), it is found that the role of TBAs is to make steps smooth. With the TBAs flow, desorption of Ga atoms from step edges can occur without increasing the surface energy remarkably,

because As in the ambient allows the desorbed Ga atoms to readsorb to GaAs and realizes the equilibrium state between the desorption and the readsorption. The desorbed Ga atoms migrate relatively freely on the GaAs surface and, as a result, the ML steps are straightened so as to minimize the total surface energy.

For II-VI heteroepitaxy on GaAs, an As source is not necessarily equipped to a growth chamber, because it may be the origin of contamination. Although an As source is needed to control surface atoms of GaAs, it is worth noting from a structural viewpoint that atomically flat surfaces can be obtained by annealing in a hydrogen ambient without an As source.

A 1500-Å-thick GaAs buffer layer was grown at 700°C on the substrate annealed in a mixture of TBAs/hydrogen. AFM observations revealed that the surface of the epilayer consisted of terraces, ML steps, and 2D islands, indicating that the growth was in the 2D nucleation mode. Since the step edge acts as the major sink for the surface migrating species, the 2D islands remained only in the middle of the terraces. In order to remove the 2D islands, post-growth annealing [9] was performed at 700°C for 10 min with the TBAs flow. The surface after annealing possessed regular terraces without 2D islands as illustrated in Fig. 2.3. The step edges, which were not modified by post-growth annealing, became much straighter than those on the surface of the GaAs substrate [Fig. 2.2(c)]. The straightened step edges indicate the decrease in the number of kink sites. Therefore, the GaAs epilayer has lower surface energy and is more stable than the GaAs substrate. The steps 1-ML high indicate that the surface is fully stabilized by either Ga or As. Arsenic is a more plausible candidate because the substrate was cooled with the TBAs flow after annealing [10, 11].

The As-terminated GaAs epilayer obtained by the above mentioned procedure was used for the following ZnSe growth. Since a ZnSe layer was successively grown in the same reactor, the GaAs buffer layers were kept in the reactor under hydrogen flow at 200°C for typically 1 h for purging of the source precursors for the GaAs growth.

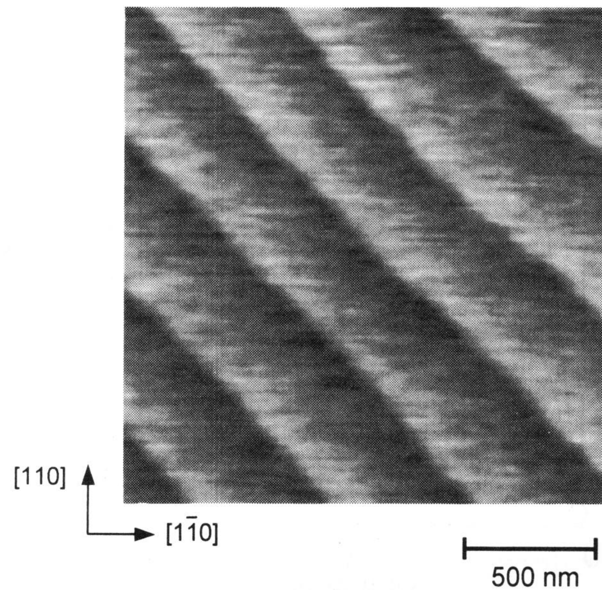

Figure 2.3: AFM image of the GaAs epilayer grown at 700°C followed by annealing at the same temperature for 10 min. The epilayer thickness is 1500 Å. The height of all steps is 1 ML.

2.4 Nucleation Processes of ZnSe on GaAs

2.4.1 Rate-limiting steps

Before describing detailed nucleation processes, the rate-limiting steps during MOVPE growth of ZnSe are summarized.

At several temperatures, the growth rate as a function of the molar flow ratio of DMSe/DEZn (VI/II ratio) was investigated, where the flow rate of DEZn ([DEZn]) was kept constant at 6 μmol/min. The results are indicated in Fig. 2.4. Regardless of the growth temperatures, the growth rate increased with increasing the VI/II ratio when it was lower than approximately three, while it was independent of higher VI/II ratios. In other words, when the VI/II ratio is lower than three, the growth rate is limited by the DMSe flow rate, whereas the VI/II ratio higher than three realizes the DMSe-excess condition. Since the crystal growth should be performed in an anion-excess ambient for attaining high crystalline quality, the VI/II ratio was typically set at 10 in this study.

Figure 2.5 shows dependence of the growth rate on the reciprocal growth temperature under a constant VI/II ratio of 10. The growth rate did not depend on growth temperatures

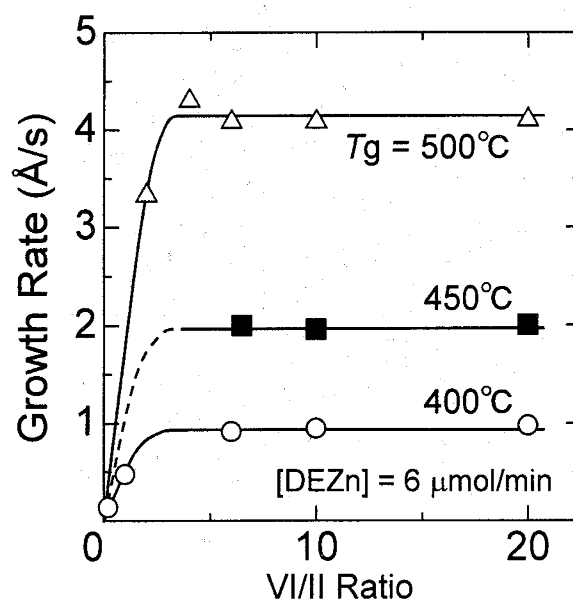

Figure 2.4: Growth rate versus molar flow ratio of DMSe/DEZn (VI/II ratio).

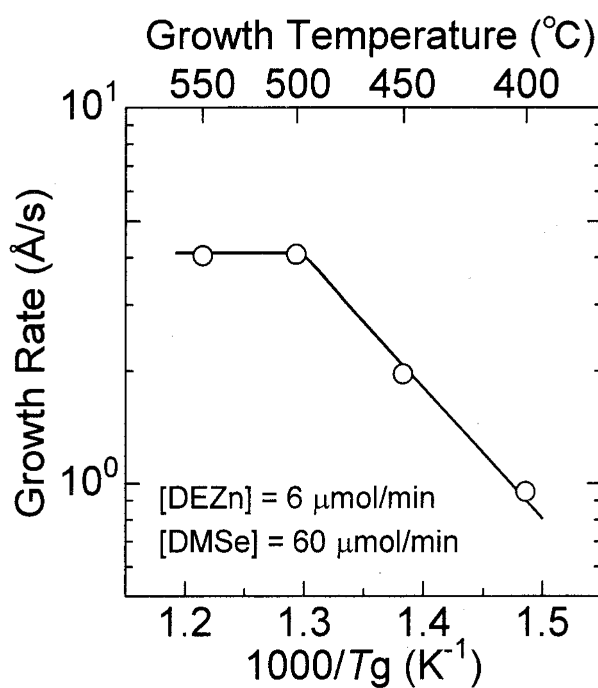

Figure 2.5: Growth rate versus reciprocal growth temperature (T_g).

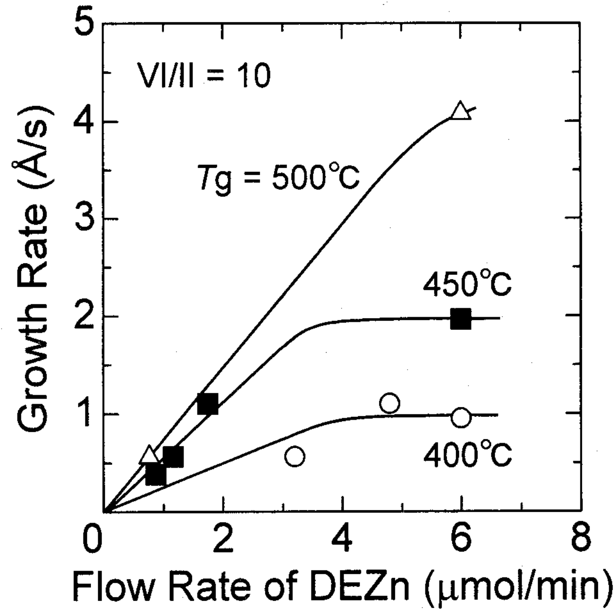

Figure 2.6: Dependence of the growth rate on [DEZn]. The VI/II ratio is constant at 10.

above 500°C, which is indicative of mass-transport-limited growth. On the other hand, at temperatures below 500°C, the growth rate decreased with decreasing temperature, characteristics of a process limited by surface kinetics. As is deduced from the figure, the growth rate in this regime can be expressed as $R_{\mathrm{g}}^{\infty}\exp(-\Delta E/k_{\mathrm{B}}T)$, where R_{g}^{∞} is a constant, ΔE is the activation energy, k_{B} is the Bolzmann constant, and T is the absolute temperature. From this equation, the activation energy was estimated to be 20 kcal/mol, which is typical for ZnSe MOVPE [12].

Figure 2.6 shows variation of the growth rate due to [DEZn]. Here, the VI/II ratio was, again, 10. At the growth temperatures of 400 and 450°C, the growth rates appeared to saturate with increasing [DEZn] when it exceeded 4.0 and 3.5 μmol/min, respectively. Since the growth below 500°C is limited by surface kinetics as shown in Fig. 2.5, these saturating growth rates indicate that those are determined by the reaction rate for generating ZnSe and, consequently, that both DEZn and DMSe are excess in the ambient. On the other hand, under other conditions, that is, [DEZn] less than 4.0 μmol/min at 400°C, less than 3.5 μmol/min at 450°C, or the growth temperature of 500°C, the growth rate was almost proportional to [DEZn]. This indicates that the surface kinetic step limiting the growth rate is related to DEZn.

2.4.2 Effects of growth parameters

In this section, first, the effects of the growth temperature and the VI/II ratio on the nucleation processes are investigated. Then, the effects of the growth rate are discussed. The thickness of ZnSe was 100 Å for all samples in this section, at which the growth is not influenced by the interface, as verified in Sec. 2.4.3.

growth temperature and molar flow ratio

The growth rate of ZnSe depends on the growth temperature as shown in Fig. 2.5. Therefore, the molar flow rates were adjusted so as to maintain a growth rate of 0.2 ML/s (= 0.57 Å/s), by which the influence of the growth rate could be avoided. Note that the rate-limiting step for the growth rate of 0.2 ML/s is related to [DEZn] (see Fig. 2.6). This is a favorable condition in terms of surface flatness as shown later.

The ZnSe surfaces were observed by AFM in air immediately after the growth. Figure 2.7 compares AFM surface images and cross sections of ZnSe grown at 400, 450, and 500°C with a VI/II ratio of 10. A significant degree of 2D nucleation is observed on the surface of ZnSe grown at 400°C [Fig. 2.7(a)]. Surface roughness estimated from the cross section is ±1 ML, indicating that the growth was in the multinucleation mode where 2D nucleation occurs before the underlying 2D nuclei complete 1 ML growth. At 450°C as well, ZnSe grew though 2D nucleation [Fig. 2.7(b)]. In those figures, representative features are indicated by arrowheads. Those indicated by the arrowheads marked ① are 1 ML steps. Small islands typically 20 nm in diameter and relatively large islands which are assemblies of small islands are represented by the arrowheads marked ② and ③, respectively. As mentioned previously, the misorientation of the substrate is within 0.05°, which corresponds to a terrace width of greater than 320 nm. The observed separations of ML steps marked ① are about 200 – 500 nm, and therefore the ML steps are derived from the substrate misorientation. It should be noted that all steps and islands observed on the surfaces of ZnSe grown at 400 and 450°C are 1-ML high, indicating that the ZnSe surface is fully covered with either Zn or Se. Se is more plausible because the MOVPE growth was carried out with an excess of DMSe. The difference between 400 and 450°C growth is that, at 450°C, the background of the islands is atomically flat, which means that the growth is in the layer-by-layer mode. The transition from the multinucleation mode to the layer-by-layer

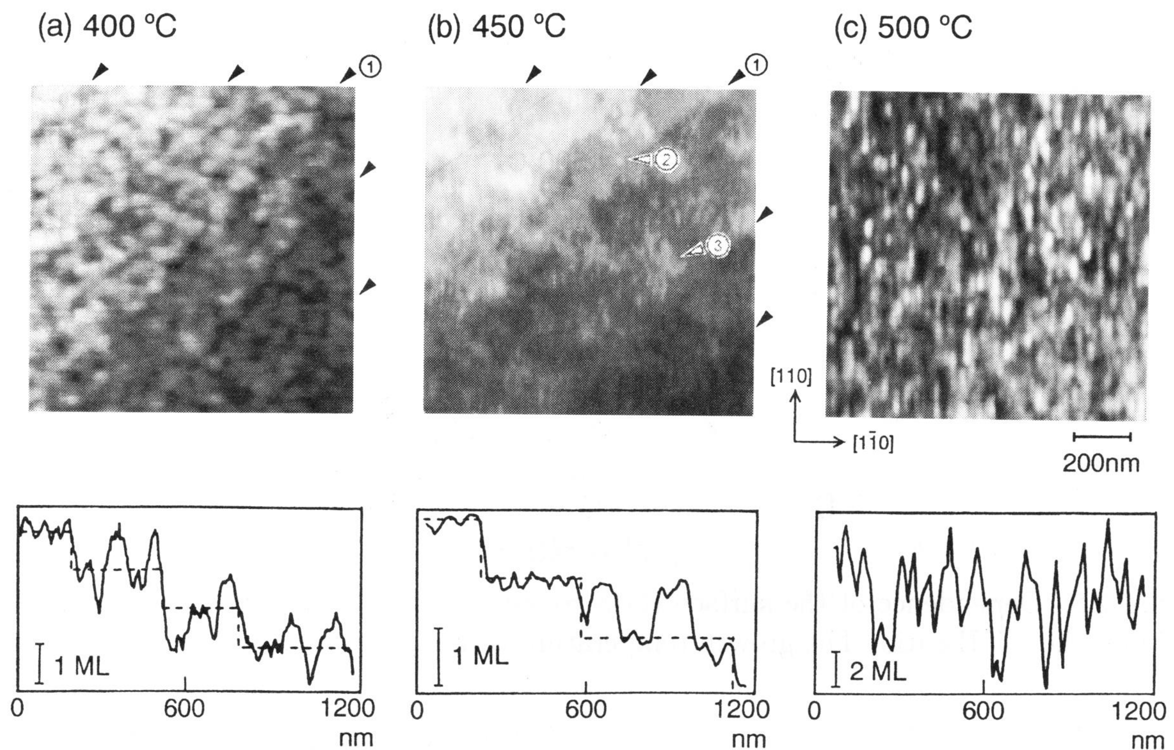

Figure 2.7: AFM images and cross sections of as-grown ZnSe surfaces. The growth temperatures are (a) 400, (b) 450, and (c) 500°C, respectively. Arrowheads marked 1 indicate 1 ML steps. Arrowheads marked 2 and 3 represent small islands typically 20 nm in diameter and relatively large islands which are assemblies of small islands, respectively. The dotted lines in the cross sections indicate the background step structures.

mode is due to the higher growth temperature. Increasing the growth temperature would result in an increase in the diffusion coefficient of adatoms and consequently promotion of 2D layer-by-layer growth. One may feel that a further increase in the growth temperature brings step flow growth mode, although, contrary to expectation, ZnSe grown at 500°C was highly three-dimensional as shown in Fig. 2.7(c). The surface root-mean-square (RMS) roughness was 10.4 Å and islands were elongated in the [110] direction.

To discuss the results obtained by the AFM observations more quantitatively, the surface RMS roughness was summarized in Fig. 2.8 as a function of the VI/II ratio, where the growth temperature is a parameter. The VI/II ratio was varied with changing the flow rate of DMSe, while keeping [DEZn] constant. At 400°C, the multinucleation growth was preserved at any VI/II ratios and the surface RMS roughness was estimated to be

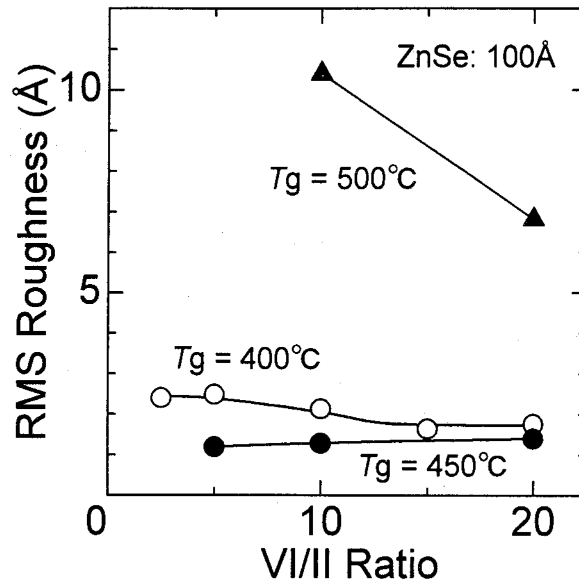

Figure 2.8: Dependence of the surface RMS roughness of ZnSe/GaAs(001) measured by AFM on the VI/II ratio. The growth temperature is used as a parameter.

within 1 ML (= 2.8 Å). However, surface morphology was slightly modified by the VI/II ratio. ZnSe islands 1-ML high, which have round shape when the VI/II ratio is less than 10 [*cf.* Fig. 2.7(a)], were elongated toward [110] by VI/II ratios higher than 15. Since Se is bound at [110] steps more weakly than at [$\bar{1}$10] steps, the deficiency of Se at the [110] steps might occur, in particular, under low VI/II ratios. The increase of excess Se by high VI/II ratios reduces the deficiency of Se at the [110] steps and enhances the incorporation of Zn adatoms at the [110] steps, resulting in faster growth rates in the [110] direction and, thus, the anisotropic island shape. With respect to ZnSe grown at 450°C, changes in the surface RMS roughness and in surface morphology were not appreciated. On the other hand, surface roughness of ZnSe grown at 500°C was remarkably improved by the high VI/II ratio, implying that the formation mechanism of 3D anisotropic islands is related to the amount of Se on the surface. If the amount of Se is small under low VI/II ratios, migration of Zn adatoms is enhanced. Under this situation, the migrating Zn atoms easily coalesce with each other and cohere to form 3D islands because the possibility of Zn meeting Se is low. Concerning anisotropy of the 3D islands, it hardly depended on the VI/II ratio and seems to be caused by Zn atoms. Owing to the anisotropic bond configuration, a Zn atom at a [110] step is bound by three bonds to the step side and the step bottom [(001) plane], whereas one at a [1$\bar{1}$0] step is bound by two bonds to the step bottom. Thus, islands tend

to be elongated in the [110] direction in which a Zn atom is bound more strongly by the larger number of bonds.

growth rate

With the growth temperatures of 400 and 500°C, the variation of the growth rate did not alter the nucleation processes drastically. Thus, here, the results with the growth temperature of 450°C are described. The VI/II ratio was constant at 10.

The surfaces of ZnSe grown with different growth rates were observed by AFM. As long as the growth was limited by the amount of the supplying DEZn, which is realized by [DEZn] $<$ 3.5 μmol/min (*cf.* Fig. 2.6), the surfaces were atomically flat similar to Fig. 2.7(b). However, ZnSe grown in the reaction-kinetics-limited growth regime ([DEZn] $>$ 3.5 μmol/min) exhibited a rough surface as shown in Fig. 2.9. The surface is wavy with roughness of ± 5 Å. In the reaction-kinetics-limited growth regime, excess source precursors exist in the ambient, which is supposed to affect the surface flatness of ZnSe, for example, through deposition of Zn metal. These results strongly suggest that, in terms of the surface flatness, the growth should be performed in the growth regime where the rate-limiting step is the amount of the supplying source precursors.

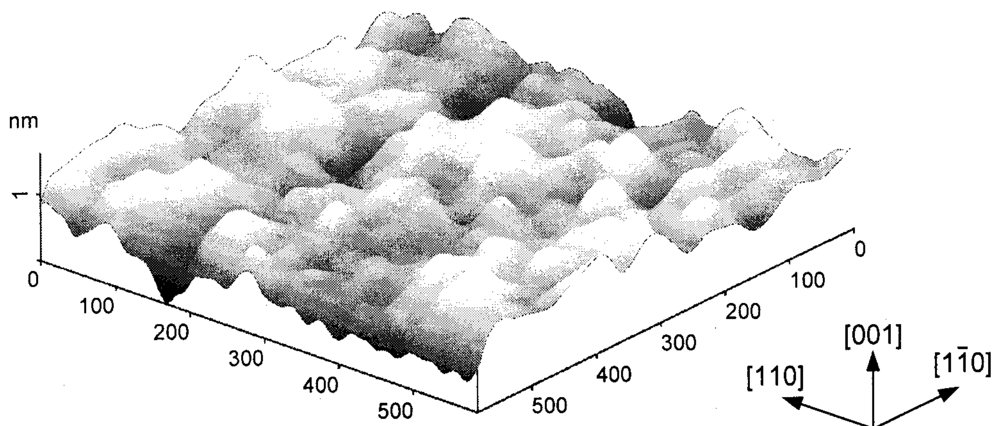

Figure 2.9: AFM image of ZnSe grown at 450°C with [DEZn] of 6 μmol/min and a VI/II ratio of 10, which bring the reaction-kinetics-limited growth.

The conclusion extracted from the above discussions concerning the growth parameters is that, for obtaining an atomically flat surface of ZnSe, strict control of the growth temperature and the growth rate is necessary, though that of the VI/II ratio is not.

comparison with MBE growth

Let us compare the present results with MBE growth, by which ZnSe-based devices have, so far, been fabricated [13, 14]. The typical growth temperature in MBE is as low as 300°C, and this seems to be too low to achieve sufficient migration, considering the optimal growth temperature revealed in this study, that is, 450°C. In addition to the growth temperature, the growth method itself also plays an important role in determining the diffusivity of adatoms; in the case of GaAs homoepitaxy, the diffusion coefficient of Ga adatoms on a GaAs surface in MBE is much smaller than that in MOVPE [15]. The present results as well as this report imply that it is quite difficult to form an atomically flat surface of ZnSe by MBE with conventional methods. Then, are there some possible ways to realize an atomically flat surface with terraces and ML steps by MBE? It depends on both diffusion coefficient of adatoms and substrate misorientation. Namely, if adatoms can diffuse more than half of terrace width, which is determined by the misorientation, step propagation growth will occur and the resultant surface will be atomically flat. Therefore, one possibility is to employ the growth method such as migration enhanced epitaxy (MEE) and atomic layer epitaxy (ALE) which may achieve greater diffusion coefficients. The recent investigation for GaAs homoepitaxy revealed that the diffusion coefficient in ALE-MOVPE is about two orders of magnitude larger than in conventional MOVPE [16]. The other possibility is to use substrates with higher misorientation. Since higher misorientation causes narrower terrace width, the growth on such substrates may be in the step flow mode even with a low diffusivity, resulting in an atomically flat surface.

2.4.3 Initial nucleation processes

The growth temperature of 450°C was revealed to be suitable for obtaining the atomically flat ZnSe surface. Therefore, discussions hereafter focus on the nucleation at 450°C. Since the nucleation processes may depend on the interface structure as described in Sec. 2.1, the interfaces were formed with different manners; before beginning the ZnSe growth, the GaAs surfaces were exposed to either the Zn or the Se precursor for 1 min

and 15 s, respectively at 450°C. Differences in the nucleation behavior due to the starting precursors were investigated.

The ZnSe surfaces were observed by AFM. Figure 2.10 traces how the initial nucleation behavior changed as the growth proceeded. Regardless of the starting precursors and the film thickness, ML steps which already existed on underlying GaAs (Fig. 2.3) persisted to the ZnSe surfaces as indicated by arrowheads. At a very early stage of the Zn-initiated growth, a number of islands were formed on terraces as observed in the AFM image of 10-Å-thick ZnSe. The distribution of the islands is homogeneous in the entire area of the sample surface and the density was estimated to be 3×10^{10} cm^{-2}. The height of the islands is 1 ML, indicating that the growth was in the 2D nucleation mode. The islands are elongated in the [110] direction; the typical dimensions are 100 nm in the [110] direction and 25 nm in the [1$\bar{1}$0] direction. This is probably caused by the anisotropic bond configuration. When a Zn atom migrating on the surface is incorporated into an island, the Zn atom is bound more strongly at a [110] step by the larger number of bonds, which elongates the islands in the corresponding direction. This is the same mechanism considered for the 3D islands in Sec. 2.4.2. As the growth continued, the anisotropic islands disappeared and relatively wide areas with atomically flat surfaces appeared at a layer thickness of 30 Å. The similar surface structure continued up to, at least, 900 Å. This transition from a number of 2D nuclei to the flat surface indicates a decrease of the nucleation density. It has generally been found that the nucleation density decreases as surface diffusion is activated, and therefore, Zn adatoms on ZnSe are supposed to diffuse more easily than on GaAs.

Regarding the Se-initiated growth, the feature of the initial nucleation is different from that of the Zn-initiated growth; although 2D islands are observed on 10-Å-thick ZnSe, they exhibit isotropic round shape with typically 10 nm in diameter and their density, 8×10^{10} cm^{-2}, is about three times higher than that in the Zn-initiated growth. Furthermore, surface roughness determined from a cross sectional view is ±1 ML, indicating that the growth was in the multinucleation mode. These differences of the nucleation behavior indicate that the diffusion of Zn adatoms is suppressed on GaAs exposed to DMSe. As the thickness of ZnSe was increased, the islands developed and the diameter became about 30 nm at a thickness of 30 Å. The further increase in thickness to about 100 Å brought the transition from 2D nuclei to an atomically flat surface. The thickness at which the transition occurs is thicker in the Se-initiated growth than in the Zn-initiated growth. This also

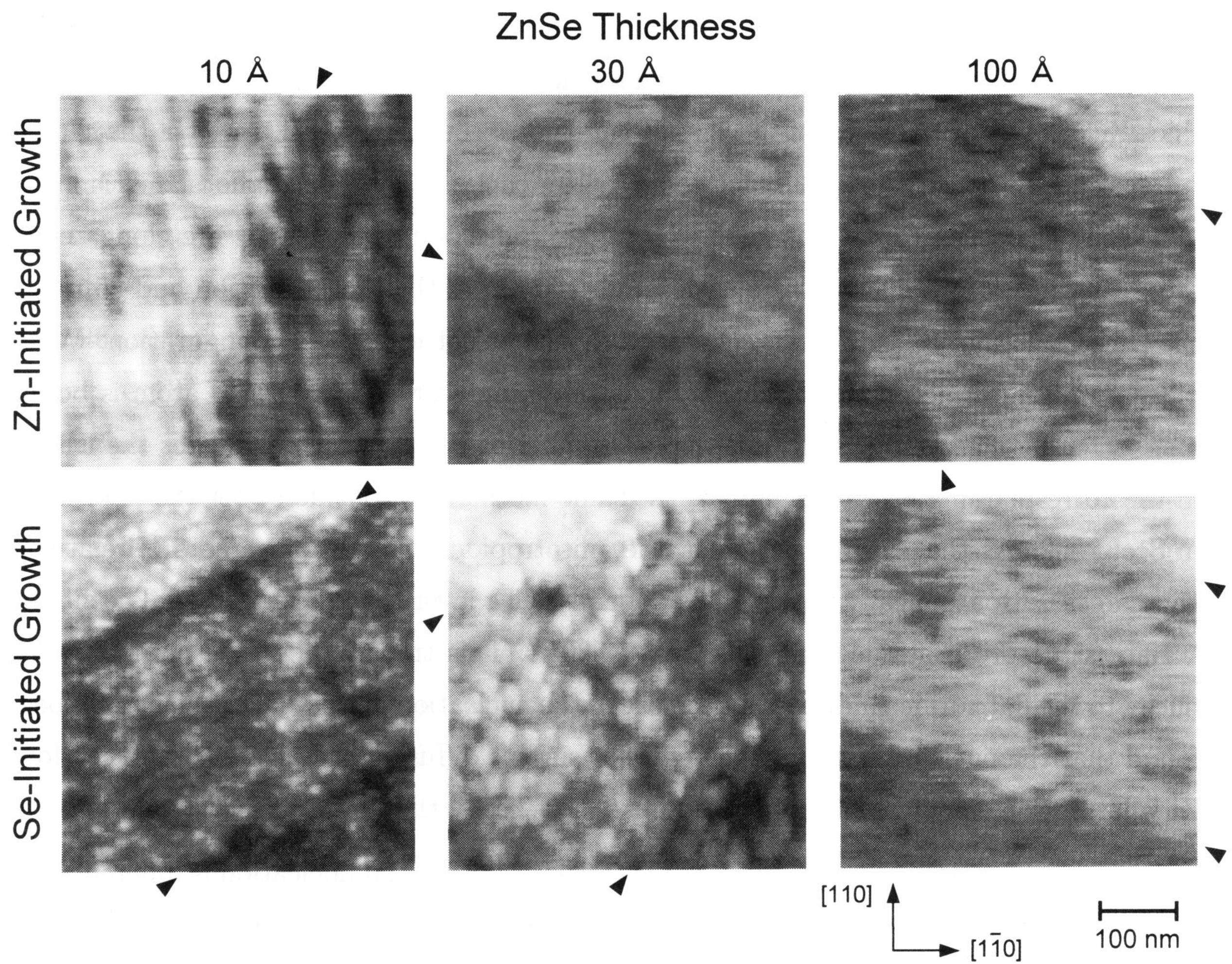

Figure 2.10: AFM images of the nucleation behavior of ZnSe grown at 450°C. The nucleation processes depend on the starting precursors and change as the growth proceeds. Arrowheads indicate 1 ML steps.

originates from the less diffusivity of Zn atoms on the Se-treated GaAs. ZnSe thicker than 100 Å showed similar surface structures with ZnSe thicker than 30 Å in the Zn-initiated growth. Thus, the growth with atomically flat terraces is free from the influence of the ZnSe/GaAs interface and may approximate the homoepitaxy of ZnSe, where the epitaxial material is growing onto itself.

Now, a question arises why the starting precursors cause the difference in the nucleation processes of ZnSe on GaAs. Since the growth conditions are completely the same for the Zn- and the Se-initiated growth, attention should be directed to the interface properties. Thus, the atomic configuration near the heterointerfaces was investigated by x-ray crystal truncation rod (CTR) scattering measurements [17]. As a result, it has been revealed that in the Zn-initiated growth, Ga and Zn atoms interdiffused into several ML's, while the As and Se distributions changed quite abruptly at the interface. For the Se-initiated heterointerfaces, on the other hand, the CTR profiles could not be interpreted only by assuming the distribution of the constituent atoms on the zincblende lattice, implying the introduction of imperfections such as vacancies, anti-site defects, and interstitial atoms to the interfaces. This difference of the interface structures due to the starting precursors gives rise to the variation of the nucleation processes revealed by AFM. In the case of the Se-initiated growth, since the imperfections and/or strain induced by them can modify the surface energy around them, the distribution of the surface energy becomes inhomogeneous. This inhomogeneity causes inhomogeneous nucleation, that is, the formation of a significant number of 2D islands as observed in the AFM images (Fig. 2.10).

The analysis of the CTR profiles is in progress, and the origin of the imperfections introduced by the Se-initiated growth has not been identified yet. For a complement, (110) cross-sectional views of the interfaces were observed by transmission electron microscopy (TEM) using a JEOL JEM2000EX system operated at 200 kV. The samples were prepared by the conventional Ar^+-milling at room temperature. Figure 2.11 shows TEM 002 dark field images of the (110) cross sections of (a) the Zn-initiated and (b) the Se-initiated interface. In Fig. 2.11(a), the interface is featureless, indicating the absence of a transition layer. This does not contradict the result of the x-ray CTR measurements. For the Se-initiated growth [Fig. 2.11(b)], on the other hand, dark contrast observed at the interface proves the presence of an interfacial layer which includes the imperfections revealed by the CTR measurements. The $00\bar{2}$ dark field image also exhibited a dark interface line. These

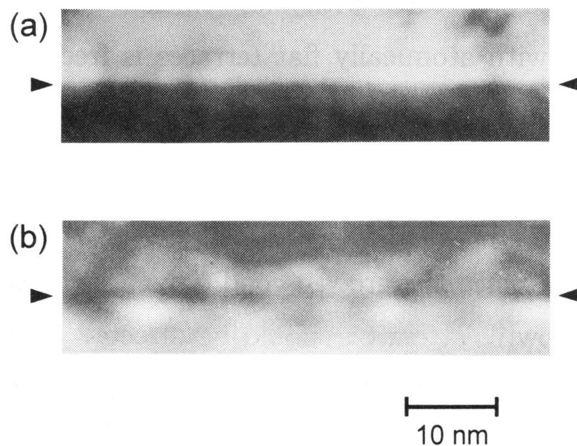

Figure 2.11: TEM 002 dark field images of the (110) cross sections of the ZnSe/GaAs heterostructures. Differences in the interface structure due to the starting precursor for the ZnSe growth are compared, (a) Zn-initiated growth and (b) Se-initiated growth. The interfaces are marked by arrowheads.

findings indicate that the value of a 002-type structure factor of the interfacial layer must be less than those of ZnSe and GaAs. Since the structure factor of 002 reflection is given by a difference of individual atomic scattering factors, and since the values of the scattering factors for Zn, Ga, As, and Se are nearly equal, the 002 structure factors for ZnSe and GaAs are very small (3.5 and 1.5, respectively). Therefore, the 002 structure factor of the interfacial layer might be almost zero, which is achieved by a stack of atomic layers with nearly the same scattering factors. This indicates that an interfacial layer which possesses vacancies only in the cation sublattice does not exist in the present MOVPE samples, because the 002 structure factor for such a transition layer is greater than those for ZnSe and GaAs and brings bright contrast in TEM images. When ZnSe is grown by MBE on Se-treated GaAs, Ga_2Se_3 containing Ga (cation) vacancies is formed at the interface as suggested by earlier studies [1,2]. However, based on the above analysis on the structure factor, we can rule out the possibility of the formation of Ga_2Se_3 in the present MOVPE samples.

Here, we will discuss differences between MBE and our MOVPE results. It has often been reported that a Zn-exposure treatment of GaAs surfaces prior to the MBE growth of ZnSe resulted in the 2D growth as verified by a streaky RHEED pattern [6]. The Zn-initiated growth in MOVPE was also in the 2D growth mode as shown in Fig. 2.10. At

present, we find no evidence to clarify a difference between MBE and MOVPE with respect to the Zn-initiated growth. A Se-exposure, on the other hand, brings the Ga_2Se_3 interfacial layer [1,2] and the corresponding 3D growth in the case of MBE [5,6]. The mechanism for the formation of Ga_2Se_3 and the 3D growth has been explained as follows [18]: The Se-terminated GaAs contains Ga vacancies in order to satisfy the charge neutrality, and the Se dimers at the GaAs surface possess positive charge as a result of electron transfer from the Se dimers to the Ga vacancies. This positive charge results in the filled dangling bonds at the Se dimers being pulled in slightly closer to the surface, which makes the surface more stable and hence, less reactive. A sticking probability of ZnSe to the less reactive GaAs surface is much lower than that of ZnSe to ZnSe. Therefore, ZnSe preferably grows on itself, resulting in the 3D growth. Concerning the structure of the 3D ZnSe/GaAs interface grown by MBE, TEM observations revealed the existence of a zincblende type compound of Ga_2Se_3 having Ga vacancies [1,2]. The Ga vacancies induced by the Se-exposure are preserved even after the growth of ZnSe to be observed as Ga_2Se_3. In contrast, 3D growth did not occur in the present MOVPE growth as shown in Fig. 2.10, and the TEM image (Fig. 2.11) indicated the absence of Ga_2Se_3 at the interface. The remarkable difference of MOVPE from MBE is the presence of hydrogen and hydrocarbons. Therefore, we consider that hydrogen and/or hydrocarbons being provided during the exposure of GaAs to DMSe change the condition for the charge neutrality and obstruct the generation of Ga vacancies and, thus, Ga_2Se_3. Consequently, the GaAs surface exposed to DMSe becomes reactive compared with that exposed to Se in a MBE chamber, and the 2D growth of ZnSe is promoted.

The variation in the interface structures also influenced growth rates. Figure 2.12 exhibits ZnSe thickness as a function of the growth time. The thickness was determined through analyses of interference fringes and satellite peaks appeared in x-ray diffraction patterns obtained from ZnSe single films and ZnSe-GaAs multilayered structures, respectively. It is clearly seen that the growth rates, which are determined from the slopes, depend strongly on the starting precursor, that is, the growth rate in the Zn-initiated growth is much faster than that in the Se-initiated growth. The growth rate estimated from a thick ZnSe layer about 0.4-μm thick is 30 Å/min and this value agrees well with that of the Se-initiated growth. Therefore, the growth rate is not suppressed by the DMSe-exposure but enhanced by the DEZn-exposure.

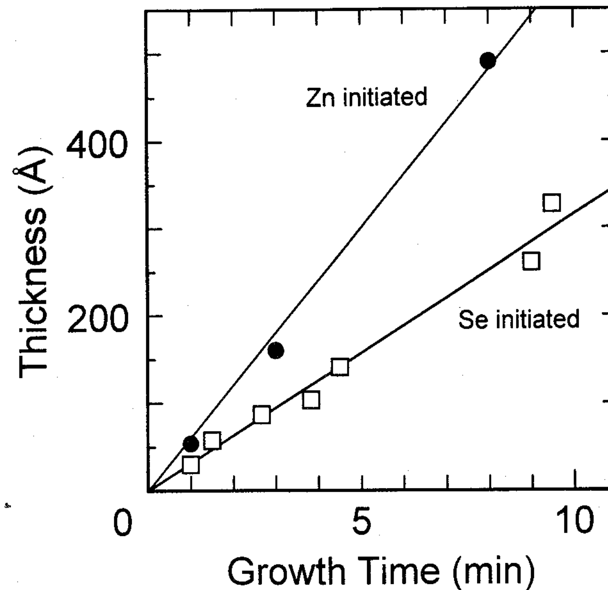

Figure 2.12: ZnSe thickness as a function of the growth time. The Zn-initiated growth has the much faster growth rate, which is determined from the slope, than the Se-initiated growth does.

In order to elucidate the cause of the growth rate enhancement, we refer again to the results of the x-ray CTR measurements. As mentioned previously, in the Zn-initiated growth, interdiffusion of Ga and Zn to several ML's occurs, while the As and Se distributions change quite abruptly at the interface. As a result, the donor-like bond of Ga-Se and the acceptor-like bond of Zn-As are induced in ZnSe and GaAs, respectively, to form dipoles very near the interface. Owing to the dipoles, the valence band offset at the ZnSe/GaAs interface is modified; that at the Se-initiated interface was estimated to be 0.6 eV by x-ray photoelectron spectroscopy (XPS), while that at the Zn-initiated interface was 1.0 eV [17]. On the other hand, Hall-effect measurements revealed that both ZnSe and GaAs were n-type and that their carrier concentrations were approximately 1×10^{11} and 5×10^{15} cm^{-3}, respectively. Using these carrier concentrations, the Fermi levels for ZnSe and GaAs were calculated to be 1.5 and 1.0 eV above the valence bands, respectively. These band parameters deduce band lineups as schematically shown in Fig. 2.13. For the Se-initiated growth [Fig. 2.13(b)], the Fermi levels for ZnSe and GaAs are located at almost the same energy level, and as a result, there is little distribution of the electron density in ZnSe. With respect to the Zn-initiated growth [Fig. 2.13(a)], when ZnSe is thin, an electron transfer from GaAs to ZnSe occurs to increase the electron density in ZnSe,

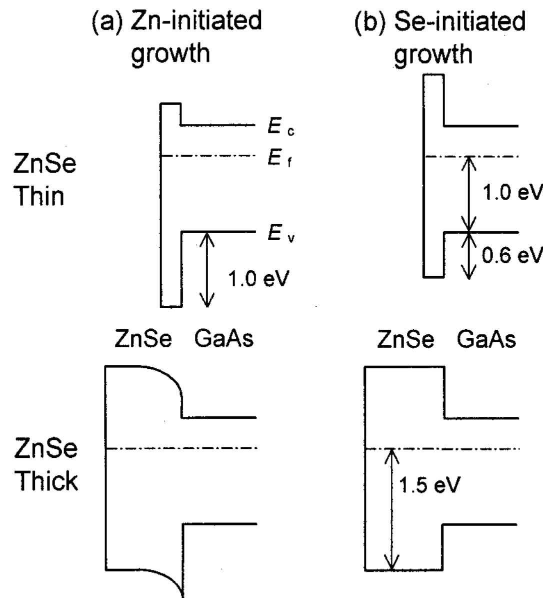

Figure 2.13: Band lineups of the ZnSe/GaAs heterostructures. The variations due to the thickness of ZnSe and the precursor initiating ZnSe growth are illustrated.

and hence, the Fermi level in ZnSe is raised. As ZnSe becomes thicker, band bending occurs to move the Fermi level to the original position and the electron density at the growth front approaches the original value, 1×10^{11} cm^{-3}. We consider, at present, that this increase of the electron density in ZnSe at early stages of the growth is responsible for the growth rate enhancement. In particular, attention should be paid to an interaction between electrons and DEZn, because the growth condition employed in this study is a Se-overpressure condition. It has been found through a mass analysis using a quadrupole mass spectrometer that DEZn does not decompose completely at the growth temperature of 450°C, which implies that the Zn atoms adsorbed at the surface are accompanied by hydrocarbons. Since Zn is positively polarized in the C-Zn bonds, electrons at the surface are easily attracted by Zn and eliminate the C-Zn bonds. Owing to an excess of Se in the growth ambient, the elimination of the C-Zn bonds might immediately be followed by the bonding of Zn with Se. By this mechanism, a higher density of electrons results in a faster growth rate. The above discussion suggests that the increase of the growth rate due to electrons is a characteristic of MOVPE and will not be observed in MBE.

The growth rate enhancement through alkylzinc elimination has also been observed by irradiation of photons with energies greater than the bandgap during MOVPE, where photogenerated carriers are considered to play an important role in enhancing the growth rate [19]. Although it has not been clear in photoassisted MOVPE whether electrons or holes are responsible for the decomposition of alkylzinc, the mechanism proposed here for the growth rate enhancement in the Zn-initiated growth does not contradict the conclusion from photoassisted MOVPE.

Similar experiments were also carried out using Ga-terminated GaAs which was completed by supplying TEGa to the amount corresponding to 1 atomic layer. However, the influence of the starting surface atoms on the nucleation of ZnSe was not found, indicating that the phenomena observed in this study were governed by the precursor initiating the ZnSe growth. From another point of view, a GaAs surface initially terminated by Ga and that terminated by As are considered to have resulted in the same structure after the exposure to DEZn or DMSe. This hypothesis is validated by the following reported experimental results. Zn reacts with As to synthesize Zn_3As_2, which is a volatile compound easily evaporated above 360°C [20]. Therefore, as a result of the reaction between DEZn and As terminating the GaAs surface, As-terminated GaAs turns into Ga-terminated GaAs already before the ZnSe growth. On the other hand, it has been reported that whatever the initial surface reconstructions are, Se-exposure below 550°C under ultra high vacuum results in GaAs with a (2×1) Se-terminated surface [21]. In the present study, the durations of the DEZn- and the DMSe-exposure seem to be sufficiently long to complete reactions like the above examples. Therefore, if the durations for these exposures are shorter, differences due to the initial surface atoms of GaAs may be detected.

2.4.4 Nucleation processes during quasi-homoepitaxial growth

In this section, the nucleation process on a thick ZnSe layer where the growth is a simulation of the homoepitaxial case is described.

The atomically flat surfaces shown in Figs. 2.7(b) and 2.10 are indicative of 2D growth. More precisely, the presence of the 2D nuclei in Fig. 2.7(b) provides important evidence that the growth is not in the step flow mode but in the 2D nucleation mode and proceeds layer-by-layer. This is because if the growth is the step flow growth, the ZnSe surface should be covered homogeneously with atomically flat terraces and ML steps without 2D

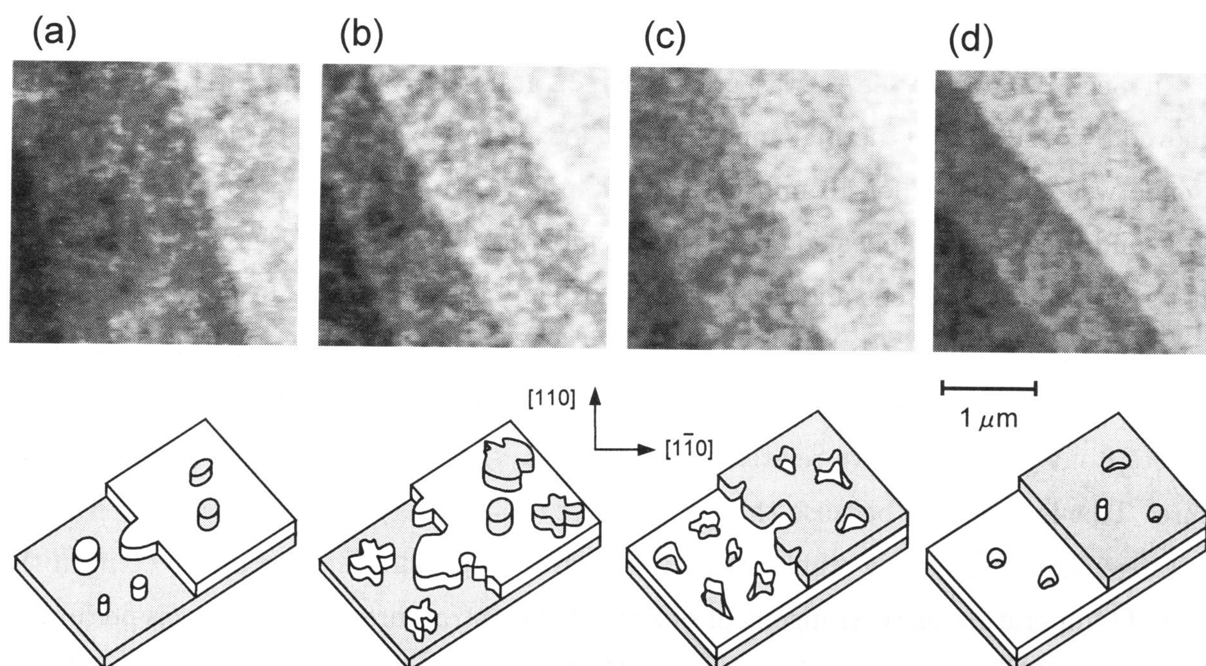

Figure 2.14: AFM images and schematic views of the formation process of 1 ML ZnSe.

nuclei. Since the growth phase cannot be the same at the atomic level in the entire area of the surface, it is possible to observe several stages during 1 ML formation though 2D layer-by-layer growth at different positions on the same layer. Figure 2.14 shows AFM images and schematic views, deduced from the images, of the formation process of 1 ML ZnSe. At first, 2D islands are nucleated on terraces [Fig. 2.14(a)]. Then the nucleated islands grow [Fig. 2.14(b)] and coalesce with each other [Fig. 2.14(c)]. The detailed observation around the step edges showed the formation of denuded zones, where 2D nucleation does not occur, indicating that migrating species in the area are preferably incorporated into steps at lower sides or islands at upper sides. The width of the denuded zone is approximately 60 nm, implying that the net migrating length of adatoms at 450°C is about half of the width, 30 nm. Therefore, it is expected that the use of a substrate with terraces narrower than 60 nm, which corresponds to the misorientation higher than 0.3°, results in the step flow growth. Finally, as shown in Fig. 2.14(d), 1 ML of ZnSe covers almost all of the surface, and the cycle is repeated.

2.5 Post-Growth Annealing

In Sec. 2.3, where GaAs was grown homoepitaxially, 2D islands were successfully removed by post-growth thermal annealing. Following this example, post-growth annealing of ZnSe was conducted for 10 min under DMSe flow. An AFM image of ZnSe grown at 450°C and successively annealed at the same temperature is shown in Fig. 2.15. Atomically flat terraces with ML steps and large 2D islands can clearly be seen. Comparing with the as-grown surface [Fig. 2.7(b)], it is found that annealing effectively has small islands such as that marked ② in Fig. 2.7(b) (typically 20 nm in diameter) migrated from a terrace to a step but cannot remove relatively large islands such as that marked ③ in the same figure. This is probably because the temperature of 450°C is not high enough to enhance rearrangement of relatively stable structures such as large islands. In order to confirm the effect of temperature on rearrangement of ZnSe surface structures, annealing was performed at 400 and 500°C against samples grown at 450°C. As expected, an annealing temperature of 400°C is too low for significantly changing the surface morphology and even small islands were still observable after the annealing. On the other hand, annealing at 500°C resulted

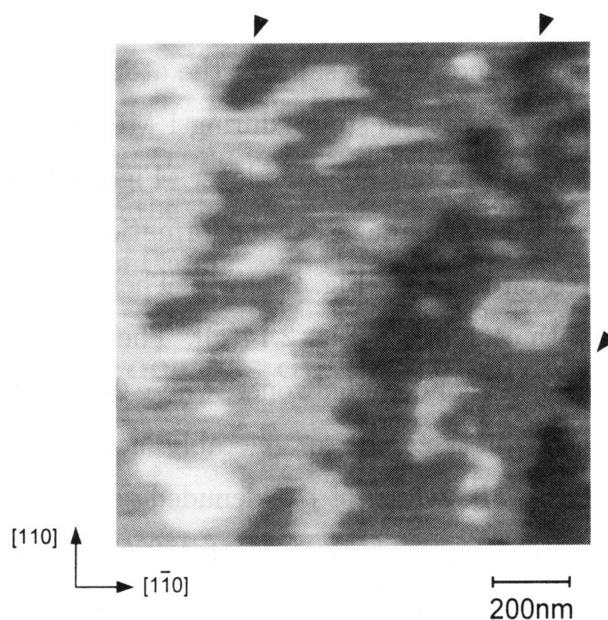

Figure 2.15: AFM image of ZnSe grown at 450°C followed by annealing at the same temperature in the Se ambient for 10 min. Film thickness is 100 Å. Arrowheads indicate 1 ML steps.

in degradation of the surface morphology; that is, fine structures with roughness of 3 ML appeared, and 10-Å-deep holes came to be observed in places. Since the vapor pressure of Se is higher than that of Zn, Se evaporates from the ZnSe surface predominantly, leaving the ZnSe surface rough. These results indicate that under the conditions employed in this study, 450°C is an optimal annealing temperature determined by competition between realization of large diffusion coefficient and prevention of Se evaporation.

Post-growth annealing at 450°C, which gives the best results for ZnSe grown at 450°C, was also performed with ZnSe layers grown at 400 and 500°C. However, an atomically flat surface could not be obtained for these samples; annealing at 450°C resulted in formation of 10-Å-deep holes on the surface of ZnSe grown at 400°C, while it induced no change in the surface structures of ZnSe grown at 500°C. Taking into account the above results for ZnSe grown at 450°C, it is concluded that, although annealing at 450°C is indeed suitable for obtaining an atomically flat surface, the annealing temperature must be below the growth temperature and the surface of as-grown ZnSe itself must be smooth. The condition which satisfies this situation is growth and post-growth annealing at 450°C.

Since the annealing effectively rearranges small structures, as discussed with Fig. 2.15, it may give more clear images of the growth processes with preserving essential features of surface structures. Therefore, we shall, again, show the formation process of 1 ML ZnSe using a sample grown and annealed at 450°C. Similar images using as-grown ZnSe have already been demonstrated in Fig. 2.14. Figure 2.16 illustrates the AFM images of the ZnSe surfaces during the layer-by-layer growth. Islands smaller than 20 nm are hardly observed because annealing at 450°C removed them. As a result, well-defined surfaces were obtained; island formation, growth, coalescence, and formation of 1 ML ZnSe are seen much more clearly than in Fig. 2.14.

2.6 Summary

Preparation of the GaAs surface for the ZnSe growth and the nucleation processes during ZnSe heteroepitaxy on GaAs(001) by MOVPE were described. The growth modes of ZnSe on the atomically flat GaAs surface were 2D or 3D below or above 450°C, respectively. In particular, an atomically flat surface could be obtained at 450°C. It was demonstrated that the initial nucleation at 450°C depended on the source precursor starting the ZnSe

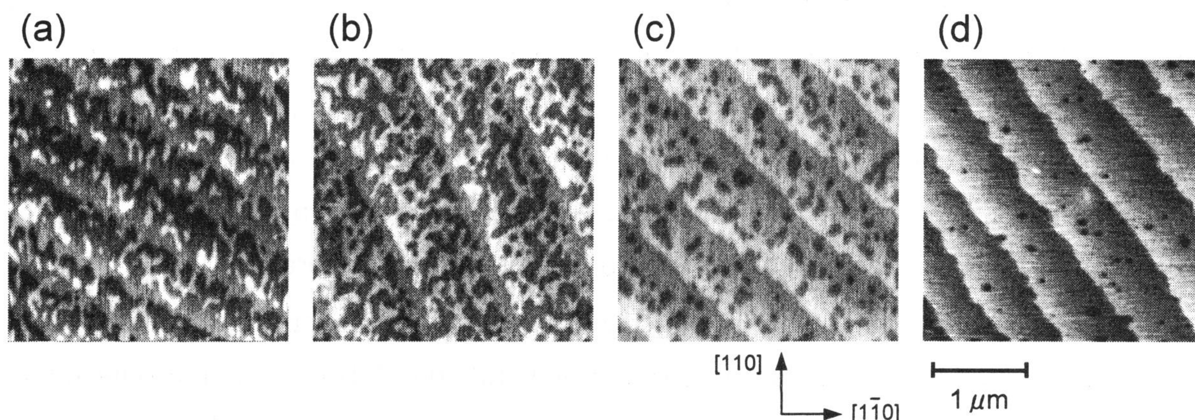

Figure 2.16: AFM images of the formation process of 1 ML ZnSe. The sample was grown and successively annealed at 450°C.

growth. The variation in the initial nucleation processes due to the starting precursors was ascribed to the difference of the interface structures. With respect to the nucleation on thick ZnSe layers, the 2D layer-by-layer growth has clearly been observed for the first time.

It is interesting to note that ZnSe can be grown two-dimensionally from a very early stage of the growth. This characteristic is favorable for the control of the band offsets via the atomic level control of the interface atomic configuration, and used in the next chapter.

References

[1] D. Li, M. Gonsalves, N. Otsuka, J. Qiu, M. Kobayashi, and R. L. Gunshor, Appl. Phys. Lett. **57**, 449 (1990).

[2] L. H. Kuo, K. Kimura, T. Yasuda, S. Miwa, C. G. Jin, K. Tanaka, and T. Yao, Appl. Phys. Lett. **68**, 2413 (1996).

[3] K. Oda and T. Nakayama, Jpn. J. Appl. Phys. **31**, 2359 (1992).

[4] M. C. Tamargo, J. L. deMiguel, D. M. Hwang, and H. H. Farrell, J. Vac. Sci. Technol. B **6**, 784 (1988).

[5] S. Guha, H. Munekata, F. K. LeGoues, and L. L. Chang, Appl. Phys. Lett. **60**, 3220 (1992).

[6] S. Guha, H. Munekata, and L. L. Chang, J. Appl. Phys. **73**, 2294 (1993).

[7] Throughout this study, AFM observations were carried out *ex situ* under the contact mode using a Seiko Instruments SPI3700 system.

[8] A. Koukitu and T. Taki, Appl. Surf. Sci. **112**, 63 (1997).

[9] M. Kasu and N. Kobayashi, Appl. Phys. Lett. **62**, 1262 (1993).

[10] I. Kamiya, D. E. Aspnes, H. Tanaka, L. T. Florez, J. P. Harbison, and R. Bhat, Phys. Rev. Lett. **68**, 627 (1992).

[11] F. Reinhardt, W. Richter, A. B. Müller, D. Gutsche, P. Kurpas, K. Ploska, K. C. Rose, and M. Zorn, J. Vac. Sci. Technol. B **11**, 1427 (1993).

[12] H. Mitsuhashi, I. Mitsuishi, H. Kukimoto, J. Crystal Growth **77**, 219 (1986).

[13] M. A. Haase, J. Qiu, J. M. DePuydt, and H. Cheng, Appl. Phys. Lett. **59**, 1272 (1991).

[14] H. Jeon, J. Ding, W. Patterson, A. V. Nurmikko, W. Xie, D. C. Grillo, M. Kobayashi, and R. L. Gunshor, Appl. Phys. Lett. **59**, 3619 (1991).

[15] M. Shinohara, M. Tanimoto, H. Yokoyama, and N. Inoue, J. Crystal Growth **145**, 113 (1994).

[16] H. Yokoyama, M. Tanimoto, M. Shinohara, and N. Inoue, Jpn. J. Appl. Phys. **33**, L1292 (1994).

[17] The detailed results are shown in the next chapter.

[18] D. Li and M. D. Pashley, J. Vac. Sci. Technol. B **12**, 2547 (1994).

[19] Sz. Fujita and Sg. Fujita, Appl. Surf. Sci. **86**, 431 (1995), and references therein.

[20] B. Chelluri, T. Y. Chang, A. Ourmazd, A. H. Dayem, J. L. Zyskind, and A. Srivastava, Appl. Phys. Lett. **49**, 1665 (1986).

[21] S. Takatani, T. Kikawa, and M. Nakazawa, Phys. Rev. B **45**, 8498 (1992).

Chapter 3

Control of Interface Properties in ZnSe-on-GaAs Heterovalent Heterostructures

3.1 Introduction

The band offset at a heterojunction interface plays an important role in determining the carrier transport and confinement properties. Although it has been recognized to be an intrinsic property for a given heterostructure, a number of recent works revealed that it is a function of the interfacial atomic configuration [1-7]. In particular, large variations in the band offsets are expected at heterovalent interfaces, owing to the existence of nonoctet bonds which form donor and acceptor states. If the microscopic interface atomic configuration, that is, the position of the donor and acceptor bonds at the interface, can be controlled in some way, that will lead to the tunability of the band offsets.

The largest variation of the valence band offset ever achieved is about 0.6 eV in the ZnSe-on-GaAs(001) [ZnSe/GaAs(001)] system [2]. It was reported that the interface composition can be controlled by the Zn/Se flux ratio employed during molecular beam epitaxy (MBE), resulting in a variation of the valence band offsets from 0.58 (Se-rich condition) to 1.20 eV (Zn-rich condition). In that study, however, the difference in the beam pressure ratio modifies the bulk properties as well as the interface properties and, thus, strict control of the heterointerface itself has not been achieved yet.

In this chapter, the tunability of the band offsets at the ZnSe/GaAs heterointerfaces through the control of the interface atomic configuration is demonstrated. For this, the modification of a GaAs surface was completed prior to the growth of ZnSe, and the growth

conditions for both ZnSe and underlying GaAs remained unchanged regardless of the GaAs surface treatment. Therefore, discussions are concentrated on the interface chemistry without consideration of the bulk properties of ZnSe and GaAs. X-ray photoemission spectroscopy (XPS), which has often been utilized for studying the band offsets [2, 6-8], is used in order to evaluate the valence band offsets and to reveal its tunability [9]. The tunability is also confirmed from the electrical properties of n-ZnSe/p^+-GaAs heterojunction diodes (HD's). The presence of electronic dipoles at the interface, which are responsible for the tunability of the band offsets, is proved structurally by the x-ray crystal truncation rod (CTR) scattering measurement and optically by the fast Fourier-transformed photoreflectance (FFT-PR) measurement.

3.2 Preparation of ZnSe/GaAs Heterointerfaces

The detailed preparation procedures of the underlying GaAs layer were described in Secs. 2.2 and 2.3. In order to compensate the chemical valence mismatch at the ZnSe/GaAs heterovalent interface, the same number of donor and acceptor states must exist at the interface. As simple examples to satisfy this condition, a mixed Ga-Zn plane with 50-50 composition and a As-Se plane with the same composition at the interface have already been introduced in Fig. 1.2. The resultant valence band offsets for the former and the latter have been calculated to be 1.59 and 0.62 eV, respectively, in Ref. [2], and 1.75 and 0.72 eV, respectively, in Ref. [3]. To realize variation of the interface structure experimentally, in this study, the GaAs surfaces were exposed to Zn or Se precursors, *i.e.*, diethylzinc (DEZn) or dimethylselenium (DMSe), at 450°C prior to ZnSe growth. The surfaces of the GaAs epilayers after these procedures were confirmed, by atomic force microscopy, to preserve atomically flat terraces and monolayer (ML, 1 ML = 2.8 Å) steps.

Then, ZnSe layers were grown at 450°C. Molar flow rates of DEZn and DMSe were 1.2 and 12 μmol/min, respectively. As mentioned in the previous chapter, these conditions make the ZnSe surface flat to the atomic level. The durations of the Zn- and Se-exposure were varied within the limits that the atomically flat surface of the ZnSe epilayers is retained. This is because the atomically flat surface of the thin film is a good index of an abrupt interface.

3.3 Control of Band Offsets

3.3.1 XPS measurements

experimental details

ZnSe layers 30 – 50-Å thick were grown for XPS. The XPS measurements were performed *ex situ* using a Shimadzu ESCA-1000 system. A schematic diagram is viewed in Fig. 3.1. The system was equipped with an Al $K\alpha$ (1486.6 eV) x-ray source and a hemispherical electron energy analyzer. The samples were always placed so that the analyzer detected photoelectrons vertically emitted from the sample surface. With this experimental configuration, the region detectable by XPS was about 45 Å from the sample surface. In order to avoid the influence of the surface contamination due to the exposure to air on XPS spectra, the ZnSe surface was lightly etched with Ar^+ after being loaded into the XPS chamber. Figure 3.2 is a typical example of the XPS spectra, in which the ZnSe thickness is approximately 30 Å. The thickness of ZnSe (30 Å) enabled us to detect photoelectrons from both sides of the ZnSe/GaAs interface simultaneously. The detected signals were 3d core levels of Zn, Se, Ga, and As. We can determine the solid composition from the relative intensity ratio of the signals and the valence band offset from the separation between the peak energies of the signals.

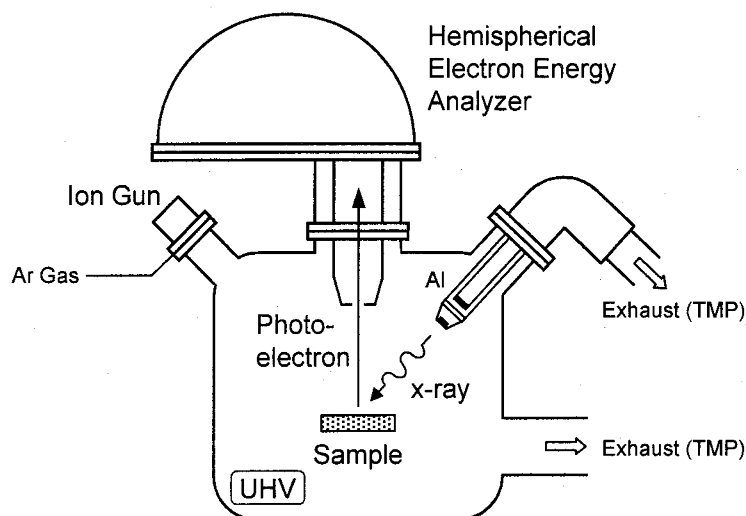

Figure 3.1: Schematic diagram of the XPS system.

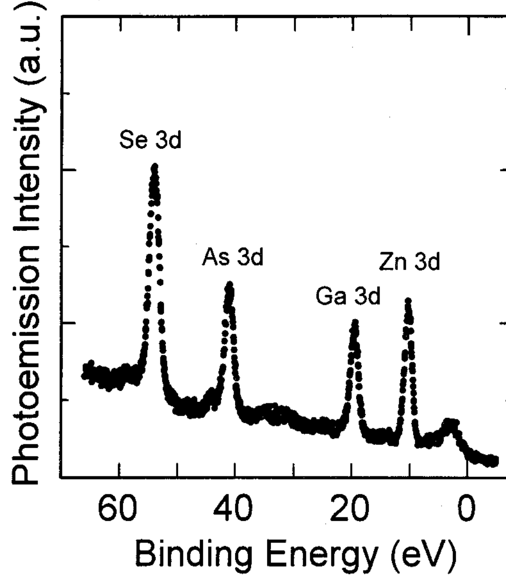

Figure 3.2: Typical XPS spectrum. The thickness of ZnSe is 30 Å, which makes it possible to observe 3*d* core levels from all constituents at the same time.

Let us explain how to extract the valence band offsets from the XPS profile. The ZnSe-GaAs heterostructure possesses a type-I energy band alignment as schematically illustrated in Fig. 3.3, where the core levels as well as the valence and conduction bands are shown. Referring to Fig. 3.3, we find that the valence band offset ΔE_{v} is determined by

$$\Delta E_{\mathrm{v}} = (E_{\mathrm{CL}}^{\mathrm{GaAs}} - E_{\mathrm{v}}^{\mathrm{GaAs}}) - (E_{\mathrm{CL}}^{\mathrm{ZnSe}} - E_{\mathrm{v}}^{\mathrm{ZnSe}}) - (E_{\mathrm{CL}}^{\mathrm{GaAs}} - E_{\mathrm{CL}}^{\mathrm{ZnSe}}), \tag{3.1}$$

where E_{CL} and E_{v} denote the core level and the valence band maximum binding energies for the indicated material. $E_{\mathrm{CL}}^{\mathrm{GaAs}} - E_{\mathrm{v}}^{\mathrm{GaAs}}$ and $E_{\mathrm{CL}}^{\mathrm{ZnSe}} - E_{\mathrm{v}}^{\mathrm{ZnSe}}$ are the known constants measured in bulk standards and, therefore, the measurements of the core level energy separation, $E_{\mathrm{CL}}^{\mathrm{GaAs}} - E_{\mathrm{CL}}^{\mathrm{ZnSe}}$, by XPS lead to the determination of the valence band offsets. In this study, as shown in Fig. 3.2, 3*d* core levels of Zn, Se, Ga, and As were detected at the same time. Thus, four different separations may be used to obtain the valence band offset: Ga 3*d* – Zn 3*d*, Ga 3*d* – Se 3*d*, Zn 3*d* – As 3*d*, and As 3*d* – Se 3*d*. Here, the valence band offsets were extracted chiefly from the Ga 3*d* – Zn 3*d* separation and, for a compliment, from the As 3*d* – Se 3*d* separation. Concerning Ga 3*d* and Zn 3*d* levels, $E_{\mathrm{CL}}^{\mathrm{GaAs}} - E_{\mathrm{v}}^{\mathrm{GaAs}}$ and $E_{\mathrm{CL}}^{\mathrm{ZnSe}} - E_{\mathrm{v}}^{\mathrm{ZnSe}}$ are found in literatures to be 18.81 [10] and 8.90 eV [11], respectively. In these Refs. [10] and [11], the core level energy position was defined to be the center of the peak width at half of the peak height and this definition was followed in this study.

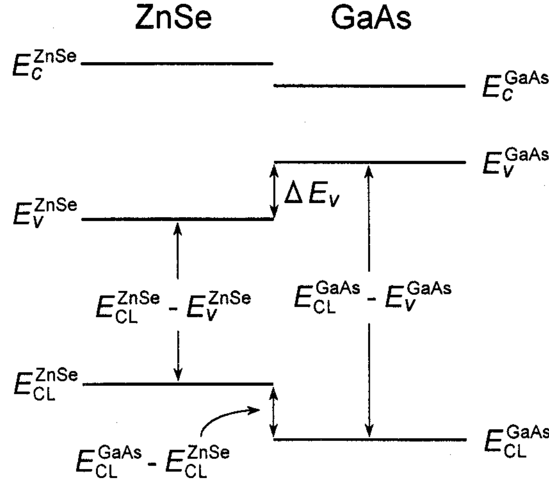

Figure 3.3: Schematic energy band diagram of the ZnSe-GaAs heterostructure. E_c is the conduction band minimum binding energy, and other notations are explained in the text. The junction is type-I and three quantities, that is, $E_{CL}^{GaAs} - E_{V}^{GaAs}$, $E_{CL}^{ZnSe} - E_{V}^{ZnSe}$, and $E_{CL}^{GaAs} - E_{CL}^{ZnSe}$, are necessary to determine ΔE_v.

Here, possible errors included in the present experimental procedure are discussed. First, errors derived from the XPS measurement itself are pointed out. The reproducibility of binding energies by XPS measurements is 0.1 eV in general. Therefore, the estimated valence band offsets may also include an error of approximately 0.1 eV. Also, if chemical shifts at the interface occur, the valence band offset calculated from Eq. (3.1) apparently changes. In this study, however, the contribution of chemical shifts to the XPS spectra seems to be minor and we neglected it. This is because quantitatively consistent results were obtained from the Ga 3*d* – Zn 3*d* separation and the As 3*d* – Se 3*d* separation. Furthermore, no change in the Zn, Se, Ga, and As 3*d* line shapes was observed for any of the samples, which supports the above conclusion. It has been reported that chemical shifts were also small in ZnSe/GaAs heterostructures grown by MBE [12], implying that chemical shifts do not appear explicitly in the ZnSe-GaAs material system.

Another possible error in estimation of the valence band offset is caused by the material system; strain due to the difference in the lattice parameters modifies the energy bands, as is well known. Since ZnSe was grown on the GaAs substrates and the thickness of ZnSe (30 – 50 Å) is much thinner than the critical layer thickness of 1500 Å [13], the ZnSe layer

is strained to achieve pseudomorphic growth. The lattice parameter of ZnSe is 5.6686 Å, while that of GaAs is 5.6533 Å at room temperature. Thus, the strain is compressive. The effect of the compressive strain on the energy band of ZnSe was estimated with the model-solid theory proposed by Van de Walle *et al.* [14, 15] (see Appendix for the detailed calculation procedure). As a result, it was found that the compressive stain in ZnSe makes the valence band offset smaller by 3.6 meV for heavy holes and larger by 10.5 meV for light holes. However, these quantities are very small, compared with the variation of the valence band offset shown later, and we neglected the influence of the strain on the measured valence band offset.

To obtain a depth profile, the ZnSe layer thickness was reduced by Ar^+ sputtering in the XPS chamber. Figure 3.4 shows schematic views of photoelectron emission with different thicknesses of ZnSe. The region detectable by the present XPS measurements is about 45 Å from the surface. Therefore, when ZnSe is thick [$>\sim$30 Å, Fig. 3.4(a)], Ga and As 3*d* signals give information in the vicinity of the interface and Zn and Se 3*d* signals show bulk properties of ZnSe. As the thickness of ZnSe is reduced [Fig. 3.4(b)], Ga and As 3*d* signals begin to include the GaAs bulk properties and Zn and Se 3*d* signals indicate the interface properties on the ZnSe side. The ZnSe thickness was estimated from the

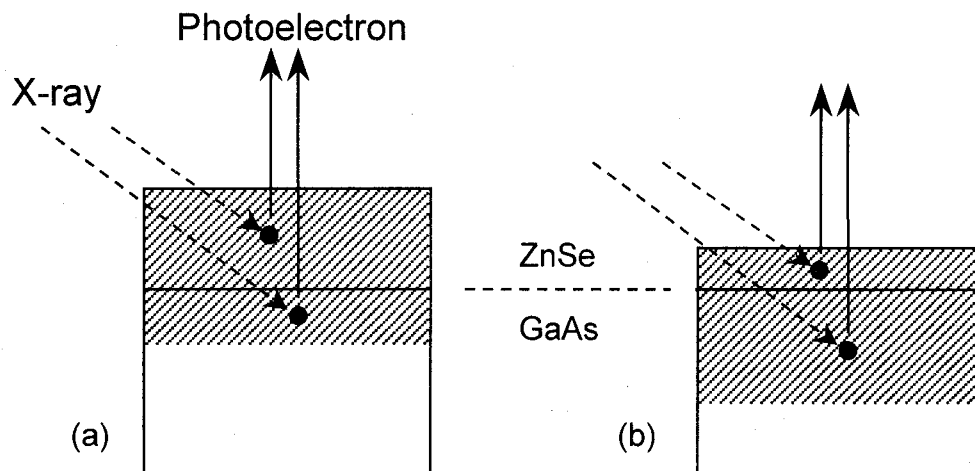

Figure 3.4: Schematic views of photoelectron emission from ZnSe/GaAs heterostructures with (a) thick and (b) thin ZnSe.

attenuation of the Zn and Se 3*d* photoemission.

results and discussion

The heterostructures were fabricated with variation of the amount of either DEZn or DMSe for the GaAs surface treatment. It must be noted that the amount of DEZn was adjusted by changing the duration rather than the flow rate. If not, at a higher flow rate, deposition of Zn takes place and the morphology of ZnSe becomes poor as shown in Fig. 2.9.

Figure 3.5 summarizes the integrated intensity ratios of the XPS signals originating from the 3*d* core levels, I_{Zn}/I_{Se} and I_{Ga}/I_{As}, as a function of ZnSe thickness. This figure corresponds to the depth profile as explained with Fig. 3.4. Both I_{Zn}/I_{Se} and I_{Ga}/I_{As} were normalized so as to exhibit unity in each bulk standard. Even in ZnSe and GaAs bulk standards, the intensity ratios showed scattering of about 10% and, therefore, the empiri-

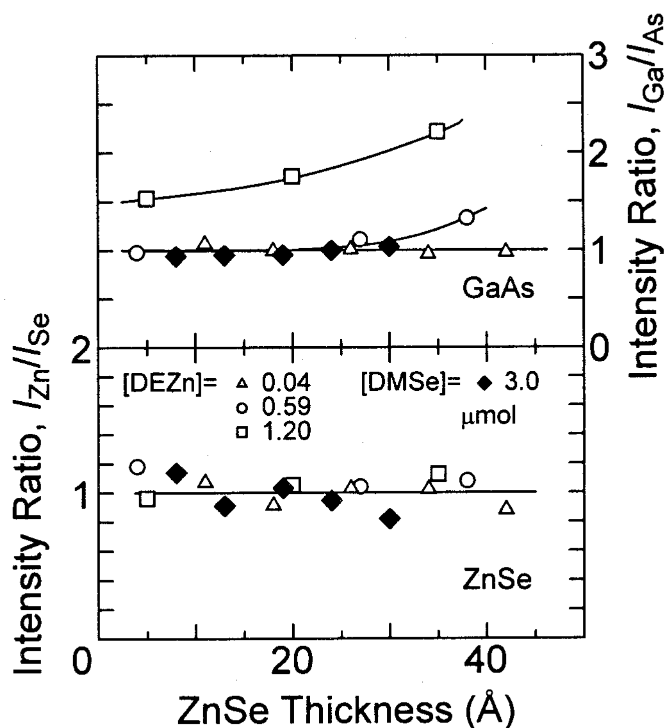

Figure 3.5: Depth profile of the integrated 3*d* photoemission intensity ratios in the ZnSe/GaAs heterostructures. Before the growth of ZnSe, the GaAs surfaces were exposed to either DEZn or DMSe by the amount indicated in the figure at 450°C. Both I_{Zn}/I_{Se} and I_{Ga}/I_{As} were normalized so that they exhibit unity in each bulk standard.

cally deduced accuracy of this experiment is approximately 10%. From the figure, I_{Zn}/I_{Se} is found to stay at around unity, regardless of the GaAs surface treatments and the ZnSe layer thicknesses. Although some scattering of data is observed, its distribution is random and the degree of scattering is comparable to the experimental resolution. With respect to I_{Ga}/I_{As}, that depends on the GaAs surface treatments. The Se-exposure does not influence the composition of GaAs; I_{Ga}/I_{As} remains unity at any ZnSe thickness. When GaAs is exposed to DEZn, on the other hand, I_{Ga}/I_{As} is higher for a larger thickness of ZnSe. Furthermore, this characteristic becomes pronounced as the amount of DEZn increases. Since, when ZnSe is thicker, the observed I_{Ga}/I_{As} value includes more information regarding the Ga and As atomic configuration at the ZnSe/GaAs interface, this behavior of I_{Ga}/I_{As} indicates that the local relative solid composition at the interface is Ga-rich. The cause for this is considered as follows: The Zn-exposure to the GaAs surface brings about the formation and evaporation of a volatile compound of Zn_3As_2 [16], leaving the surface Ga-rich. The subsequent growth of ZnSe confines the surface Ga at the interface. The detailed interface structure will be discussed later in Sec. 3.4.

The Zn- or Se-exposure was carried out not only for the As-terminated GaAs (denoted by As:GaAs) discussed above, but also for Ga-terminated GaAs (Ga:GaAs) which was completed by supplying triethylgallium (TEGa) to the amount corresponding to 1 atomic layer. The resultant interface compositions are shown in Fig. 3.6. Here, as the Ga/As interface composition, we adopted the XPS intensity ratio of I_{Ga}/I_{As} obtained from the heterostructures with thick ZnSe (> 30 Å), while for the Zn/Se interface composition, I_{Zn}/I_{Se} from thin ZnSe (< 15 Å) was used. As deduced from Fig. 3.4, the compositions estimated by this procedure well reflect the actual interfacial compositions. It is found from the figure that the Zn/Se ratio is independent of the surface treatment and the surface atoms of GaAs. In contrast, the Ga/As ratio increases as the duration of the Zn-exposure increases, which was already pointed out in Fig. 3.5, and the difference due to the starting surface atoms of GaAs is clearly observed. Namely, Ga:GaAs resulted in the more Ga-rich interface than As:GaAs did under the same Zn-exposure duration.

On the other hand, how do the formation processes of the interfaces stated above influence the band offsets? Figure 3.7 shows the dependence of the valence band offsets on the Zn- or Se-exposure duration, in which the atom terminating the GaAs surface is a parameter. The valence band offsets were determined from the XPS spectra for the

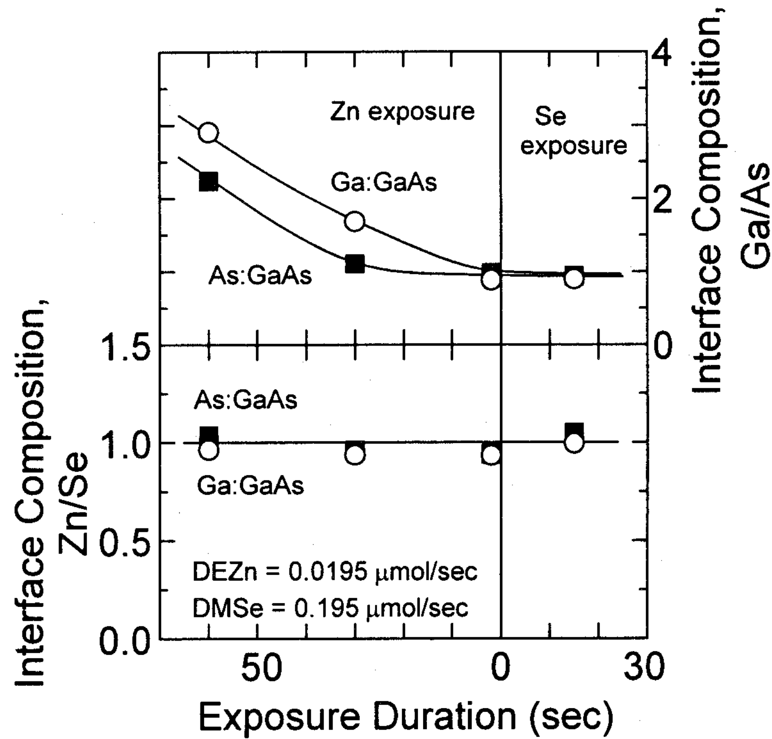

Figure 3.6: Variation of the interface composition as a function of the Zn- or Se-exposure duration. In addition to As-terminated GaAs (As:GaAs), Ga-terminated GaAs (Ga:GaAs) was investigated.

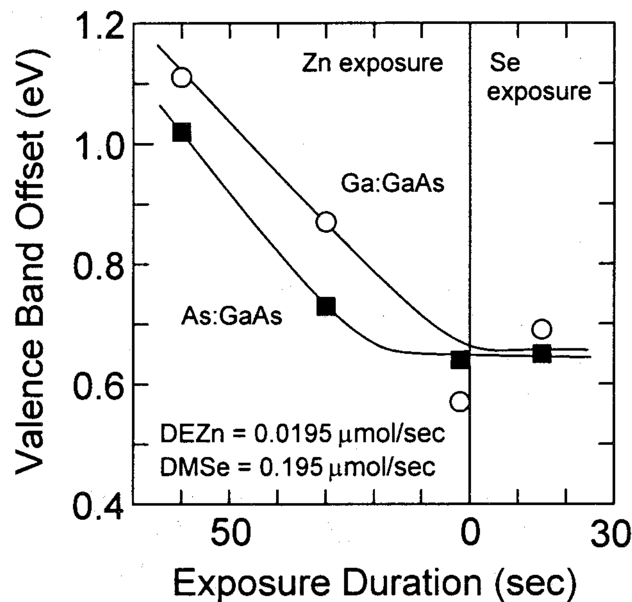

Figure 3.7: Dependence of the valence band offsets on the formation processes of the interfaces. The valence band offsets were determined from the XPS spectra for heterostructures with ZnSe 20 – 30-Å thick.

samples with ZnSe 20 – 30-Å thick, because the thickness in this region can minimize the influence of the chemical shift due to interfacial structures on the XPS signal, even if exists. It is clearly seen that the valence band offsets become large as the Zn-exposure duration increases and that this trend is pronounced with Ga:GaAs. The variation of the valence band offsets between 0.6 and 1.1 eV was achieved. It should be emphasized that this is the first demonstration of the capability of artificially controlling the band offsets through the interface engineering.

An interesting fact emerges from a comparison between Figs. 3.6 and 3.7. Both the Ga/As interface compositions and the valence band offsets increase as the Zn-exposure duration and depend on the GaAs surface atoms, suggesting a strong relation between them. Therefore, the valence band offsets were repotted as a function of the interface composition of Ga/As. The results are shown in Fig. 3.8. Here, in addition to the Zn- or Se-exposure of Ga:GaAs and As:GaAs, a new formation process of the interface, that is, thermal etching of the GaAs surface in H_2 at 630°C for 30 min, was examined and all results are summarized. As expected, the correlation between the interface composition and the valence band offsets is expressed by unique curve regardless of the procedures used for the interface preparation. In this sense, it is essential for controlling the band offsets

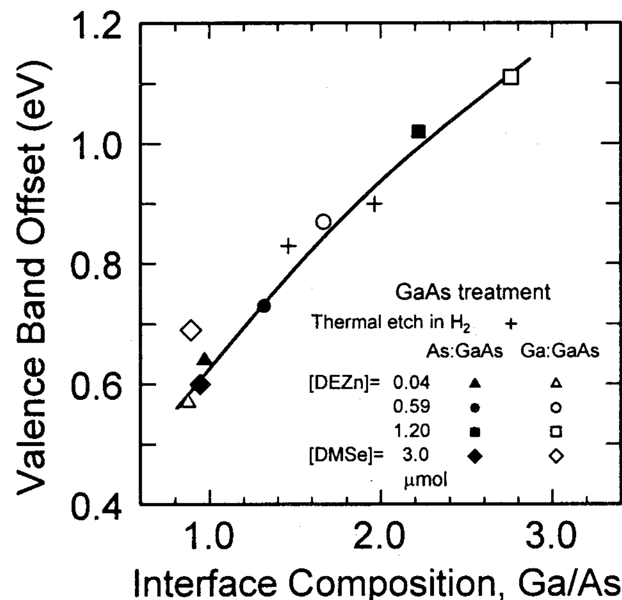

Figure 3.8: Estimated valence band offset as a function of the interface composition, Ga/As. In addition to the Zn- or Se-exposure of Ga:GaAs and As:GaAs, thermal etching in H_2 at 630°C for 30 min was examined and all results were summarized.

to modify the interface composition, Ga/As, and the method of surface treatment itself is not important.

3.3.2 Heterojunction diodes

In above section, the tunability of the band offsets was successfully demonstrated using thin ZnSe ($< \sim 50$ Å) on GaAs. In this section, using n-ZnSe/p^+-GaAs HD's, we will confirm that the tunability of the band offsets is preserved in the following thick-layer growth of ZnSe as well.

The diffusion potential, V_D, in a HD is generally a function of the band offset. V_D of an n-ZnSe/p^+-GaAs HD is deduced from

$$eV_D = E_g^{ZnSe} - \Delta E_v - \delta_{GaAs} - \delta_{ZnSe}, \tag{3.2}$$

where e is the elementary charge, E_g^{ZnSe} is the band gap of ZnSe, ΔE_v is the valence band offset and δ_{GaAs} and δ_{ZnSe} are the energy differences between the Fermi levels and the valence band edge in p^+-GaAs and the conduction band edge in n-ZnSe, respectively. Thus, the tunability of the band offset should result in that of V_D. The designed HD structure is n^+-ZnSe (1×10^{19} cm^{-3}) / n-ZnSe (1×10^{17} cm^{-3}) / p^+-GaAs (2×10^{19} cm^{-3}), as shown in Fig. 3.9. The p^+-GaAs buffer layer was obtained by Zn-doping with DEZn as a dopant. The n-ZnSe layer was grown at 400°C and doped with Ga using TEGa. The growth temperature of 400°C was 50°C lower than in the previous experiments in order to promote

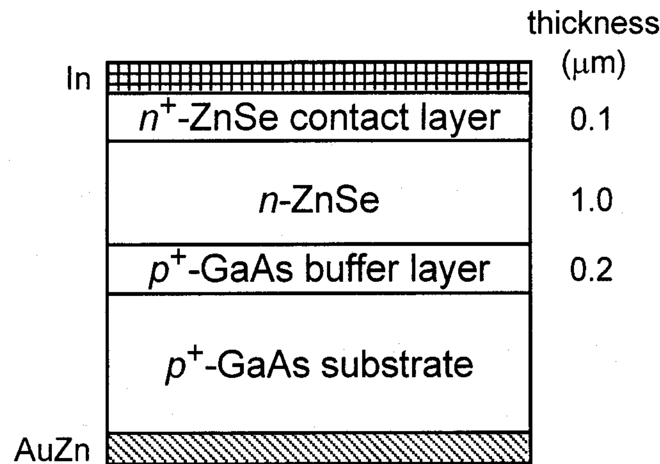

Figure 3.9: The HD structure used for the investigation of the tunability of the band offsets

the incorporation of Ga. Thickness of the n-ZnSe region was 1 μm. The n^+ conductivity for the 500-Å-thick ZnSe contact layer was achieved by I doping using ethyliodide, which is incorporated into ZnSe much more easily than Ga. This layer was grown at 350°C under photoassistance, and those conditions provided a carrier concentration of 2×10^{19} cm^{-3}. Au/AuZn and In metal electrodes were formed on p^+-GaAs and n^+-ZnSe, respectively, by vacuum deposition. Finally, mesa structures 1 mm in diameter were formed by conventional photolithography and chemical etching. The etching solutions for ZnSe and GaAs were [6 wt% $K_2Cr_2O_7$ in H_2O] : H_2SO_4 = 4 : 1 and H_2SO_4 : H_2O_2 : H_2O = 5 : 1 : 1, respectively.

The local compositions at the ZnSe/GaAs heterointerfaces in HD's were controlled by thermal etching (in H_2, 630°C, 30 min), that is, the properties of HD's with interfaces subjected to thermal etching or not are compared. Separate XPS experiments using ZnSe thin films (~40 Å) grown at 400°C confirmed that the compositional ratio of Ga/As and the valence band offset at the heterointerface with thermal etching were 2.0 and 0.92 eV, respectively, while those without thermal etching were 1.0 and 0.63 eV, respectively. These values agree reasonably well with the properties shown in Fig. 3.8, indicating that the lower growth temperature of ZnSe did not influence the formation processes of the interfaces and the interface structures remarkably.

The current-voltage (I-V) and capacitance-voltage (C-V) characteristics of the HD's measured at 300 K are shown in Fig. 3.10. The I-V curves [Fig. 3.10(a)] indicate clear rectifying characteristics with turn-on voltages of 0.30 and 1.01 V for the HD's with Ga/As = 2.0 and 1.0, respectively. Regarding the C-V measurements [Fig. 3.10(b)], the net donor concentrations in ZnSe were derived from the $1/C^2$ plot to be 5×10^{16} and 2×10^{17} cm^{-3} for the HD's with Ga/As = 2.0 and 1.0, respectively. The energy differences, δ_{ZnSe}, were calculated using the net donor concentrations as the carrier concentrations. Moreover, the diffusion potentials were extracted by extrapolation of the $1/C^2$ plot into $1/C^2 = 0$, which gives the voltage, $V_{\mathrm{D}} - 2k_{\mathrm{B}}T/e$ (k_{B} denotes the Boltzmann constant). Those were 1.50 and 1.95 V for the HD's with Ga/As = 2.0 and 1.0, respectively.

Using the experimental results, the valence band offsets were calculated from Eq. (3.2) and summarized in Table 3.1. Here, the energy difference of δ_{GaAs} was calculated based on the designed carrier concentration value in GaAs. The valence band offsets estimated from the C-V and XPS measurements agree well, but those from the I-V measurements,

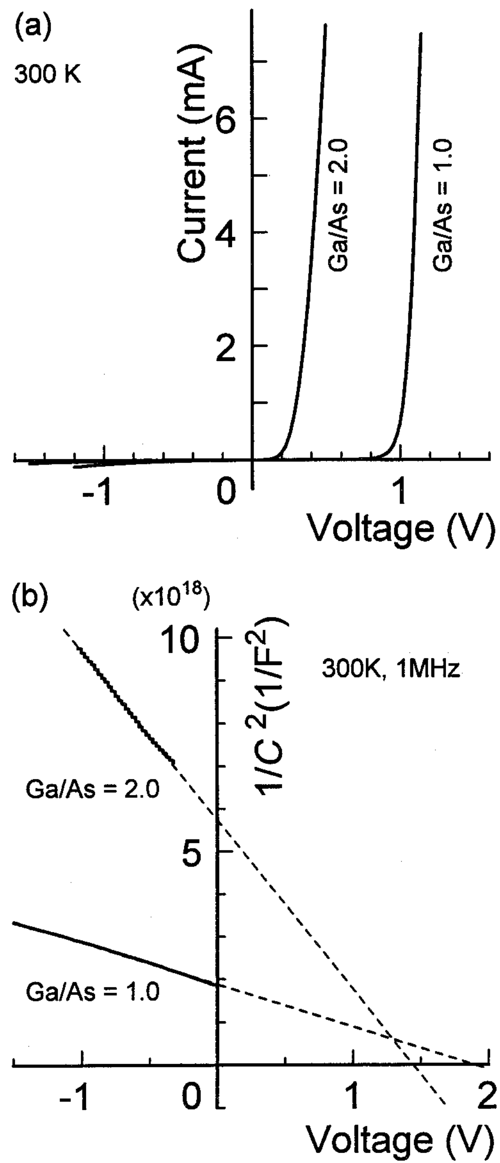

Figure 3.10: (a) *I-V* and (b) *C-V* characteristics of n-ZnSe/p^+-GaAs HD's measured at 300 K. The HD's have different interface compositions of Ga/As = 1.0 and 2.0.

Table 3.1: Valence band offsets estimated from XPS, I-V, and C-V measurements. Ga/As is the interface composition measured by XPS.

Ga/As	Valence band offset (eV)		
	XPS	I-V	C-V
2.0	0.92	2.31	1.15
1.0	0.63	1.64	0.75

which were calculated by substituting the turn-on voltage for the diffusion potential, are larger than the former. This discrepancy may be attributed to the difference between the turn-on voltage and the diffusion potential due to the existence of a tunneling current. In fact, the temperature dependence of the I-V characteristics indicated that the carrier transport in the HD's was dominated by the tunneling current. However, for three different measurements, larger valence band offsets were consistently obtained for the HD with the larger Ga/As, indicating that the tunability of the band offset is preserved in thick layers.

3.4 Interface Structures

The tunability of the band offsets presented in Sec. 3.3 was based on the control of the interface atomic compositions. In this section, in order to reveal the actual interface structures, the Zn, Se, Ga, and As distributions at and near the heterointerfaces are investigated in the atomic scale by means of the x-ray CTR scattering measurement.

experimental details

X-ray CTR is a rod (or a needle depending on the x-ray beam size) that appears around a Bragg diffraction spot in the reciprocal space as shown in Fig. 3.11, where the co-ordinate axes were defined as h, k, and l. CTR is caused by the abrupt truncation of a crystal at the surface and finite penetration depth of the x-ray [17,18]. In Fig. 3.11, the crystalline structure was assumed to be zinc-blende with the (001) surface, and consequently, the x-ray CTR scattering is elongated in the $[00l]$ direction. The x-ray CTR measurement has originally been developed for the assessment of surface structures. However, it has recently been demonstrated that the x-ray CTR scattering with the x-ray interference effect is a very powerful technique to reveal the layer structure, and even the crystal structure in the layer,

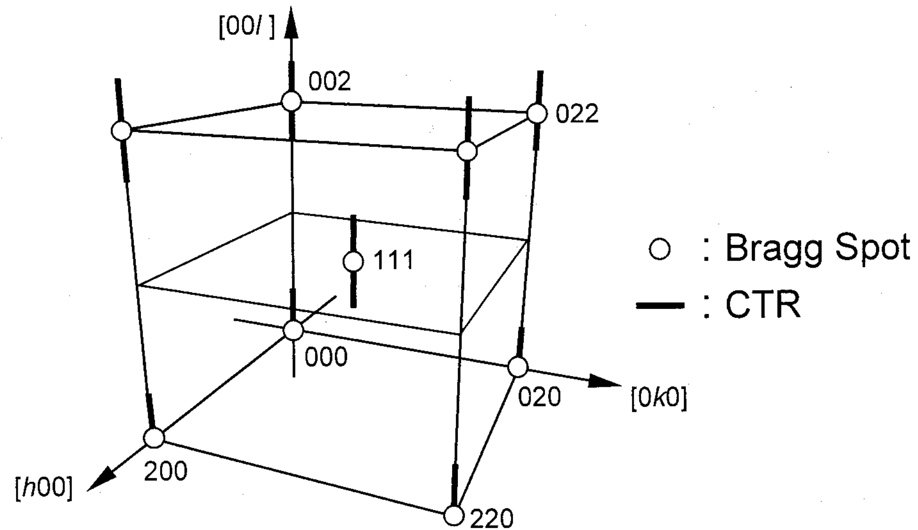

Figure 3.11: X-ray CTR scattering in the reciprocal space. The crystalline structure was assumed to be zinc-blende with the (001) surface

of heteroepitaxially grown samples in the atomic scale [19, 20]. From this background, the x-ray CTR measurement was applied for the investigation of the atomic configuration at the ZnSe/GaAs interfaces.

The schematic diagram of the measurement system is illustrated in Fig. 3.12. The measurement was carried out at the beam line $BL6A_2$ of the Photon Factory at Tsukuba using synchrotron radiation from the 2.5 GeV storage ring. The SiO_2 bent mirror excluded high frequency components of the x-ray and increased its intensity. The wavelength of the x-ray was adjusted to 1.600 Å by the triangular Si(111) monochromator. The CTR spectrum extending from the 004 Bragg spot was recorded by the Weissenberg camera with the imaging plate (IP) as a detector.

To analyze the interface structures, a model structure as shown in Fig. 3.13 was created, from which a theoretical CTR spectrum was generated using the kinematical theory [17, 18]. In the model, the parameters such as n_{Zn} (number of Zn ML's), n_{Se} (number of Se ML's), δ_{Zn} (distribution distance of Zn into Ga sublattices), δ_{Se} (distribution distance of Se into As sublattices), δ_{Ga} (distribution distance of Ga into Zn sublattices), δ_{As} (distribution distance of As into Se sublattices), x_{iZn} (Zn composition at Zn/Ga interface), x_{iSe} (Se composition at Se/As interface), x_{hZn} (Zn composition in ZnSe layer), x_{hSe} (Se composition in ZnSe layer) were considered. The distribution functions were assumed to be expressed as, *e.g.*,

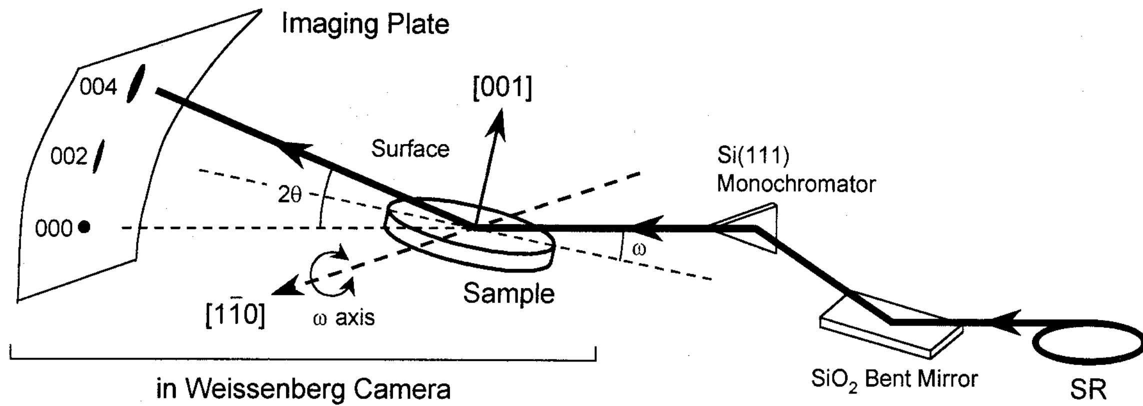

Figure 3.12: Schematic diagram of the measurement system of the x-ray CTR scattering.

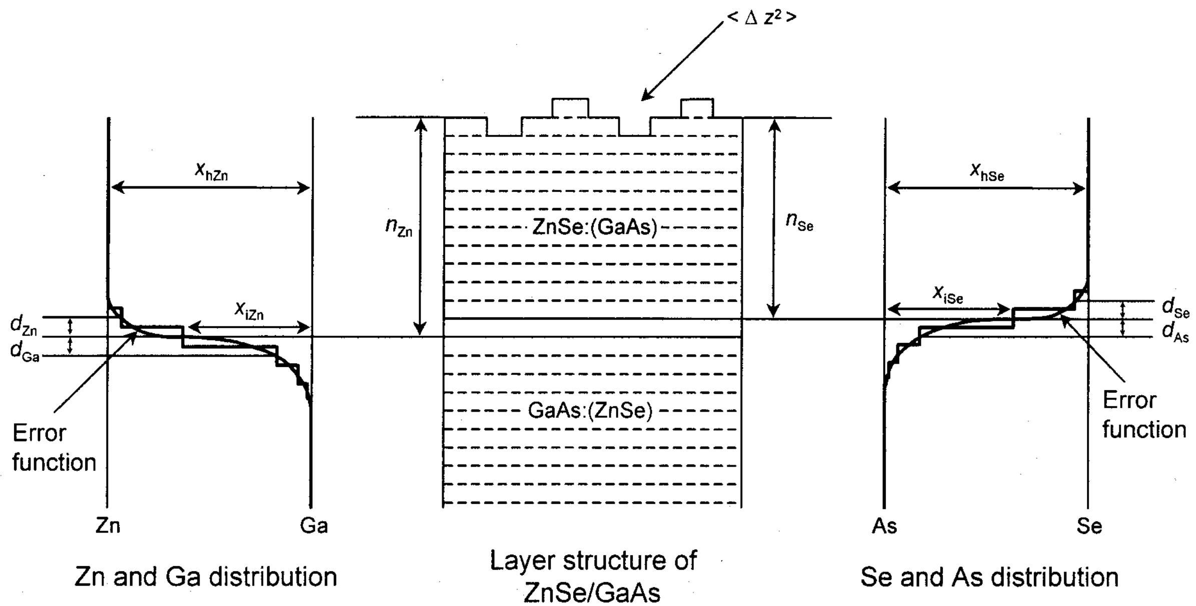

Figure 3.13: Model structure for ZnSe/GaAs with Zn/Ga and Se/As interdiffusion near the interface. Central figure is the model layer structure with ZnSe on top of GaAs. Left curve is the distribution of Zn and Ga, and the right curve is the distribution of As and Se. The distribution curve was assumed to be the error function with distance from the interface as a variable. The symbols are explained in the text.

in the case of the Se distribution, $x_{\rm hSe} = x_{\rm iSe}\{1-{\rm erf}(n/\delta_{\rm Se})\}$, where erf is the error function and n is the number of ML from the interface, *i.e.*, the distance from the interface in units of ML. Other conventional parameters such as the surface roughness $\langle \Delta z^2 \rangle$ and the lattice distortion were also considered as usual (see, for example, Ref. [20]). The values of these parameters were obtained at the best fit of the theoretical curve to each of the experimental spectra.

The fitting was performed so as to minimize the following conventional R-factor,

$$R = \frac{1}{N}\sum_{i=1}^{N}\frac{|\log I_{\rm e} - \log I_{\rm c}|}{\log I_{\rm e}}, \qquad (3.3)$$

where N is the number of measurement points, $I_{\rm e}$ is the experimentally obtained scattering intensity, and $I_{\rm c}$ is the calculated intensity. In order to assess the influence of noise included in the measurements on the R-factor, a standard sample (InP substrate) was measured and its profile was fitted with calculation. As a result, $R = 0.0085$ was obtained at the best fit, which limits the accuracy of the present experiment. For ZnSe/GaAs heterostructures, a 1 ML (2.8 Å) change in the ZnSe thickness around 50 Å was calculated to alter the R-factor by about 0.025 (> 0.0085). Therefore, a 1 ML difference may be detected.

results and discussion

Figure 3.14 shows the measured (background subtracted) CTR spectra by solid circles. The CTR scattering is elongated along the $[00l]$ direction in the reciprocal space as shown in Fig. 3.11, and therefore, the index l is used at the horizontal axis in Fig. 3.14 [21]. The measurements were performed in the vicinity of the 004 diffraction spot ($l = 4$). Each spectrum was shifted by two orders of magnitude for clarity and the bottom one was plotted at the real intensity. Upper two spectra are from the samples grown with the initial exposure of As:GaAs to Se for 15 and 60 s, and lower three spectra are from the samples grown with the initial exposure of Ga:GaAs to Zn for 2, 30, and 60 s before the ZnSe growth. The Se-exposure duration of 60 s resulted in the three-dimensional growth and was neglected in the previous section, but here, its CTR spectrum is shown for a comparison. Clear difference between the Zn-initiated growth and the Se-initiated growth is observed in both the lower and the higher index sides of the spectra. However, the difference arisen from the duration is trivial as long as the precursor to which GaAs was exposed is the same. Therefore, variation in the atomic distributions due to the duration

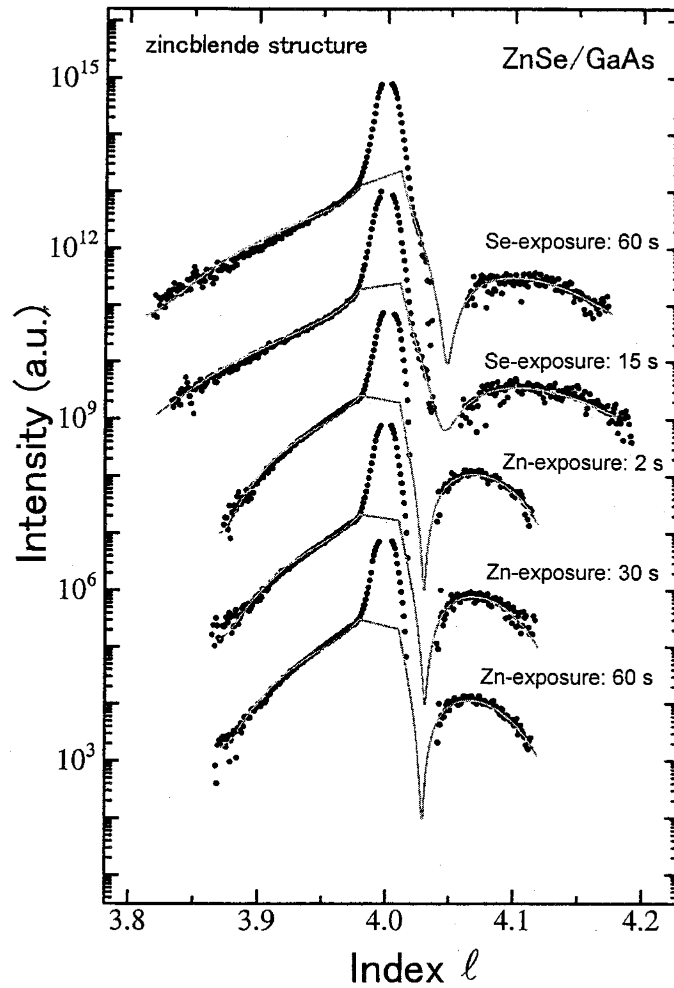

Figure 3.14: CTR spectra of ZnSe/GaAs heterostructures taken in the vicinity of the 004 ($l = 4$) Bragg spot. For the detail of the index l, see the text. Upper two curves are for the Se-initiated growth with the Se-exposure duration of 15 and 60 s, and lower three curves are for the Zn-initiated growth with the Zn-exposure duration of 2, 30, and 60 s. Clear differences are observed between the Se- and the Zn-initiated growth. Thin dotted lines are the best fit theoretical curves.

will not be detected clearly with the present experimental resolution. The lack of data around $l = 4.03$ in all spectra means that the diffraction intensities sharply drop toward zero.

In Fig. 3.14, the best fit curves to the spectra are also drawn with thin dotted lines. Data around the Bragg peak ($l = 4 \pm 0.01$) were not used for the fitting because the intensity may be too strong for the kinematical theory. For the Zn-initiated growth, the theoretical curves reasonably reproduce the experimental spectra. However, the best fit curves for the Se-initiated growth exhibit discrepancy from the experiments. In case of the Se-exposure duration of 15 s, the dip around $l = 4.03$ is not well expressed in the theoretical curve. For the sample with the Se-exposure duration of 60 s, reproducibility of the sharp drop around $l = 4.03$ is improved, but slight difference occurs at index l lower than 3.95. The observed discrepancy suggests the presence of some imperfections such as vacancies, anti-site defects, and interstitial atoms at the Se-initiated interfaces. As a first trial, Ga vacancies were introduced in the model structure.

Figure 3.15 shows the best fit curves to the upper two spectra in Fig. 3.14, *i.e.*, of the Se-initiated growth, calculated with the assumption of Ga vacancies. Compared with Fig. 3.14, much better fitting near the dip and in the lower index region was achieved. However, since the introduction of Ga vacancies into the model structure increases the

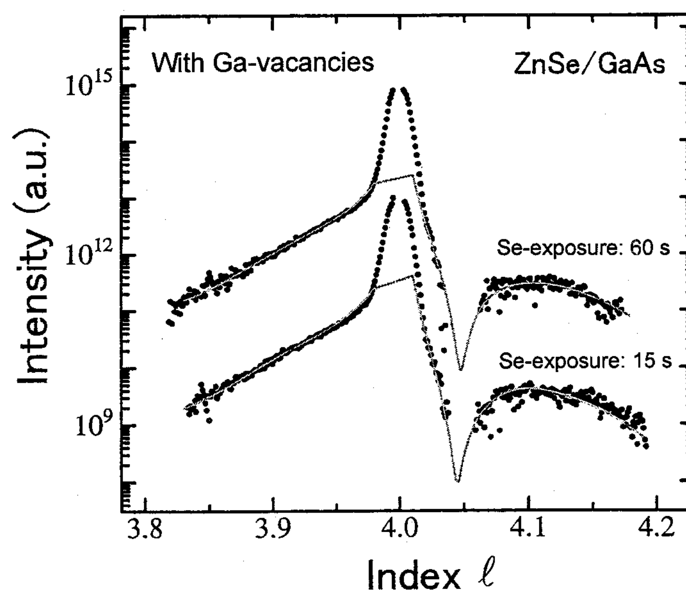

Figure 3.15: The CTR spectra of the samples grown with the Se-exposure and the theoretical spectra calculated under the assumption of Ga vacancies in the model structure.

number of the fitting parameters, it is quite difficult to conclude that Ga vacancies are the unique solution for explaining the observed CTR spectra. Indeed, the TEM observation shown in Fig. 2.11 suggested that there was no interface structure which included only Ga vacancies as a structural imperfection. Therefore, the conclusion we can make at this stage is that the Se-initiated growth induces some imperfections at the interface, though their structures remain controversial.

The analyses of the CTR spectra provide the distributions of Zn, Ga, Se, and As around the ZnSe/GaAs interfaces through the determination of the parameters in the model structures. The results are illustrated in Fig. 3.16, in which the result for the Se-initiated growth is tentative because its model structure is under progress as mentioned above. Since the distribution was changed by the duration negligibly, typical profiles for the Zn- and Se-initiated growths were shown. For the Zn-initiated growth, the compositions of Zn and

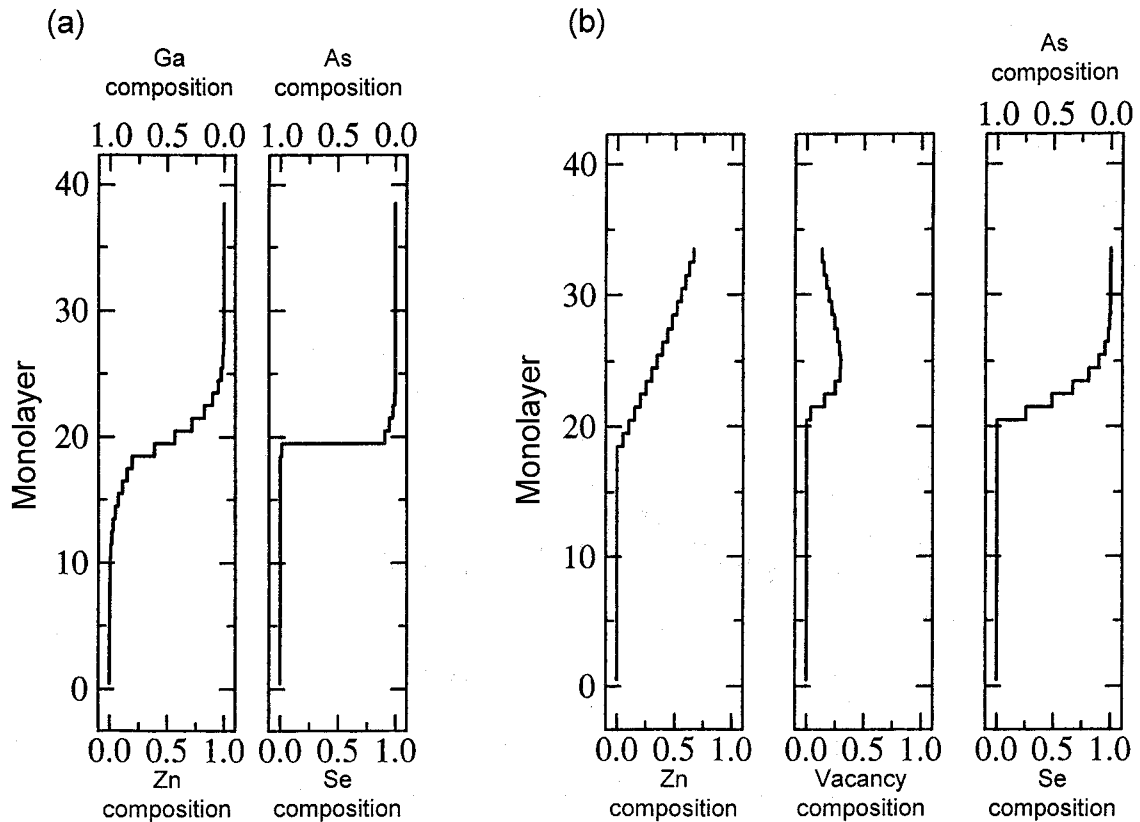

Figure 3.16: Distribution of the constituents around the interfaces formed with initial exposure of GaAs to (a) Zn for 30 s and (b) Se for 15 s.

Ga at the II/III interface are 0.5 and 0.5, which means that no vacancies were induced by this growth sequence. Furthermore, it is found that Zn and Ga distribute into several ML's of GaAs and ZnSe, respectively, while As and Se distributions change abruptly at the interface. This is quite interesting from the viewpoint of the formation of the electronic dipoles; since the atom distributions induce the donating Ga-Se bonds in the ZnSe layer and the accepting Zn-As bonds in the GaAs layer, dipoles pointing toward GaAs are supposed to be formed very near the interfaces as a result of electron transfer from Ga-Se to Zn-As. With those dipole moments, the electrostatic potential in GaAs is raised steeply within a distance of a few ML's, which was observed as the enlarged valence band offsets (at most, 1.1 eV) in the XPS measurements. For the Se-initiated growth, on the other hand, the atom distribution shown in Fig. 3.16(b) also implies the presence of spatially separated donor and acceptor bonds, and the formation of electronic dipoles pointing toward GaAs. These dipoles originate from the interfacial layer containing imperfections and, consequently, an increase of the imperfections by longer Se-exposure duration seems to result in a larger valence band offset. However, this band offset control based on the defective interface layer is out of scope of this study and has not been discussed in the previous section concerning XPS.

The depth profile of the XPS photoemission intensity ratio (Fig. 3.5) reflects the distributions of the constituent atoms. Therefore, from the model structures shown in Fig. 3.16, depth profiles of the normalized photoemission intensity ratios of $I_{\mathrm{Zn}}/I_{\mathrm{Se}}$ and $I_{\mathrm{Ga}}/I_{\mathrm{As}}$ can be deduced. Here, those ratios are calculated by the layer-attenuation model and are compared with the result of XPS. For this, the discussion was concentrated on the Zn-initiated growth, because the model structure for the Se-initiated growth involves uncertainty. By the layer-attenuation model, for example, the intensity ratio of Zn and Se photoemission signals, $i_{\mathrm{Zn}}/i_{\mathrm{Se}}$, is expressed as

$$\frac{i_{\mathrm{Zn}}}{i_{\mathrm{Se}}} = \frac{I^0_{\mathrm{Zn}}}{I^0_{\mathrm{Se}}} \cdot \frac{\sum\limits_{m} x_{\mathrm{hZn}} A^{2m+1}}{\sum\limits_{m} x_{\mathrm{hSe}} A^{2m}}, \tag{3.4}$$

where $A = \exp(-d/\Lambda)$ is the attenuation factor, d is the atomic layer spacing along the [001] direction, Λ is the electron escape depth, I^0_{Zn} and I^0_{Se} are the emission intensities from the Zn and Se monoatomic layers, respectively, and m is the number of molecular layers from the surface. Since the ZnSe layer is coherently grown on GaAs, d is 1.422 Å

in ZnSe and 1.413 Å in GaAs. The value of Λ, which was assumed to be common for all $3d$ photoelectrons, is 11 Å [22]. This assumption is reasonable because the electron escape depth is determined by the kinetic energy, which is almost the same for all photoelectrons in this study. Taking into account the experimentally determined region detectable by XPS of 45 Å, the summation was performed for 17 molecular layers from the surface. The normalized intensity ratio, I_{Zn}/I_{Se}, which was used in Fig. 3.5, was obtained by dividing i_{Zn}/i_{Se} with I^0_{Zn}/I^0_{Se}. Figure 3.17 shows the calculated depth profile of the photoemission intensity ratios (solid lines) as well as the experimental results of XPS (open circles). The model structure for the sample grown with the Zn-exposure for 30 s [Fig. 3.16(a)] was used as an example. I_{Zn}/I_{Se} is almost constant regardless of the ZnSe thickness, while I_{Ga}/I_{As} increases with increasing the ZnSe thickness. It is found that the depth profile revealed by XPS (open circles) is well reproduced by the layer-attenuation model based on the model structure derived from the x-ray CTR measurement. This result strongly suggests that the

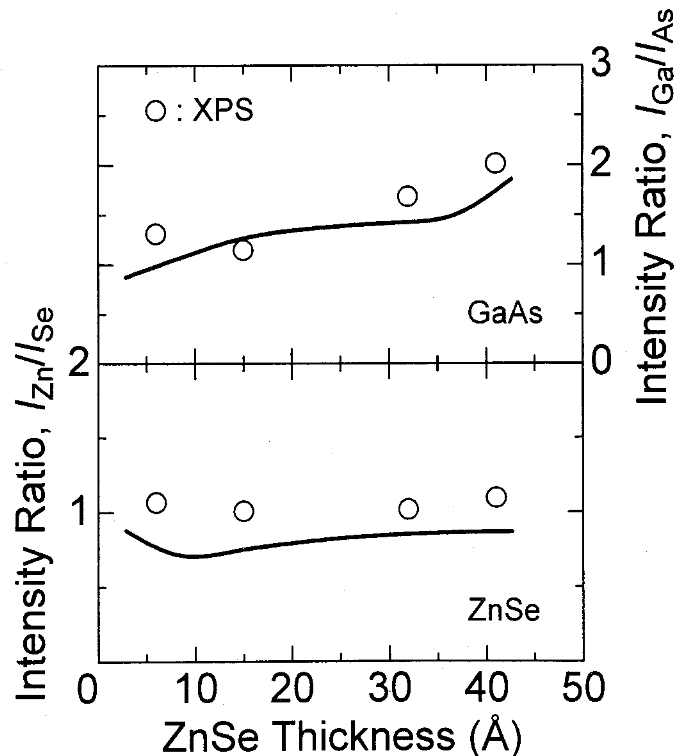

Figure 3.17: Depth profile of the photoelectron intensity ratios. The used sample was grown on Ga:GaAs with the Zn-exposure for 30 s. The solid lines were calculated by the layer-attenuation model, using the model structure determined by the x-ray CTR measurement. The open circles are the experimental results revealed by XPS.

variation of the interface composition, Ga/As, observed in XPS (*e.g.* Fig. 3.8) indicates the degree of the interdiffusion of Zn and Ga. When the interdiffusion is pronounced, which corresponds to large Ga/As, the electronic dipoles are strong and the valence band offset becomes large.

3.5 Electric Field at the Interface

In the above sections, the tunability of the band offsets was discussed in terms of the formation of the electronic dipoles. In this section, further evidence of their presence is given by quantitatively measuring the intensity of electric fields induced by the electronic dipoles.

experimental details

Modulation spectroscopy is an important technique for study and characterization of energy band structures of semiconductors. Among various modulation techniques, photoreflectance (PR) is of considerable interest because it yields spectra with sharp features at the critical-point energies, it is a contactless measurement technique, it requires no special mounting of samples, it can be performed in a variety of transparent ambients, and it is sensitive to surface and interface electric fields. It is well known that at high electric fields, Franz-Keldysh oscillation (FKO) appears in the PR spectra above the band gap energy. The period of the oscillation, which can be extracted by FFT of the spectra, is directly related to the electric field at the surface or interface [23-27]. Here, FFT-PR is applied to the ZnSe-GaAs heterovalent heterointerfaces to evaluate the intensity of the interface electric field.

The experimental setup for the PR measurements is shown in Fig. 3.18. A modulation light was provided by a 2-mW He-Ne laser. Its wavelength was 632.8 nm and, therefore, excited only GaAs region at the interface. The chopped laser light was irradiated on to the sample by a spot radius of approximately 1 mm. A 100-W tungsten lamp was dispersed by a 20-cm monochromator and used as a probe light. The reflected probe light from the sample was detected by a Si detector and the signal from the detector was fed to a lock-in amplifier. The measurements were carried out at room temperature.

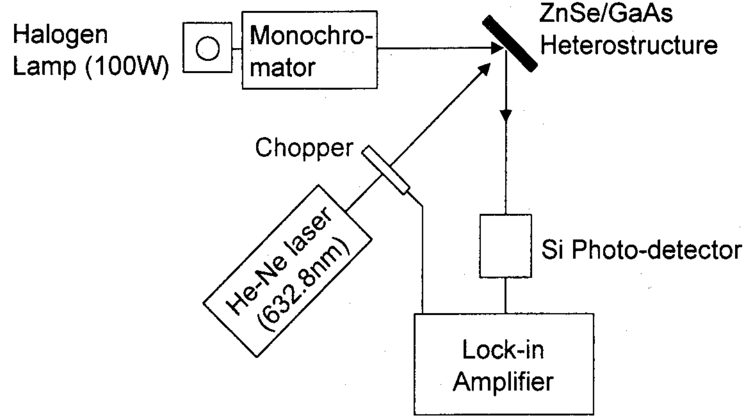

Figure 3.18: Schematic diagram of the PR system.

results and discussion

Figure 3.19 shows variation of the PR spectra due to the Zn-exposure duration and the Se-exposure duration, in which dR and R denote an ac and a dc component of the photoreflectance, respectively. Owing to the energy of the modulation light of the He-Ne laser, the PR spectra inform about the characteristic features only in the GaAs region. The samples are the same as those used in the x-ray CTR measurement; prior to the ZnSe growth, Ga:GaAs was exposed to a Zn flux for 2, 15, and 60 s, while As:GaAs was exposed to a Se flux for 15 and 60 s. The PR spectra for the Zn-exposed samples are shown in Fig. 3.19(a) and those for the Se-exposed samples in Fig. 3.19(b). All spectra exhibit a long period of FKO above the band gap energy of GaAs [$E_{\mathrm{g}}^{(\mathrm{GaAs})}$]. The oscillatory behavior in the energy (E) region higher than the band gap energy (E_{g}) is correlated with electric field (F) by an electrooptic function, whose asymptotic form [28] can be written as

$$\mathrm{d}R/R \sim \cos\left[\frac{4}{3}\left(\frac{E-E_{\mathrm{g}}}{\hbar\Theta}\right)^{3/2} + \frac{\pi}{2}(n_{\mathrm{d}}-1)\right], \tag{3.5}$$

where $(\hbar\Theta)^3 = e^2\hbar^2F^2/2\mu_{\parallel}$, n_{d} is the dimensionality of the critical point, and $\mu_{\parallel}$ is the reduced effective mass. Therefore, the observed FKO indicates the existence of high electric fields at the heterointerfaces between ZnSe and GaAs.

To extract the FKO periods and then the electric fields in the samples, which are mutually related via Eq. (3.5), we transformed the horizontal variable in Fig. 3.19, E, to $\varepsilon = (E - E_{\mathrm{g}})^{3/2}$ and performed the Fourier transform against the PR spectra at $E > E_{\mathrm{g}}$

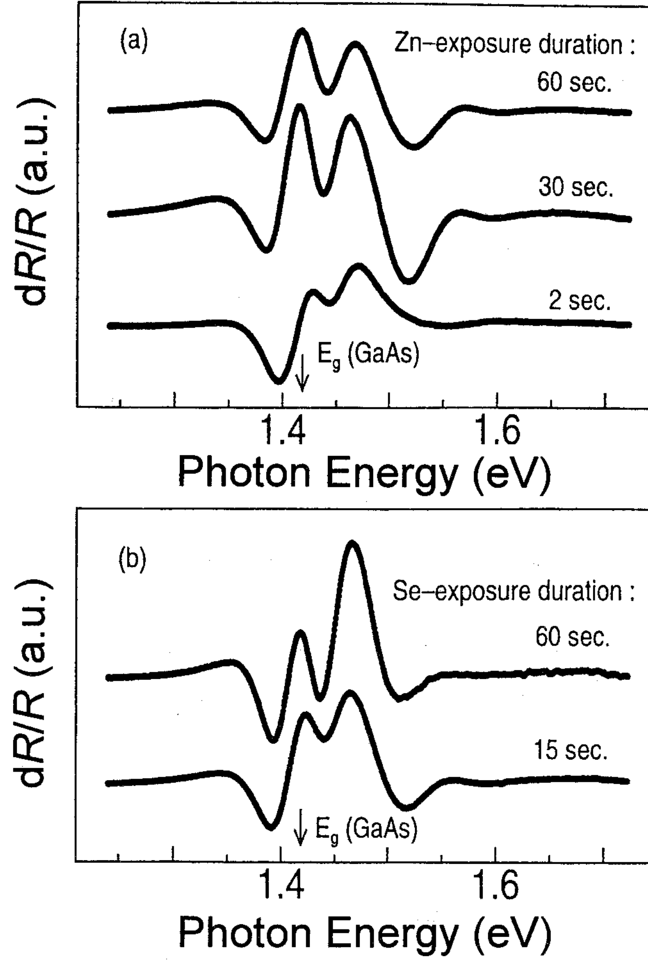

Figure 3.19: Room temperature PR spectra measured in the GaAs regions. Variation due to (a) Zn-exposure duration and (b) Se-exposure duration is shown.

as [29]

$$G(\tau) = \int (\mathrm{d}R/R) \exp(-i2\pi\varepsilon\tau) \mathrm{d}\varepsilon. \tag{3.6}$$

The fast Fourier transform method was applied for the calculation. The main peak position (τ_0) evaluated from the Fourier transform is related to the electric field (F) by

$$\tau_0 = (2/3\pi)(2\mu_{\parallel})^{1/2}(1/e\hbar F), \tag{3.7}$$

as is deduced from Eq. (3.5).

Figure 3.20 shows $G(\tau)$ transformed from the PR spectra (Fig. 3.19) as a function of $\tau^{2/3}$, whose dimension is the inverse of energy. As can be seen, the transformed results clearly exhibit a single peak due to FKO. The electric fields calculated from the peak

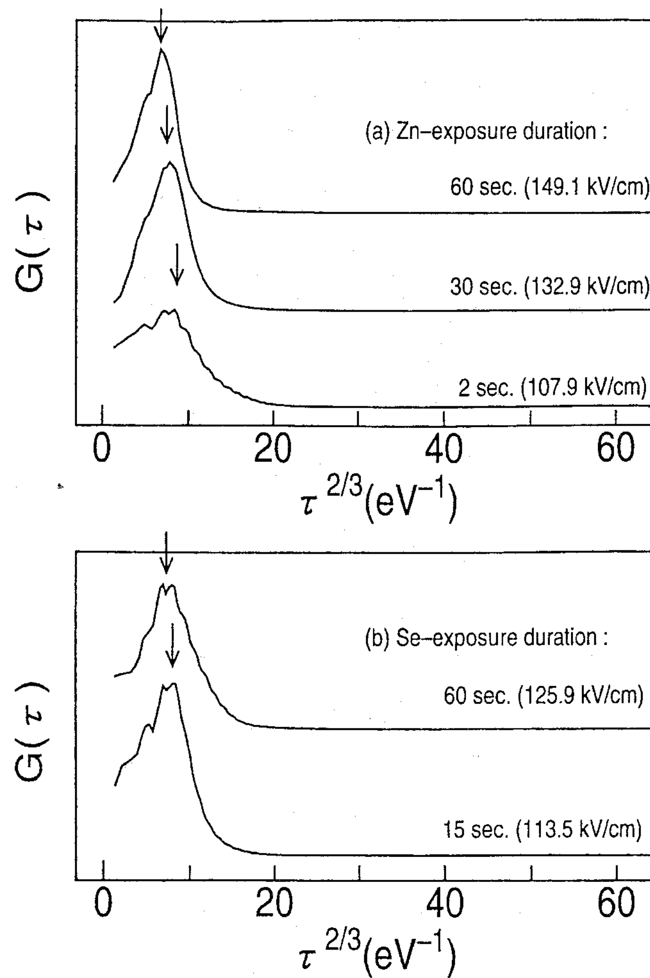

Figure 3.20: FFT results obtained from the PR spectra.

positions are also indicated in Fig. 3.20. Those are intense in the range of 100 – 150 kV/cm. It was frequently reported that when the strength of the electric field was not uniform, the electric fields estimated by FKO were lower than the maximum electric field [23, 30], implying that the electric field derived from the FKO period is the average value [30]. Therefore, the maximum electric fields at the ZnSe/GaAs interfaces are considered to be more intense than the estimated values.

It is quite interesting to compare the electric field derived from FFT-PR with the valence band offset derived from XPS. The comparison as a function of the Zn- or Se-exposure duration is shown in Fig. 3.21. It is clear from the figure that the electric field and the band offset possess a strong correlation. However, if the valence band offset is controlled only by the interface atomic configuration, it should be decreased monotonously from the

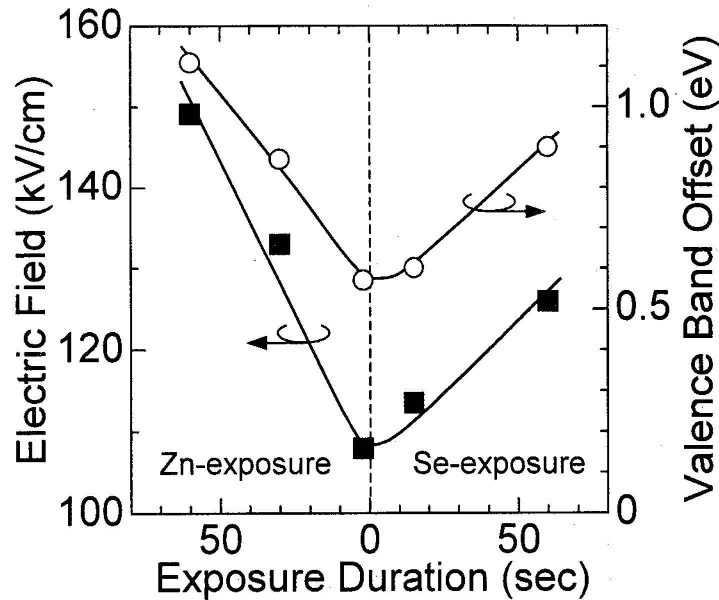

Figure 3.21: Comparison of dependence of the electric field and the valence band offset on the Zn- or Se-exposure duration.

left-hand side to the right-hand side of the figure, as deduced from Fig. 1.2. Thus, we need to discuss the cause for the v-shape characteristic shown in Fig. 3.21. For the Zn-exposure, the x-ray CTR measurements revealed that the interface was free from defects such as vacancies and suggested the formation of the electronic dipoles. Furthermore, the behavior of the valence band offset against the Zn-exposure duration agrees with the expectation. Therefore, the observed variations of both the electric field and the valence band offset can be attributed to the control of the interface atomic configuration, which is the basic idea of this study. As for the Se-exposure, the valence band offset increases with the Se-exposure duration, suggesting that the valence band offset is not determined only by the interface atomic configuration and that other factors should be considered. Here, note that the presence of imperfections was pointed out by the TEM observation [Fig. 2.11(b)] and the x-ray CTR measurement (Sec. 3.4), and that, as mentioned previously, the surface of ZnSe grown with the Se-exposure duration of 60 s was three-dimensional. These experimental results suggest that a transition layer including imperfections is formed between ZnSe and GaAs and changes the growth behavior. Furthermore, the x-ray CTR measurement implied that the defective interface layer increased the valence band offset. Therefore, we consider at present that the formation of the interface layer due to the Se-exposure causes the increase in the electric field and the valence band offset.

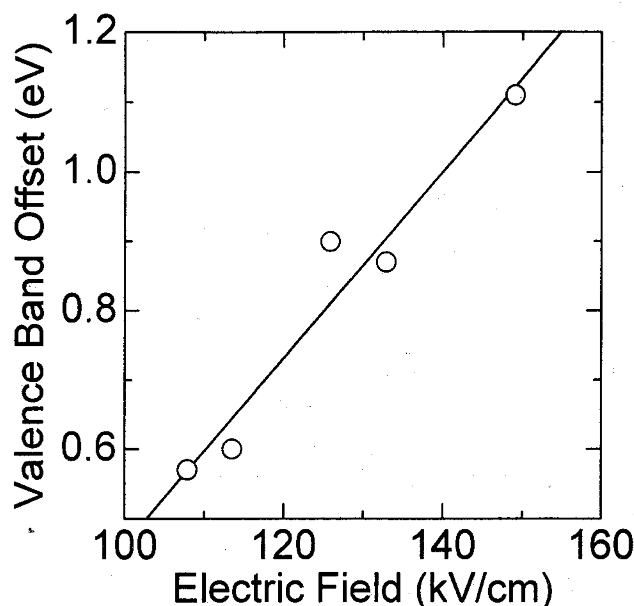

Figure 3.22: Correlation between the valence band offset and the electric field.

In order to see the correlation between the valence band offset and the electric field more explicitly, the former was plotted as a function of the latter in Fig. 3.22. In the figure, all results of the Zn- and Se-initiated growth are shown. Almost linear dependence of the valence band offset on the electric field strongly supports the assertion that the electric field caused by the electronic dipoles determines the valence band offset. Also, this figure indicates that how to form dipoles is not essential; concerning this study, the control of the interface atomic configuration (Zn-initiated growth) and the introduction of the defective interface layer (Se-initiated growth) brought the same results.

We wish to emphasize that, for the Zn-exposure, the XPS, x-ray CTR, and FFT-PR measurements have given the consistent results proving the tunability of the band offset via the control of the interface atomic configuration. The results of those measurements were schematically summarized in Fig. 3.23 using the band diagram. As a result of the Zn-exposure, the donating Ga-Se bonds and the accepting Zn-As bonds are formed in ZnSe and GaAs, respectively (x-ray CTR). Electrons being originally at the Ga-Se bonds in ZnSe transfer to the Zn-As bonds in GaAs and form electronic dipoles very near the interfaces, which were measured as the intense electric field in FFT-PR. Since the interdiffusion of Zn and Ga atoms revealed by the x-ray CTR measurement is within a few ML's, the band-bending due to the dipoles is quite abrupt and was apparently measured by XPS as a

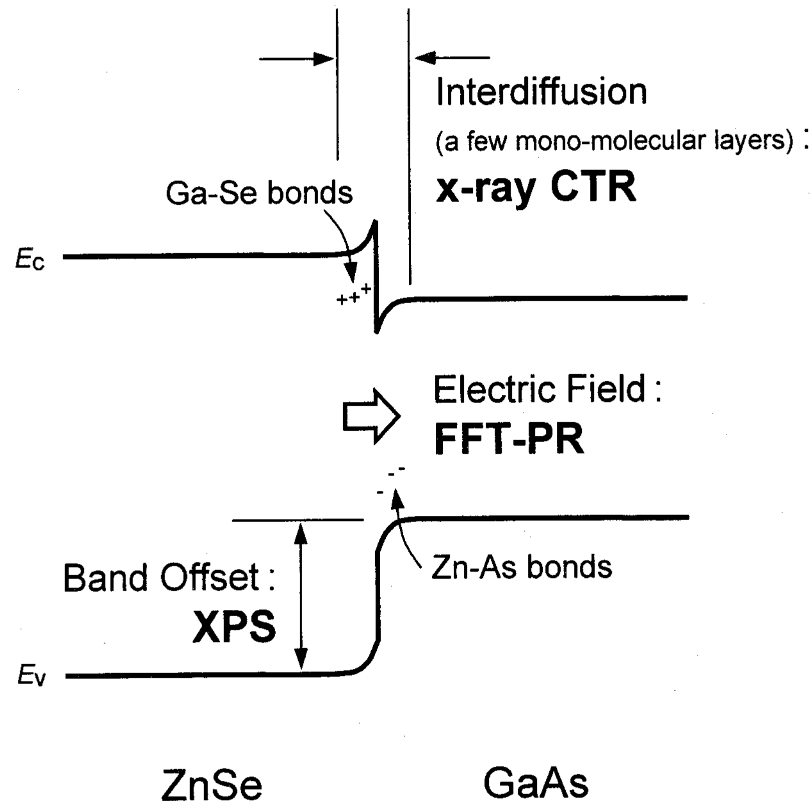

Figure 3.23: Schematic summary of the XPS, x-ray CTR, and FFT-PR measurements.

change of the valence band offset.

3.6 Summary

Tunability of the band offsets in ZnSe/GaAs(001) heterovalent heterostructures was successfully achieved by controlling the local interface composition by means of Zn- or Se-exposure, or thermal etching of the GaAs surfaces followed by ZnSe growth. In order to elucidate the mechanism of the tunability, the interfaces were investigated structurally by x-ray CTR measurements and optically by FFT-PR measurements. As a result, it was found that Zn and Ga atoms interdiffused to a few ML's to form electronic dipoles, and that those dipoles bent the energy band very abruptly at the interface. This sharp band-bending, that is, strong electric field, due to the dipoles was closely related to the band offset evaluated by XPS, indicating that the interface atomic configuration, which induces electric fields, plays a crucial role in determining the interface properties.

References

[1] L. A. Hemstreet, C. Y. Fong, and J. S. Nelson, J. Vac. Sci. Technol. B**11**, 1693 (1993).

[2] R. Nicolini, L. Vanzetti, G. Mula, G. Bratina, L. Sorba, A. Franciosi, M. Peressi, S. Baroni, R. Resta, A. Baldereschi, J. E. Angelo, and W. W. Gerrich, Phys. Rev. Lett. **72**, 294 (1994).

[3] A. Kley and J. Neugebauer, Phys. Rev. B **50**, 8616 (1994).

[4] R. G. Dandrea, S. Froyen, and A. Zunger, Phys. Rev. B **42**, 3213 (1990).

[5] K. Kunc and R. M. Martin, Phys. Rev. B **24**, 3445 (1981).

[6] G. Bratina, L. Vanzetti, A. Bonanni, L. Sorba, J. J. Paggel, A. Franciosi, T. Peluso, and L. Tapfer, J. Crystal Growth **159**, 703 (1996).

[7] R. W. Grant, J. R. Waldrop, S. P. Kowalczyk, and E. A. Kraut, J. Vac. Sci. Technol. B **3**, 1295 (1985).

[8] J. R. Waldrop, R. W. Grant, S. P. Kowalczyk, and E. A. Kraut, J. Vac. Sci. Technol. A **3**, 835 (1985).

[9] Scanning tunneling microscopy (STM) may also be available for the estimation of band offsets because STM can estimate density of states (DOS) by measuring the dependence of tunneling current on bias voltage. The difference of the onset of DOS due to materials is equal to the band offset, which will be detected by scanning across the interface, for example, appeared on a cleaved surface. However, DOS estimated by STM is surface "local" DOS, and we must take care of the modification of DOS due to dangling bonds and dimers at the surface.

[10] E. A. Kraut, R. W. Grant, J. R. Waldrop, and S. P. Kowalczyk, Phys. Rev. Lett. **44**, 1620 (1980).

[11] S. P. Kowalczyk, E. A. Kraut, J. R. Waldrop, and R. W. Grant, J. Vac. Sci. Technol. **21**, 482 (1982).

[12] G. Bratina, R. Nicolini, L. Sorba, L. Vanzetti, G. Mula, X. Yu, and A. Franciosi, J. Crystal Growth **127**, 387 (1993).

[13] H. Mitsuhashi, I. Mitsuhashi, M. Mizuta, and H. Kukimoto, Jpn. J. Appl. Phys. **24**, L578 (1985).

[14] C. G. Van de Walle and R. M. Martin, Phys. Rev. B **34**, 5621 (1986).

[15] K. Shahzad, D. J. Olego, and C. G. Van de Walle, Phys. Rev. B **38**, 1417 (1988).

[16] B. Chelluri, T. Y. Chang, A. Ourmazd, A. H. Dayem, J. L. Zyskind, and A. Srivastava, Appl. Phys. Lett. **49**, 1665 (1986).

[17] I. K. Robinson, Phys. Rev. B **33**, 3830 (1986).

[18] Y. Kashihara, S. Kimura, and J. Harada, Surf. Sci. **214**, 477 (1989).

[19] Y. Takeda, Y. Sakuraba, Y. Fujibayashi, M. Tabuchi, T. Kumamoto, I. Takahashi, J. Harada, and H. Kamei, Appl. Phys. Lett. **66**, 332 (1995).

[20] M. Tabuchi, N. Yamada, K. Fujibayashi, Y. Takeda, and H. Kamei, J. Electon. Mater. **25**, 671 (1996).

[21] In the particular case of symmetric diffraction such as 002 and 004, the relation between the index l and diffraction angle θ can be expressed as $2(a/l)\sin\theta = \lambda$, where a is the lattice parameter and λ is the wavelength of x-ray.

[22] C. M. Kwei and L. W. Chen, Surf. Interface Anal. **11**, 60 (1988).

[23] N. Bottka, D. K. Gaskill, R. S. Sillmon, R. Henry, and R. Glosser, J. Electon. Mater. **17**, 161 (1988).

[24] C. Van Hoof, K. Deneffe, J. De Boeck, J. D. Arent, and G. Borghs, Appl. Phys. Lett. **54**, 608 (1989).

[25] H. Shen, M. Dutta, L. Fotiadis, P. G. Newman, R. P. Moerkirk, W. H. Chang, and R. N. Sacks, Appl. Phys. Lett. **57**, 2118 (1990).

[26] C. R. La, C. L. Chang, C. H. Lion, J. R. Anderson, D. R. Stone, and R. A. Wilson, Appl. Surf. Sci. **92**, 404 (1996).

[27] D. P. Wang and C. T. Chen, Appl. Phys. Lett. **67**, 2069 (1995).

[28] D. E. Aspnes and A. A. Studna, Phys. Rev. B **7**, 4605 (1973).

[29] W. H. Press, S. A. Teukolsky, W. T. Vetterling, and B. P. Flannery, in *Numerical Recipes in Cambridge University*, Cambridge, 1994, p.496.

[30] J. Nukeaw, Y. Fujiwara, and Y. Takeda, Jpn. J. Appl. Phys. **36**, 7019 (1997).

Chapter 4

MOVPE Growth of GaAs on ZnSe

4.1 Introduction

In chapter 2, the nucleation processes during metalorganic vapor phase epitaxy (MOVPE) of ZnSe/GaAs were discussed, and the two-dimensional (2D) growth in the atomic level was achieved. This, in turn, implies that the inverse growth of GaAs on ZnSe (GaAs/ZnSe) is considerably more difficult than the growth of ZnSe/GaAs (see chapter 1 for the details). In the case of molecular beam epitaxy (MBE), actually, owing to the low sticking coefficient of As molecules to ZnSe, GaAs grown on ZnSe is generally three-dimensional (3D). To obtain 2D and high quality GaAs/ZnSe, several attempts have been made [1-4]. Kobayashi *et al.* employed the combination of solid-phase epitaxy (SPE) and migration-enhanced epitaxy (MEE) [1,2]. The GaAs growth was initiated with As_4 adsorption on ZnSe followed by deposition of 2 atomic layers of Ga at room temperature. Successively, deposited Ga and As were crystallized to GaAs by SPE, on which GaAs was grown by MEE at a relatively low temperature of 250°C. Farrell *et al.* examined the correlation between interface structures and the growth behavior of GaAs MBE onto ZnSe [3]. They pointed out that a ZnSe(100)$c(2 \times 2)$-Zn surface, which is terminated with 1/2 atomic layer of Zn, is optimized by a sequence of steps involving a predeposition of excess Se and a low-temperature deposition of 1/2 atomic layer of Ga prior to the GaAs epitaxy. Gas source MBE (GSMBE) using thermally pre-cracked AsH_3 also required a complicated procedure [4]. At the interface, Ga source metal was sequenced with a constant As_2 flux at a high V/III ratio of 12 and a low substrate temperature of 250°C. Then, after 6 monolayers (ML, 1 ML = 2.8 Å) deposition, the V/III ratio and the substrate temperature were varied to 1 and 350°C, respectively, which are the typical conditions for the continuous growth of

GaAs.

On the other hand, MOVPE growth of GaAs/ZnSe has not been reported yet, although the growth ambient considerably different from that of MBE may provide different growth behavior. Therefore, in this chapter, the MOVPE growth of GaAs on ZnSe is investigated in detail in an attempt to establish the growth procedure. For this purpose, first, the effects of the source precursors for GaAs on ZnSe are studied. Then, the effects of growth conditions, in particular the growth temperature (T_g) and the V/III ratio, on the growth behavior in GaAs MOVPE on ZnSe are studied. It is found that either the 2D or 3D growth mode occurs depending on the growth conditions and the mechanism behind it is discussed. We demonstrate that 2D GaAs can be grown on ZnSe at a constant growth temperature without complicated procedures, unlike MBE.

4.2 Flow Sequence of GaAs Source Precursors at the Interface

To optimize the flow sequence of triethylgallium (TEGa) and tertiarybutylarsine (TBAs) at the interfaces, TEGa or TBAs is separately supplied to the ZnSe surface at 450 – 550°C, and their behavior on it is investigated. For this experiment, unexpected modification of the ZnSe surface morphology while the substrate temperature is descending without a flow of the precursors must be avoided. Therefore, the thermal stability of ZnSe was examined by annealing at 550°C for 30 min in an H_2 or N_2 ambient. Figure 4.1 shows the thermally etched thickness of ZnSe as a function of its growth temperature. The etched thickness was estimated by measuring the ZnSe film thickness before and after etching by ellipsometry. It is found that ZnSe is etched with the help of H_2 and that the thermal stability is higher for ZnSe grown at a higher temperature. For example, the etching rates for ZnSe grown at 450 and 550°C were estimated to be 9.0 and 4.4 Å/min in H_2, respectively. Taking this result into account, the underlying ZnSe in this section was grown at 550°C with the thickness of 700 – 800 Å. Referring to chapter 2, the growth temperature of 550°C for ZnSe seems to be too high in terms of surface flatness, although, here, the thermal stability was given a first priority.

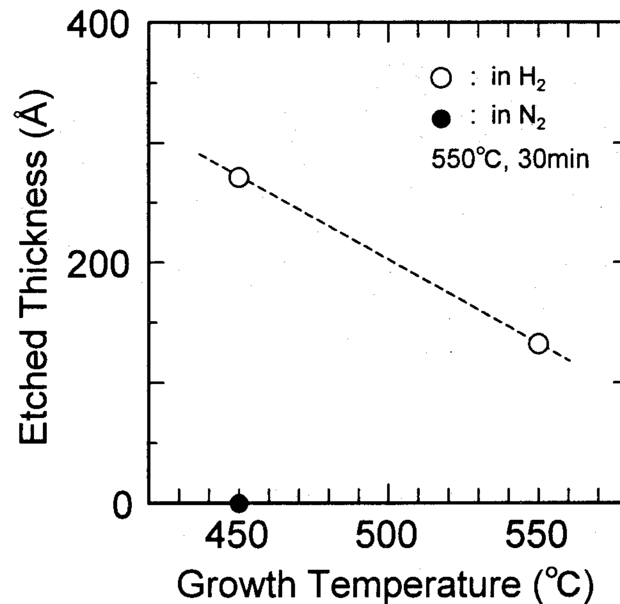

Figure 4.1: Etched thickness of ZnSe by annealing at 550°C for 30 min in an H_2 or N_2 ambient.

4.2.1 Ga precursor

First, ZnSe was exposed to TEGa at 550°C for 4 min. Figure 4.2 compares surface morphologies of ZnSe before and after the TEGa-exposure. A Nomarski microscope was used for the observation. As-grown ZnSe possessed a mirror like surface, while the surface became three-dimensional after the TEGa-exposure. Since TEGa decomposes completely into Ga metal above 350°C [5], it is reasonable to consider that metal Ga deposited on ZnSe. The presence of Ga on ZnSe was confirmed by surface analysis by means of Auger electron spectroscopy. When the temperature at which ZnSe is exposed to TEGa was lowered to 450°C, the surface was improved but still three-dimensional. As deduced from the decomposition temperature of TEGa (350°C), the deposition of Ga could result even by the TEGa-exposure at 450°C. From those results, it is considered that the 3D surface is indicative of active migration of metal Ga on the ZnSe surfaces, and that the improvement of surface roughness by a lower temperature is due to suppression of the migration.

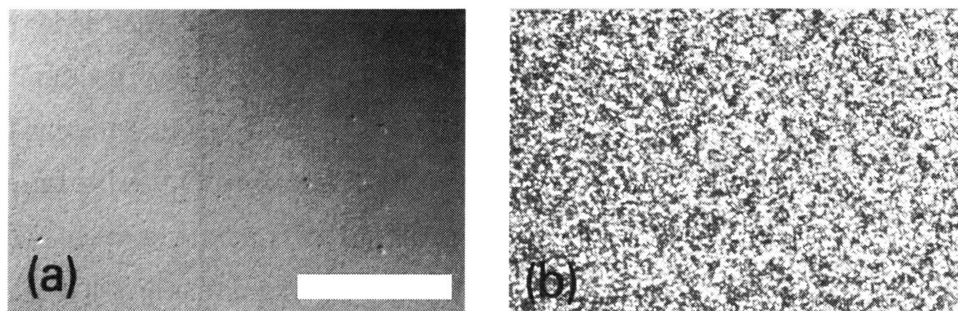

Figure 4.2: Surface morphologies of ZnSe; (a) as-grown and (b) after the TEGa-exposure at 550°C for 4 min. Marker represents 50 μm.

4.2.2 As precursor

experimental results

In a TBAs ambient, on the other hand, it was found that ZnSe was drastically etched compared with "pure" thermal etching mentioned above (Fig. 4.1). The etched thickness of ZnSe after annealing at 550°C under a flow rate of TBAs ([TBAs]) of 20 μmol/min is plotted in Fig. 4.3. The etched thickness increases as the annealing duration, from which the etching rate was estimated to be about 150 Å/min. On the other hand, when the annealing temperature (T_a) was decreased to 300°C, ZnSe was hardly etched. Some products generated by a reaction between ZnSe and TBAs seem to govern the etching properties.

The relation between the etching rate and the TBAs partial pressure (P_{TBAs}) was estimated at a constant annealing temperature of 550°C. The result is indicated in Fig. 4.4. From the slope of the straight line, the etching rate turned out to be proportional to the 0.56^{th} power of P_{TBAs}, which means that the stoichiometric coefficient of TBAs in the reaction with ZnSe is 0.56. Using this quantity, the reaction mechanism will be discussed later.

Figure 4.5 shows the Arrhenius plot of the etching rate, where [TBAs] was 20 μmol/min. Since TBAs decomposes completely in the temperature region investigated here [6, 7], the Arrhenius plot does not reflect the pyrolysis of TBAs but does reactions related to the etching of ZnSe. This figure exhibits that the etching of ZnSe by TBAs is a

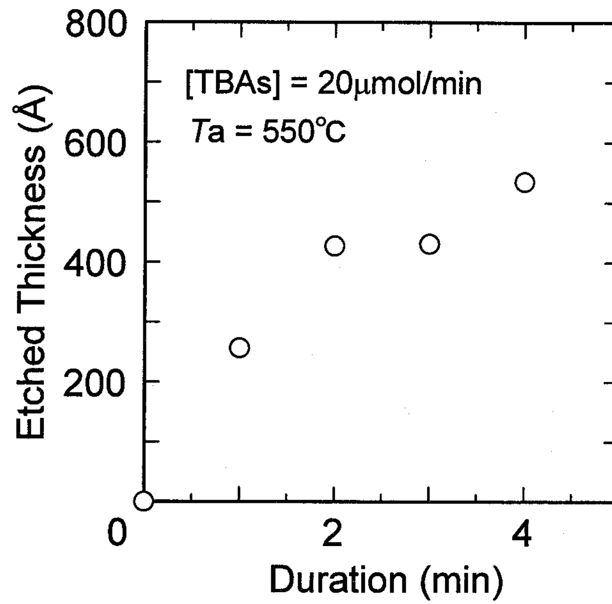

Figure 4.3: Etched thickness as a function of the annealing duration at 550°C. [TBAs] = 20 μmol/min. The annealing temperature is denoted by T_a.

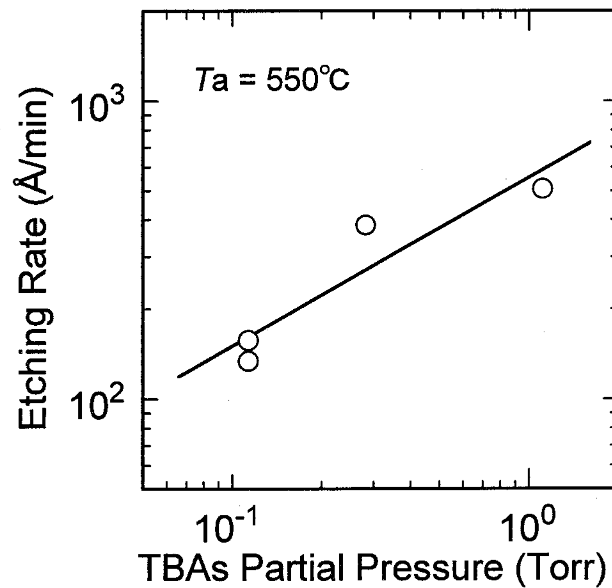

Figure 4.4: Variation of the etching rate at 550°C due to the TBAs partial pressure.

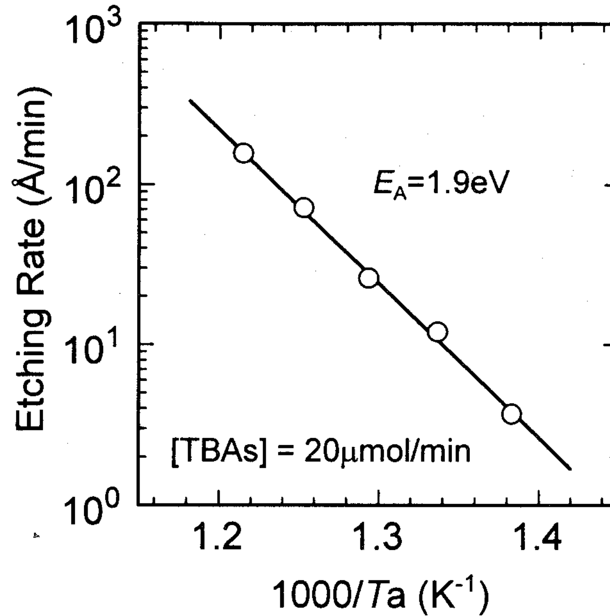

Figure 4.5: Arrhenius plot of the etching rate under [TBAs] = 20 μmol/min. The activation energy (E_A) was calculated to be 1.9 eV from the slope.

first order reaction. The activation energy (E_A) given by the slope was 1.9 eV.

Typical surface morphology of the ZnSe layer etched by TBAs is indicated in Fig. 4.6. The annealing temperature, the flow rate of TBAs, and the etched thickness for the sample are 550°C, 20 μmol/min, and 470 Å, respectively. The surface became rough after etching compared with the as-grown ZnSe surface shown in Fig. 4.2(a). Regardless of the annealing conditions, the surfaces tend to be rough after etching.

discussion

The surface morphology shown in Fig. 4.6 indicates that the etching mechanism in not congruent desorption of Zn and Se. Therefore, desorption of Zn and Se must be considered separately.

Concerning the desorption of Zn, one of the most plausible reactions is formation and evaporation of Zn_3As_2. Etching of GaAs using dimethylzinc as an etchant has been reported and generation of Zn_3As_2 on the GaAs surface has been proposed as the etching mechanism [8]. Similarly, when TBAs is passed over ZnSe, Zn_3As_2 may be synthesized through a surface reaction between TBAs and the surface Zn atoms. Since Zn_3As_2 is a volatile compound rapidly desorbing above 360°C [9], the formation of Zn_3As_2 at 550°C

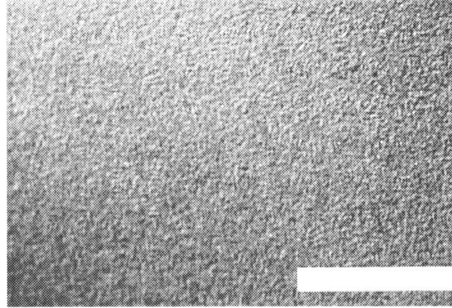

Figure 4.6: Surface morphology of ZnSe after annealing in a TBAs ambient. T_a, [TBAs], and the etched thickness are 550°C, 20 μmol/min and 470 Å, respectively. Marker represents 50 μm.

is immediately followed by evaporation, resulting in the Se-terminated ZnSe surface. This reaction is expressed as

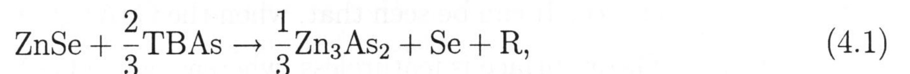

$$\mathrm{ZnSe} + \frac{2}{3}\mathrm{TBAs} \rightarrow \frac{1}{3}\mathrm{Zn_3As_2} + \mathrm{Se} + \mathrm{R}, \tag{4.1}$$

where R represents hydrocarbon and hydrogen molecules, though has not been identified yet. The stoichiometric coefficient of TBAs in the reaction (4.1) is 2/3 and this value is very close to the slope of 0.56 in Fig. 4.4. This implies that the stoichiometric coefficient of TBAs in a reaction with surface Se is also about 2/3. This is because Fig. 4.4 illustrates the macroscopic etching properties concerning TBAs reacting with both Zn and Se, and consequently, the slope in Fig. 4.4 must be average of the stoichiometric coefficient of TBAs in each reaction.

For discussing the Se desorption, the results of the next chapter are necessary. Brief summaries are as follows: (1) the desorption rate of Se from ZnSe in an H_2 ambient is faster than in a TBAs ambient, and (2) the dependence of the etching rate of ZnSe on the annealing temperature shown in Fig. 4.5 is caused by the Se desorption, not by the Zn desorption. The result (1) rules out H_2Se gas as a reaction product responsible for the etching with TBAs; since, in addition to the carrier gas, H_2 which is provided through the TBAs pyrolysis [7] may also contribute to the formation of H_2Se gas, the presence of TBAs could increase the etching rate. Therefore, at present, we consider that a reaction between Se and As forms an As_xSe_{1-x} compound [10, 11] and that its formation and evaporation

properties determine the ZnSe etching properties such as the activation energy of 1.9 eV observed in Fig. 4.5.

4.2.3 Surface morphology of GaAs on ZnSe

The above experimental results suggest that the ZnSe surface before the GaAs growth should not be exposed to TEGa or TBAs alone for a long time. Within this limit, in this section, GaAs is grown on ZnSe by varying the flow sequence at the interface and their structural properties are compared.

The growth temperature of GaAs was 500°C because growth temperatures above 550°C make the surface of GaAs three-dimensional, as will be presented later, and make the comparison difficult. Figure 4.7 shows the surface morphologies of GaAs grown on ZnSe with the initial exposure of ZnSe to (a) TEGa and (b) TBAs. The remainder of the source precursors, that is, TBAs for (a) and TEGa for (b), was supplied just 2 s later. The thicknesses of GaAs and ZnSe are 175 Å and 225 Å, respectively, and therefore, the layers maintain full coherence. It can be seen that, when the GaAs growth was started with TBAs [Fig. 4.7(b)], the GaAs surface is featureless, whereas, when GaAs was grown in the reverse sequence [Fig. 4.7(a)] , fine structures appear on the surface. Their crystalline qualities were assessed by the double crystal x-ray diffraction (XRD), using Cu $K\alpha_1$ (1.5405 Å) radiation as an x-ray source. The measurements were performed with the locking mode in the vicinity of the GaAs 004 diffraction. The results are shown in Fig. 4.8 along with the theoretical

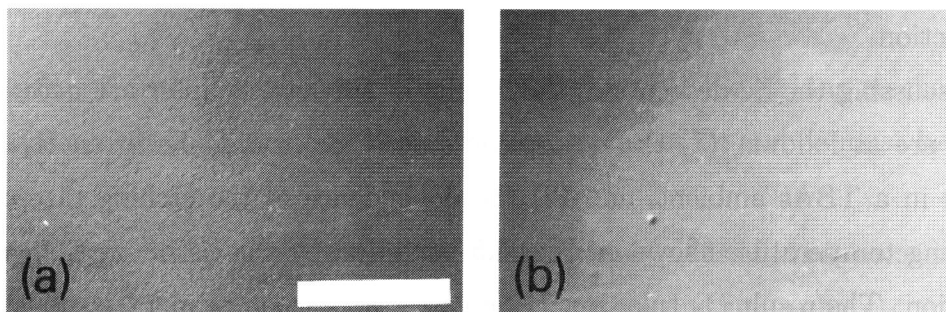

Figure 4.7: Surface morphologies of GaAs grown on ZnSe. The GaAs growth was initiated by (a) TEGa and (b) TBAs and the rest of the precursors was supplied 2 s later. Marker represents 50 μm.

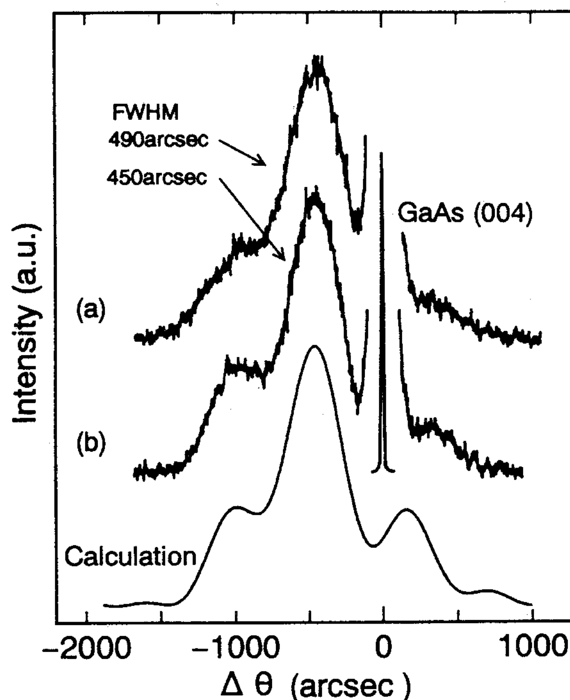

Figure 4.8: Double crystal XRD patterns (locking curves) of the same samples used in the previous figure: (a) TEGa and (b) TBAs initiated growth.

calculation based on the kinematical theory. The profile (b), where TBAs initiated the GaAs growth, agrees quite well with the theoretical simulation. On the other hand, it is found in the profile (a), where TEGa initiated the GaAs growth, that interference of x-ray diffracted by the GaAs and ZnSe layers becomes weak as seen around $\Delta\theta = -1000$ and 300 arcsec, and that the full width at half maximum (FWHM) of the main peak broadens by 40 arcsec. The GaAs surface tended to be rough by the TEGa initiation, as shown in Fig. 4.7(a). Therefore, the observed degradation of the XRD profile is probably due to the interface roughness and/or undulation of the GaAs surface caused by the Ga migration on the ZnSe surface rather than due to the poor crystalline quality. The broadening of FWHM by 40 arcsec is equivalent to a thickness fluctuation of 35 Å.

On the basis of the experimental results in this section, the GaAs growth on ZnSe, hereafter, is initiated with TBAs followed by TEGa to achieve good structural properties.

4.3 Growth Mechanism of GaAs on ZnSe

For fabricating structurally well-defined ZnSe-GaAs multilayered heterostructures, it is crucially important to understand the growth mechanism of GaAs on ZnSe comprehensively. In this section, the growth behavior of GaAs on ZnSe is discussed.

4.3.1 Growth mode

GaAs was grown on ZnSe under various growth conditions in order to reveal the growth modes and discuss its origin. The designed structure is illustrated in Fig. 4.9, wherein we can investigate the growth behavior of GaAs heteroepitaxy on ZnSe, ZnSe heteroepitaxy on GaAs, and GaAs homoepitaxy through observation of cross-sectional views of layers A, B, and C, respectively. All samples were confirmed by XRD to grow coherently against the GaAs substrate.

The effect of the growth temperatures for both ZnSe and GaAs on the surface morphology was investigated using a Nomarski microscope. The results are shown in Fig. 4.10. It is clearly seen that, regardless of the growth temperature of ZnSe, GaAs cannot be grown at 550°C without degrading surface morphology. On the other hand, the GaAs layers grown below 500°C on the ZnSe layers grown at 450 or 500°C exhibit mirror like surfaces. In the

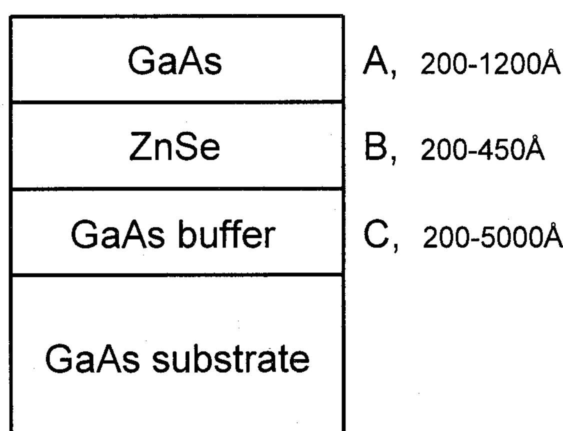

Figure 4.9: Schematic diagram of the designed GaAs-on-ZnSe heterostructure. The expected dimensions are 200 – 1200 Å for GaAs, 200 – 450 Å for ZnSe, and 200 – 5000 Å for the GaAs buffer layer.

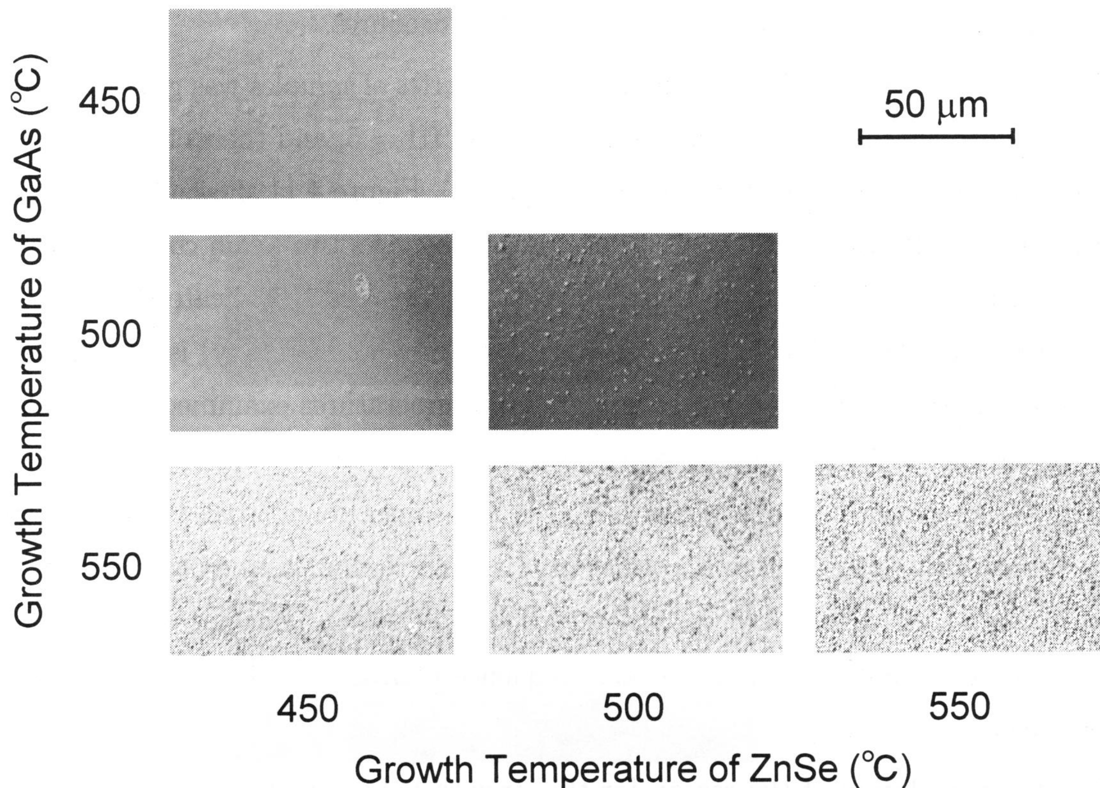

Figure 4.10: Surface morphology of GaAs (1200 Å) / ZnSe (450 Å) fabricated at various ZnSe and GaAs growth temperatures.

case of homoepitaxy, the surface morphology of GaAs grown at 550°C was much superior to those grown at 450 – 500°C. Taking this fact into account, we can conclude that the degradation observed in the heteroepitaxy originates from the interface between GaAs and ZnSe. There are two possible interpretations for this phenomenon; (1) the growth mode of GaAs on ZnSe at 550°C is three-dimensional, and (2) Se evaporation during the exposure of ZnSe to 550°C roughens the surface of ZnSe already before the GaAs growth, which may happen owing to the high vapor pressure of group VI elements. To clarify which is responsible for the experimental results in Fig. 4.10, ZnSe was grown at 450°C, and subsequently, exposed to 550°C under a TBAs flux for 6 s. The ZnSe surface morphology before and after exposed to 550°C was compared by atomic force microscope (AFM), but no appreciative difference was detected, indicating that the interpretation (2) mentioned above does not fit in with the present experiments. Namely, the growth temperature of GaAs is essential

to determine the growth mode of GaAs. In the following discussions, therefore, the growth temperature for ZnSe, which hardly influences the GaAs growth mode, is adjusted to be the same as that of GaAs to facilitate the growth procedures.

In order to ensure the above results, a different series of samples was grown at 450, 500, and 550°C without changing the gas flow ratio of V/III = 5, and their cross sections were observed by transmission electron microscope (TEM). Figure 4.11 shows TEM bright field images of the (110) cross sections of the samples, where the two beam condition with $\boldsymbol{g}$ = 002 was adopted to clarify the interfaces. These images clearly indicate that the growth mode of the GaAs buffer layers on the GaAs substrates (homoepitaxy) is two-dimensional within the experimental resolution at any growth temperatures examined here. The ZnSe layers grown on GaAs are also uniform in thickness at all temperatures. In contrast, although GaAs grown on ZnSe below 500°C is two-dimensional, that grown at 550°C is highly three-dimensional, which is consistent with the Nomarski microscope observations shown in Fig. 4.10. These findings indicate that the growth behavior of GaAs on ZnSe is quite different from that of the reverse sequence of ZnSe on GaAs and that of GaAs homoepitaxy.

For the elucidation of the reason for this growth behavior, it was attempted to grow the same structures as shown in Fig. 4.9 at 550°C, varying the V/III ratio from 2 to 10. Since the flow rate of TEGa was unchanged, the variation of the V/III ratio means the flow rate variation of TBAs. Cross-sectional TEM bright field images are shown in Fig. 4.12. They reveal that as the V/III ratio increases, *i.e.*, as [TBAs] increases, GaAs becomes flat, whereas as the V/III ratio decreases, GaAs exhibits 3D island-type growth, in which the formed islands tend to separate from each other.

Figure 4.13 shows variation of the GaAs island height as a function of the V/III ratio. The island height was measured from cross-sectional TEM images taken at several different positions on the samples, and for the flat layers grown at 450 or 500°C, that refers to the layer thickness. For GaAs grown at 550°C, as the V/III ratio increases, GaAs shows a stronger tendency of 2D growth as seen in Fig. 4.12, and correspondingly, the island height decreases. At high V/III ratios, the island height approaches the thickness of the flat layers. This result strongly suggests that the mechanism behind the formation of the GaAs islands on ZnSe, that is, the 3D growth of GaAs on ZnSe, is mainly related not to desorption but to migration. This is because if desorption were the main cause of the island formation,

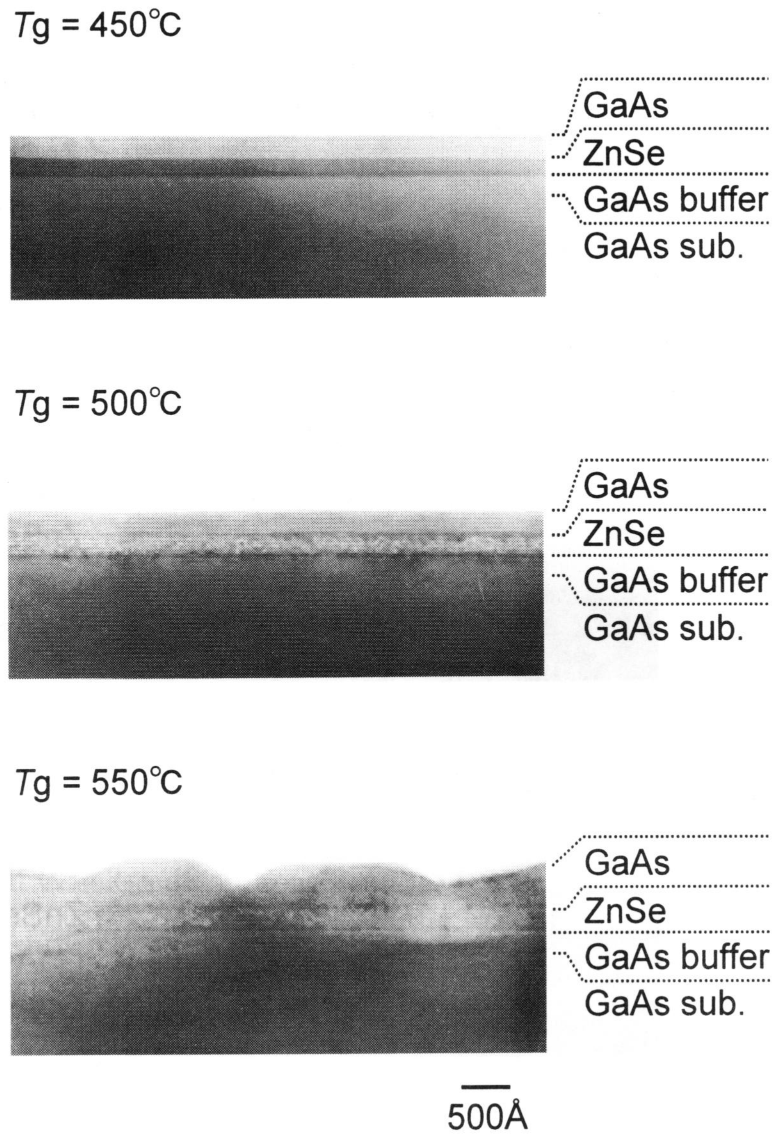

Figure 4.11: TEM bright field images of the (110) cross sections of GaAs (200 Å) / ZnSe (200 Å) heterostructures grown at various temperatures. The V/III ratio was fixed at 5.0.

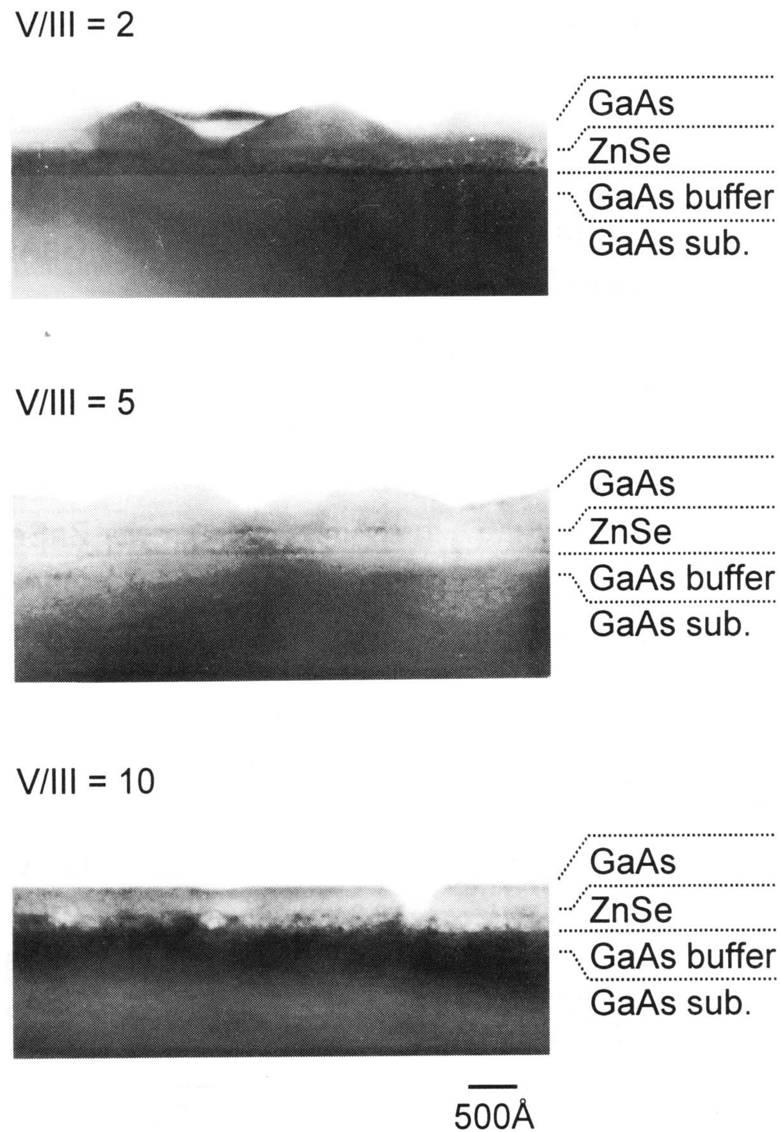

Figure 4.12: TEM bright field images of the (110) cross sections of GaAs (200 Å) / ZnSe (200 Å) heterostructures grown under various V/III ratios. The growth temperature was kept constant at 550°C.

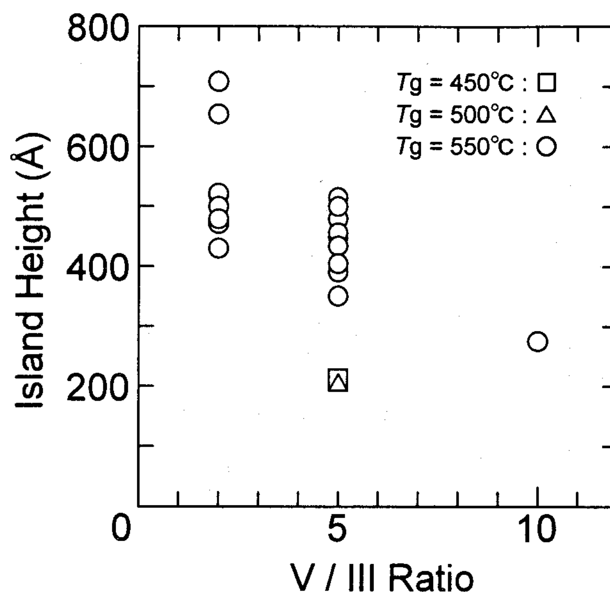

Figure 4.13: Dependence of the GaAs island height on the V/III ratio.

the island height would decrease with decrease of the V/III ratio.

To confirm this assertion, ZnSe-GaAs multilayered structures were grown at 500 and 550°C without changing the duration of supplying source precursors. Since the growth rates for both ZnSe and GaAs are independent of growth temperatures above 500°C, the nominal mean thickness of 3D GaAs grown at 550°C must be equal to the thickness of 2D GaAs grown at 500°C unless desorption occurs. XRD analysis of multilayered structures was applied for the evaluation of the mean thickness; the XRD pattern has a fundamental peak at the angular position determined by the thickness ratio of a set of the alternating layers, from which the mean thickness can be estimated. Figure 4.14 shows the double-crystal XRD patterns of the multilayered structures grown at 500 and 550°C. Those were obtained in the vicinity of the GaAs 004 Bragg angle. The designed structure is two periods of GaAs (200 Å) / ZnSe (250 Å). The XRD profile of the multilayer grown at 500°C has satellite peaks which are denoted by the closed arrows in the figure, indicating the good periodicity. On the other hand, satellite peaks disappeared in the profile of the multilayer grown at 550°C. This is due to the breakdown of the periodicity by 3D growth of GaAs at 550°C. However, since the fundamental peaks (open arrow) of both multilayers are located at the same angle, we can conclude that the mean thickness of 3D GaAs is equal to the layer thickness of 2D GaAs. This finding provides the evidence for the above assertion that

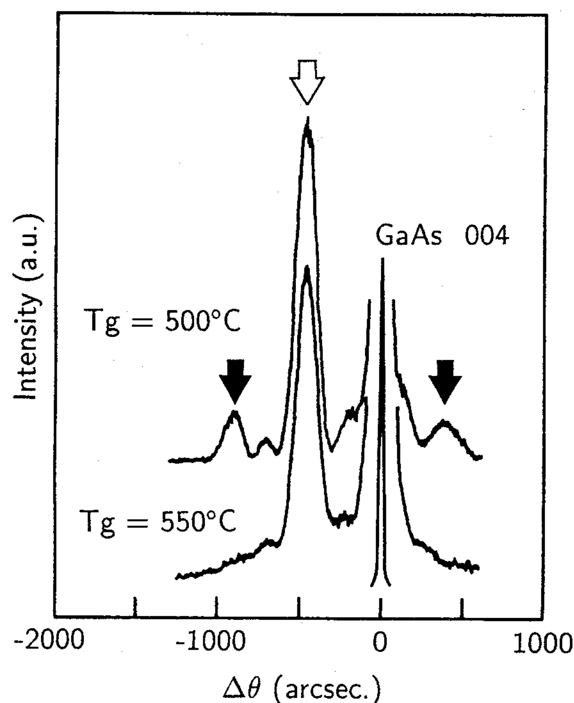

Figure 4.14: Double-crystal XRD patterns of GaAs (200 Å) / ZnSe (250 Å) × 2 multilayered structures grown at 500 and 550°C. The symbol ⇓ designates the fundamental peak and ↓ satellite peaks.

migration, not desorption, causes the formation of the GaAs 3D islands.

Generally, in heteroepitaxy of dissimilar materials, the surface diffusion coefficient of adspecies is crucial to determine the growth mode. Lower growth temperatures will mean smaller, or perhaps even negligible, diffusion coefficients, and will therefore promote 2D growth [12]. A high density of adspecies may also bring about the 2D growth mode, because it inhibits migration and reduces epilayer surface roughness. These tendencies agree quite well with our results shown in Figs. 4.11 and 4.12. The problem is what the migrating species are. We investigated the effects of TEGa and TBAs on the ZnSe surface in Sec. 4.2. When ZnSe was annealed in a TBAs ambient, ZnSe was drastically etched, for example, at the rate of 150 Å/min under the conditions of T_a = 550°C and [TBAs] = 20 μmol/min, whereas ZnSe was not appreciably etched thermally. Therefore, As-containing molecules, which are generated through the decomposition of TBAs, are not the cause of island formation, because an As-related process includes a desorption process. On the other hand, when ZnSe was exposed to TEGa, the ZnSe surface became rough due

to the nucleation of adsorbed Ga, indicating that metallic Ga may easily migrate on ZnSe. These results suggest that the Ga atoms and/or Ga-related molecules are the migrating species, which bring the 3D growth of GaAs.

Here, differences in the growth mode of GaAs on ZnSe in MBE and in MOVPE are discussed. In the case of MBE, the growth temperature for GaAs must be lowered as described in Sec. 4.1, while the present results indicate that, in MOVPE, GaAs can be grown two-dimensionally on ZnSe without changing the growth temperature. Possible factors responsible for this difference are the growth ambient, the Ga precursors, and the As precursors. Hydrogen used in MOVPE may terminate the surface atoms of ZnSe and may alter the growth behavior. However, since the hydrogen termination will enhance the migration of Ga-related adspecies by decreasing the number of dangling bonds appearing at the surface, the growth becomes three-dimensional rather in MOVPE than in MBE, which does not agree with the experimental results. With respect to the Ga precursors, the metalorganic source of TEGa is decomposed into Ga metal completely in the growth temperature region investigated here [5], and therefore, there is no difference between MBE and MOVPE. From the above, we attribute, at present, the difference observed between MBE and MOVPE to the As precursors. The As species being provided during MBE and GSMBE have been reported to be As_4 and As_2 molecules, respectively [1,4]. On the other hand, TBAs decomposes into AsH and AsH_3 with generating C_4H_{10} and C_4H_8 [6,7]. Note that As in the As-As bonds is neutral, and that As in the As-H bonds is negatively polarized, owing to the greater electron affinity for As than for H. Since the cation atoms making bonds with As are positively polarized at the sample surface, the reaction with negatively polarized As might take place more easily than with neutral As. This coulomb potential causes the higher reactivity of GaAs on ZnSe in MOVPE and, correspondingly, leads to the 2D growth.

4.3.2 Initial growth rate

In heteroepitaxy, the initial growth rate is often different from the growth rate of the thick layer (quasi-homoepitaxy). In order to estimate the initial growth rate, multilayered structures consisting of thin ZnSe and GaAs layers were fabricated at 450 and 500°C, which realize the 2D growth of GaAs as demonstrated in the previous section. The layer thickness of each constituent was estimated by double-crystal XRD analysis and TEM observation.

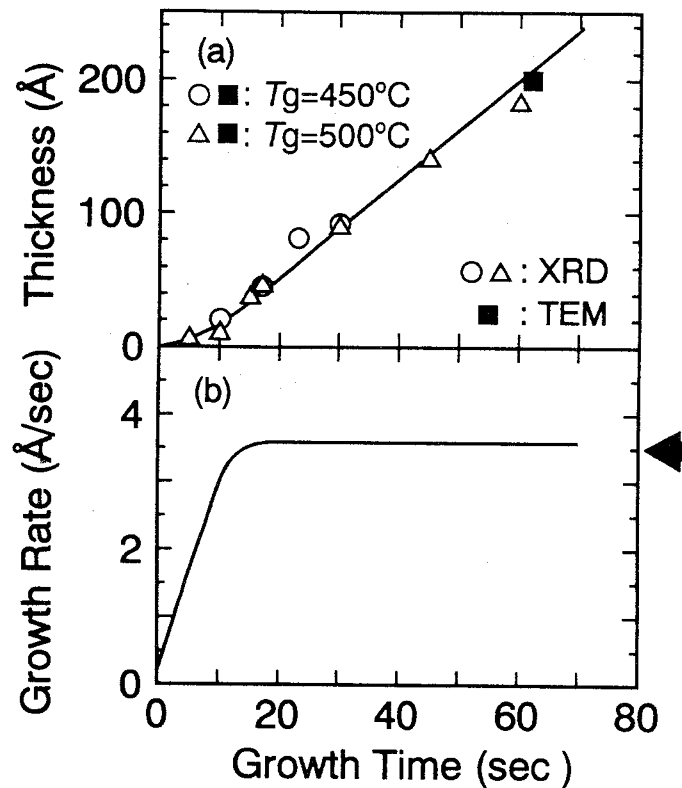

Figure 4.15: (a) Layer thickness and (b) growth rate of GaAs on ZnSe as a function of the growth time. The growth rate was derived from differential of the thickness by the growth time. The arrow indicates the growth rate calculated from a thick GaAs layer.

Figure 4.15(a) shows the GaAs layer thickness as a function of the growth time. The results obtained by the XRD and TEM observation are on the identical curve, providing validity of the method to estimate the thickness. The thickness differentiated by the growth time gives the growth rate and its variation due to the growth time is shown in Fig. 4.15(b). As can be seen, the growth rate at the beginning is approximately 0.2 Å/s, and as the growth continues, it increases and saturates at the growth rate calculated from a thick GaAs layer (3.5 Å/s) which is indicated by the arrow. The slower growth rate at an early growth stage means the low sticking probability of Ga to ZnSe because Ga determines the growth rate of GaAs under the present growth conditions. This is consistent with the tendency of the observed growth mode; since the low sticking probability of Ga enhances migration of Ga, GaAs on ZnSe tends to exhibit 3D growth, compared with GaAs homoepitaxy. Although the initial growth rate should essentially depend on the growth temperature, owing to the

temperature dependence of the sticking probability, that is not observed experimentally in Fig. 4.15. The variation of the initial growth rate due to the growth temperature was likely to be within the experimental resolution.

4.4 Nucleation Processes of GaAs on ZnSe

In Sec. 4.3, it has been revealed that either the 2D or 3D growth mode occurs depending mainly on the growth temperature. In this section, the nucleation processes in each growth mode are investigated in more detail by means of AFM. To observe the nucleation processes clearly, the ZnSe surface before the growth of GaAs was prepared to consist of atomically flat terraces, islands 1-ML high, and 1 ML steps derived from the unintentional misorientation of the substrate. The procedure for obtaining the atomically flat ZnSe surface was described in chapter 2.

4.4.1 Two-dimensional growth

GaAs 40-Å thick was grown on the atomically flat ZnSe at 400 and 450°C. It has already been described in Sec. 4.3 that the growth temperature of 450°C brings the 2D growth mode. Here, the growth temperature of 400°C as well was examined for the comparison. Figure 4.16 shows AFM images of GaAs grown at (a) 400 and (b) 450°C. Magnified images of (a) and (b) are also shown in (c) and (d), respectively. We emphasize that the height, which was estimated from height profiles revealed by AFM, of all structures observed in Fig. 4.16 such as steps and islands is 1 ML. In Fig. 4.16, the region with brighter contrast is higher by 1 ML and that with the same contrast is atomically flat: For example, four different contrasts can be seen in Fig. 4.16(a) or (b), which means that the difference in height between the regions with the brightest and the darkest contrast is 3 ML's.

From a rough inspection of Figs. 4.16(a) and (b), it is found that the growth temperatures basically do not change the surface structures in the order of a few hundred of nanometers. The height of all structures is 1 ML as was mentioned, and 1 ML steps, which are pointed by arrowheads in the figures, are clearly seen on both samples, indicating that the growth of GaAs on ZnSe at 400 and 450°C is in the 2D growth mode in the atomic level. The surface morphology of ZnSe shown in chapter 2 is similar to Figs. 4.16(a) and (b), and furthermore it has been confirmed by AFM observations of thinner GaAs that the

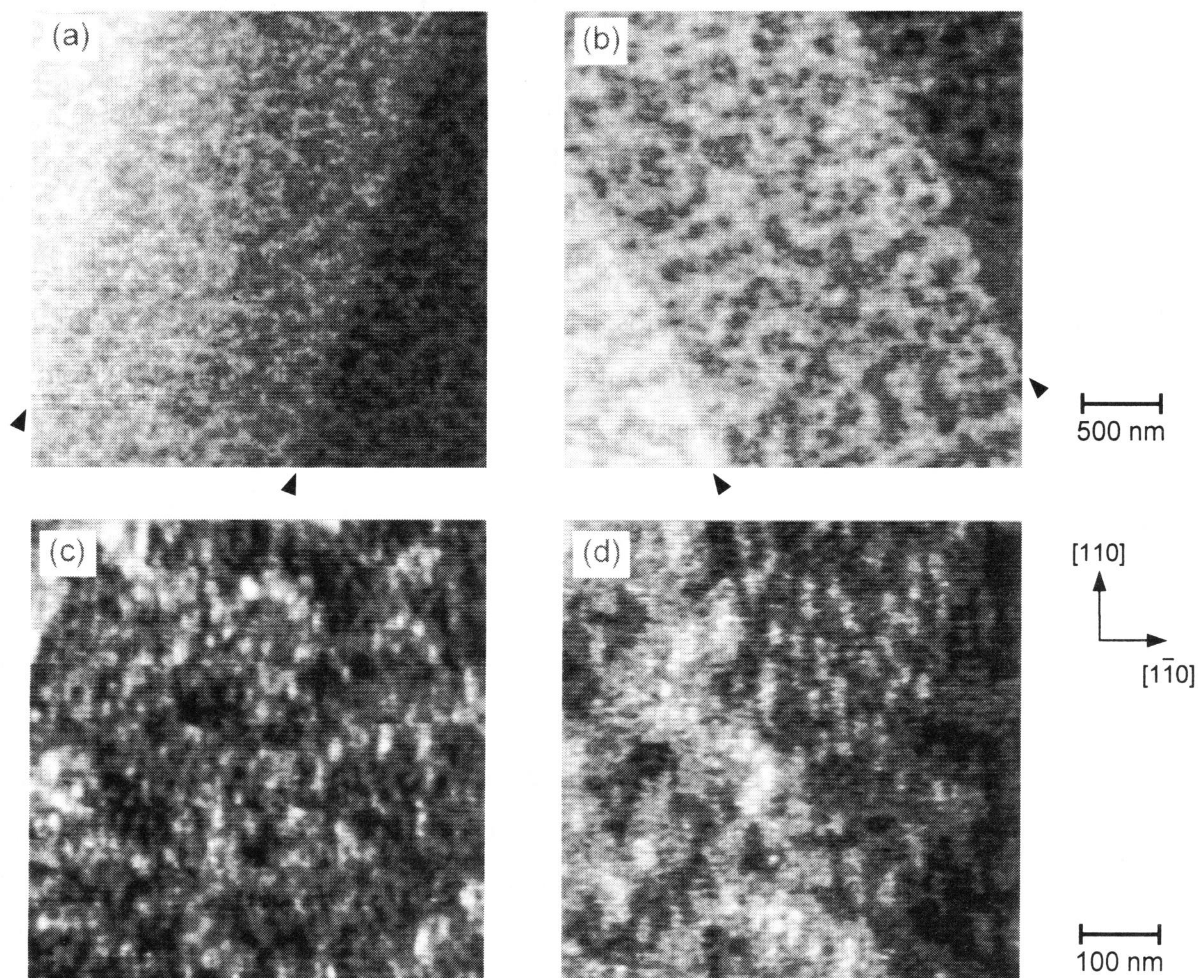

Figure 4.16: AFM images of 40-Å-thick GaAs grown on ZnSe at (a) 400 and (b) 450°C. Magnified images of (a) and (b) are also shown in (c) and (d), respectively. Indicated by arrowheads are 1 ML steps derived from the unintentional misorientation of the substrates.

2D growth of GaAs on ZnSe occurred at very early stages of the growth. These experimental results indicate that the 2D growth of GaAs preserves surface structural features of the underlying ZnSe layers to the surface of GaAs, and that the interface between GaAs and ZnSe is quite abrupt.

On the other hand, the detailed observations revealed differences due to the growth temperatures. On the surface of GaAs grown at 400°C, there are a significant number of 2D nuclei as shown in Fig. 4.16(c). The dimensions of the 2D island were typically 30 nm in the [110] direction and 10 nm in the $[1\bar{1}0]$ direction. The surface roughness determined from an AFM height profile was ± 1 ML, indicating that the growth was in the multinucleation mode where 2D nucleation occurs before the underlying 2D nuclei complete 1 ML growth. Regarding GaAs grown at 450°C, 2D islands are still observable, though the higher growth temperature brought the lower density and the greater dimensions of the islands; typically 50 nm in the [110] direction and 20 nm in the $[1\bar{1}0]$ direction. Consequently, the growth mode approached from the multinucleation mode to the layer-by-layer mode. These tendency can be interpreted well in terms of enhancement of migration of adatoms at the higher temperature.

For the comparison, GaAs homoepitaxy was performed at 400 and 450°C. The surface structures were quite similar to those of GaAs grown on ZnSe. The direction in which the 2D islands were elongated was [110] in the homoepitaxy as well [13]. Therefore, it is reasonable to conclude that GaAs grown on ZnSe at 400 or 450°C possesses the structural properties equivalent to those of homoepitaxial layers.

4.4.2 Three-dimensional growth

To discuss the nucleation processes during the 3D growth, GaAs with various equivalent thickness was grown at 550°C. In the case of homoepitaxy, the growth rate of GaAs is constant in the growth temperature range of 450 – 700°C. Hence, the "equivalent" thickness, *i.e.*, deposition quantity, of GaAs on ZnSe can be estimated using the relationship between the growth time and the layer thickness elucidated for the growth temperatures of 450 and 500°C, which is already shown in Fig. 4.15. Since the layer thickness is not proportional to the growth time, the estimated equivalent thickness will appear in the text together with the growth time for reference.

Figure 4.17 shows AFM images and schematic views, deduced from the images, of

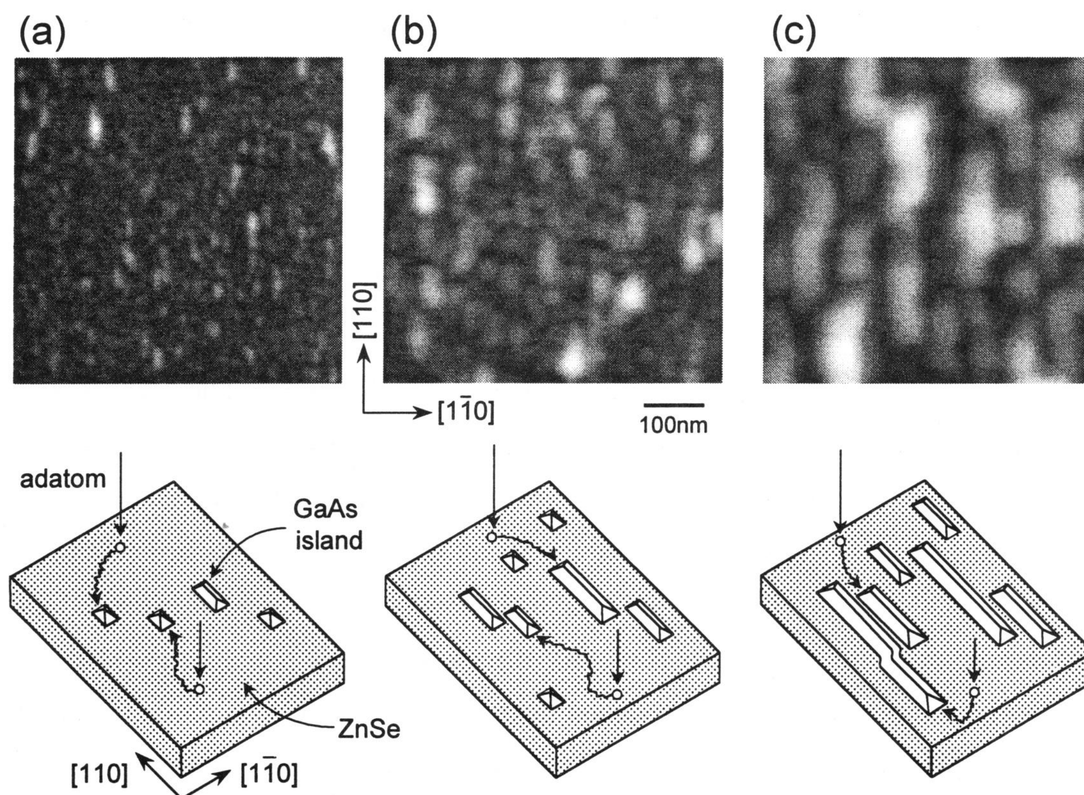

Figure 4.17: AFM images and schematic views of GaAs grown on ZnSe. Equivalent growth thicknesses are (a) 1, (b) 3, and (c) 24 ML's.

GaAs grown on ZnSe at 550°C. In Fig. 4.17, the equivalent thicknesses of GaAs are (a) 1 (growth time: 3 s), (b) 3 (6 s), and (c) 24 ML's (24 s). The V/III ratio was set at two so as to promote the 3D growth (see Fig. 4.12). As shown in Fig. 4.17(a), the 3D growth of GaAs is observed even at the very beginning of the heteroepitaxy, and therefore, the growth mode is classified as the Volmer-Weber mode. The total volume of the GaAs 3D islands in Fig. 4.17(a) was evaluated and turned out to correspond to the average thickness of 3.8 Å, which was close to 1 ML. This finding supports the conclusion that the growth mode is the Volmer-Weber mode. It is worth noting that in order to grow 1 ML GaAs on ZnSe, the amount of the supplied source precursors must be nearly equal to that for 3 ML's growth in homoepitaxy. This implies that the sticking coefficient for Ga to ZnSe is at least three times as low as that to GaAs. Owing to the low sticking coefficient, Ga adatoms can migrate on ZnSe relatively freely and coalesce with each other frequently (some of them will desorb from the ZnSe surface, while migrating). Coalescence often brings about the formation of

a 2D nucleus. However, when the sticking coefficient between adatoms and the underlying layer is low, 3D nucleation can occur more easily than 2D nucleation because deposition on itself (3D nucleus) is more stable than that on a foreign material (2D nucleus). Concerning the present material combination, the GaAs-on-GaAs structure (3D nucleus) is supposed to be preferable to the GaAs-on-ZnSe structure (2D nucleus). On the other hand, the role of a higher growth temperature is to decrease the sticking coefficient further and to enhance migration, by which the possibility of coalescence of adatoms is increased. Because of those factors, *i.e.*, the low sticking coefficient and the high possibility of coalescence, 3D GaAs islands rather than 2D islands are formed on ZnSe at 550°C. The low sticking probability of Ga to ZnSe has already been pointed out in Fig. 4.15 using 2D GaAs grown at 450 and 500°C. Therefore, the occurrence of the 3D growth at the higher growth temperature of 550°C is quite natural.

As the growth proceeded, anisotropy in the 3D island shape became pronounced [Figs. 4.17(b) and 4.17(c)]. The islands are elongated in the [110] direction. From Fig. 4.17, the [110], [$1\bar{1}0$] and vertical growth rates were estimated to be 80, 20, and 10 Å/s, respectively. The [110] growth rate is slightly overestimated because the influence of the coalescence of islands in the corresponding direction was neglected. However, it is evident that the [110] growth rate is much faster than the [$1\bar{1}0$] and the vertical growth rates. This indicates that migrating Ga adatoms on the ZnSe surface are preferably incorporated into the GaAs 3D islands from the [110] direction.

In GaAs homoepitaxy, diffusion anisotropy due to surface reconstructions often causes anisotropic lateral growth; GaAs islands in MOVPE and in MBE are elongated in the [110] direction [13, 14] and in the [$1\bar{1}0$] direction [15], respectively, and this difference is ascribed to the different surface reconstructions. During MBE, the (2×4) reconstruction, on which As dimers are in the [$1\bar{1}0$] direction, appears, while during MOVPE, (4×4), on which As dimers are in the [110] direction, coexists [16]. Note that the direction of the island elongation agrees with the dimer direction. On the other hand, the primary reconstruction of the ZnSe surface which is observed during MBE growth under Se-rich conditions is (2×1). There is no other reconstruction for the Se-terminated surface, and the (2×1) reconstruction seems to appear also during MOVPE growth [17]. However, this surface possesses Se dimers along [$1\bar{1}0$] and this orientation differs by 90° from the direction of the island elongation. Therefore, we consider that the ZnSe surface structure does not

influence the diffusion of Ga adatoms on it. This conclusion is reasonable because the interaction between Ga adatoms and ZnSe is quite weak as described above, which may lead to small anisotropy in diffusion.

Accordingly, in order to explain the anisotropic lateral growth of GaAs on ZnSe, the bond configuration should be considered. The indices of the planes which construct the GaAs islands on ZnSe have not been identified. However, since any planes parallel to [110] ([$1\bar{1}0$]) consist of [$1\bar{1}0$] ([110]) steps, it will be enough to take into account the incorporation of adatoms to [110] and [$1\bar{1}0$] steps. A Ga atom at a [110] step of the GaAs 3D island is bound with three bonds; one to the step side and two to the step bottom [(001) side]. A Ga atom at a [$1\bar{1}0$] step, on the other hand, is bound to the step bottom with two bonds but not to the step side. The sticking probability of an impinged Ga adatom to a step may be larger when it is bound by the larger number of bonds at the step. Therefore, Ga adatoms are more frequently incorporated into the [110] step than into the [$1\bar{1}0$] step, resulting in the faster [110] growth rate.

4.5 Application to Low Dimensional Structures

A novel approach to fabricate quantum structures with fractional dimensionality emerges from the growth behavior discussed above. Namely, quantum well (QW) structures can be fabricated using the 2D growth mode of GaAs, while the GaAs 3D growth may decrease the dimensionality from 2D QW to zero-dimensional (0D) quantum dot (QD) structures. Let us suppose that GaAs is grown on ZnSe under the conditions which bring the 3D growth, that is, high growth temperatures and low V/III ratios. If the growth time is sufficiently short to separate each GaAs island [for example, see Fig. 4.17(a)], ZnSe overgrowth realizes QD's where GaAs dots are buried in ZnSe. As the growth of 3D GaAs proceeds, the GaAs islands develop preferably in the [110] direction as shown in Figs. 4.17(b) and (c). Therefore, GaAs buried in ZnSe at this time may act as quantum wires. Here we will show the possibility in fabricating such quantum structures.

Figures 4.18(a) and (b) are TEM bright field images of the (110) cross sections of multilayered structures fabricated under the growth conditions of (a) T_g = 500°C and V/III = 5, and (b) T_g = 550°C and V/III = 2. In the images, bright GaAs and dark ZnSe show marked contrast. It is clearly seen that, under the growth conditions of Fig. 4.18(a),

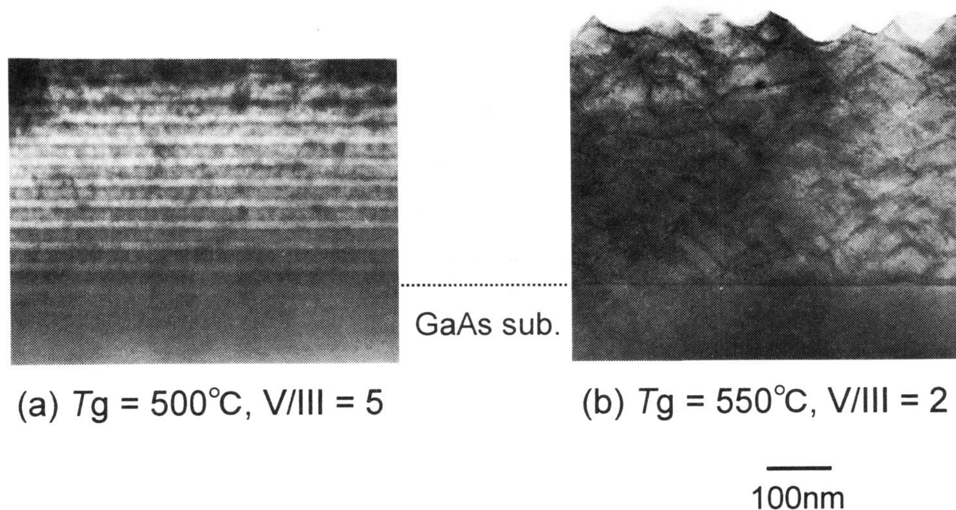

Figure 4.18: Cross-sectional TEM bright field images of ZnSe-GaAs multilayered structures fabricated under the conditions of (a) $T_g = 500°C$ and V/III = 5, and (b) $T_g = 550°C$ and V/III = 2. Bright and dark images correspond to the GaAs and ZnSe layers, respectively.

the growth of GaAs on ZnSe is two-dimensional and a QW structure with fairly good periodicity was fabricated. On the other hand, the conditions of Fig. 4.18(b) brought about the 3D growth of GaAs on ZnSe, as predicted by the previous arguments, and periodicity was considerably degraded. However, it must be noted that the ZnSe layers separate the GaAs islands. Furthermore, FWHM of the XRD pattern was evaluated to be as narrow as 46 arcsec, which is comparable with that of QW shown in Fig. 4.18(a). These findings suggest that high-quality GaAs QD's can be buried into ZnSe. To give more convincing evidence, GaAs islands surrounded by ZnSe were fabricated under the same conditions for Fig. 4.18(b), and a (110) cross section was observed by TEM. The bright field image is indicated in Fig. 4.19. GaAs shows the Volmer-Weber growth mode and each island is isolated completely by the ZnSe layers. For this figure, relatively large GaAs islands were grown to facilitate the observation, and the quantum effects will not appear. Also, the islands are probably elongated in the [110] direction, as is deduced from Fig. 4.17. However, this preliminary experiment strongly promises successful fabrication of GaAs QD's buried into ZnSe by reducing the island size.

So far, the Stranski-Krastanov mode, where the initial nucleation occurs in a 2D manner but above a certain thickness island formation occurs during strain release processes,

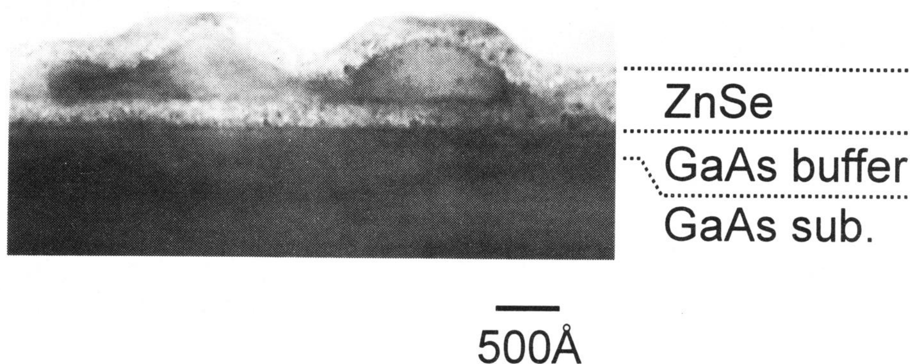

Figure 4.19: TEM bright field image of the (110) cross section of GaAs islands buried into ZnSe. The growth conditions are T_g = 550°C and V/III = 2.

has been used for fabricating QD's [18-20]. The InAs-GaAs system is a good example. In contrast, the procedure proposed here to fabricate low dimensional structures is based on a novel principle, that is, the Volmer-Weber growth mode due to the heterovalency, and does not require strain as a driving force for 3D growth. The advantages of this procedure are that QD's are not accompanied by a wetting layer which acts as a QW, and that the size of QD's can be controlled without caring about the introduction of misfit dislocations. Future studies are expected to bring fruitful results.

4.6 Summary

With the purpose of establishing the growth procedure to provide high quality and structurally well-defined GaAs on ZnSe(001), the flow sequence of the source precursors at the interface and the growth behavior were investigated. It was found that Ga metal generated through TEGa dissociation deposited three-dimensionally on ZnSe, while TBAs drastically etched ZnSe, typically at the rate of 150 Å/min. As the etching mechanism, desorption of Zn and Se from the ZnSe surface via the formation and evaporation of Zn_3As_2 and As_xSe_{1-x}, respectively, was proposed. On the basis of these results, GaAs growth on ZnSe was decided to be initiated by TBAs followed by TEGa.

The growth behavior of GaAs on ZnSe was interpreted in terms of migration of Ga atoms and/or Ga-related molecules. Owing to the low sticking coefficient of Ga on ZnSe,

enhancement of migration by raising the growth temperature to ~550°C with low V/III ratios (≤ 5) caused 3D growth, which was classified as the Volmer-Weber mode. On the other hand, with low growth temperatures ($\leq$ 500°C) or high V/III ratios (≥ 10), the Ga migration was suppressed and the resultant GaAs surface became two-dimensional. In particular, GaAs grown at 400 or 450°C showed atomically flat surfaces. As a potential application of the variation of the growth behavior, fabrication of the ZnSe-GaAs quantum structures with fractional dimensionality was proposed and the preliminary results were demonstrated.

References

[1] N. Kobayashi and Y. Horikoshi, Jpn. J. Appl. Phys. **29**, L236 (1990).

[2] S. Zhang and N. Kobayashi, Appl. Phys. Lett. **60**, 883 (1992).

[3] H. H. Farrell, M. C. Tamargo, J. L. de Miguel, F. S. Turco, D. M. Hwang, and R. E. Nahory, J. Appl. Phys. **69**, 7021 (1991).

[4] J. L. House, D. J. Dougherty, G. S. Petrich, L. A. Kolodziejski, E. P. Ippen, and G. -C. Hua, Appl. Surf. Sci. **104-105**, 472 (1996).

[5] P. W. Lee, T. R. Omstead, D. R. Mckenna, and K. F. Jensen, J. Crystal Growth **85**, 165 (1987).

[6] P. W. Lee, T. R. Omstead, D. R. Mckenna, and K. F. Jensen, J. Crystal Growth **93**, 134 (1988).

[7] C. A. Larsen, N. I. Buchan, S. H. Li, and G. B. Stringfellow, J. Crystal Growth **94**, 663 (1989).

[8] S. Akram, H. Ehsani, and I. B. Bhat, J. Crystal Growth **124**, 628 (1992).

[9] B. Chelluri, T. Y. Chang, A. Ourmazd, A. H. Dayem, J. L. Zyskind, and A. Srivastava, Appl. Phys. Lett. **49**, 1665 (1986).

[10] V. Mastelaro, H. Dexpert, S. Benazeth, and R. Ollitrault-Fichet, J. Solid State Chem. **96**, 301 (1992).

[11] S. R. Elliott and A. V. Kolobov, Philos. Mag. B **61**, 853 (1990).

[12] For example, see J. C. Bean, L. C. Feldman, A. T. Fiory, S. Nakahara, and I. K. Robinson, J. Vac. Sci. Technol. A **2**, 436 (1984).

[13] A simple model for the formation of anisotropic islands can be found in H. Asai, J. Crystal Growth **80**, 425 (1987).

[14] M. Kasu and N. Kobayashi, J. Appl. Phys. **78**, 3026 (1995).

[15] E. J. Heller and M. G. Lagally, Appl. Phys. Lett. **60**, 2675 (1992).

[16] F. Reinhardt, W. Richter, A. B. Müller, D. Gutsche, P. Kurpas, K. Ploska, K. C. Rose, and M. Zorn, J. Vac. Sci. Technol. B **11**, 1427 (1993).

[17] Of course, ZnSe surfaces under atmospheric pressure must be investigated in future studies, though, for GaAs, it has been confirmed that surface reconstructions at atmospheric pressure are the same as those in ultra high vacuum. See I. Kamiya, D. E. Aspnes, H. Tanaka, L. T. Florez, J. P. Harbison, and R. Bhat, Phys. Rev. Lett. **68**, 627 (1992).

[18] D. Leonard, M. Krishnamurthy, C. M. Reaves. S. P. DenBaars, and P. M. Petroff, Appl. Phys. Lett. **63**, 3203 (1993).

[19] J. Oshinowo, M. Nishioka, S. Ishida, and Y. Arakawa, Appl. Phys. Lett. **65**, 1421 (1994).

[20] Y. Nabetani, T. Ishikawa, S. Noda, and A. Sasaki, J. Appl. Phys. **76**, 347 (1994).

Chapter 5

Control of Interface Properties in GaAs-on-ZnSe Heterovalent Heterostructures

5.1 Introduction

One of the characteristic features of heterovalent heterostructures is the tunability of the band offsets [1-7]. In chapter 3, we have succeeded in controlling the band offsets in the ZnSe-on-GaAs(001) [ZnSe/GaAs(001)] heterostructures between 0.6 and 1.1 eV, where the interface atomic configuration was manipulated through a Zn or Se treatment of GaAs surfaces before beginning the ZnSe growth. Therefore, if the band offsets in the inverse structure, *i.e.*, the GaAs-on-ZnSe (GaAs/ZnSe) heterostructure, can be controlled, that leads to fabrication of ZnSe-GaAs multilayered structures whose properties regarding carrier transport and confinement can be designed.

Subsequently to the establishment of the growth procedure of GaAs/ZnSe in chapter 4, in this chapter, efforts are devoted to the control of the band offsets in the GaAs/ZnSe heterostructure. The basic idea is the same as the case of ZnSe/GaAs, that is, the interface atomic configuration is modified, while the growth conditions for both ZnSe and GaAs remain unchanged, in order to focus discussions on the interface engineering. It has been revealed in the previous chapter that the ZnSe surfaces are etched by thermal annealing in a hydrogen ambient, and more drastically, in an ambient of the As source precursor of tertiarybutylarsine (TBAs). These properties are utilized to control the interface atomic configuration and, correspondingly, the band offsets. Since abrupt interfaces make it easier to elicit the effect of the interface atomic configuration on the band offsets, the nucleation of

GaAs on ZnSe(001) is kept two-dimensional (2D) in the atomic level, referring to the results obtained in chapter 4. The valence band offsets are estimated by x-ray photoemission spectroscopy (XPS).

5.2 Preparation of GaAs/ZnSe Heterointerfaces

An underlying ZnSe layer 100-Å thick was grown at 450°C on the GaAs buffer layer, using diethylzinc (DEZn) and dimethylselenium (DMSe) as source precursors. Molar flow rates of DEZn and DMSe were 1.2 and 12 μmol/min, respectively. After the growth, the ZnSe layer was successively annealed at 450°C for 10 min with DMSe flow. The growth and annealing at 450°C makes the ZnSe surface flat to the atomic level, as mentioned in chapter 2; the surface consists of atomically flat terraces, islands 1-monolayer (ML, 1 ML = 2.8 Å) high, and 1 ML steps derived from the unintentional misorientation of the substrate. These features indicate that the surface of ZnSe is fully covered with either Zn or Se atoms, which is a favorable surface to control the atomic configuration.

GaAs was grown on the ZnSe layer. Since the underlying ZnSe is atomically flat, the atomically flat GaAs thin film can be an indication of the abrupt interface between GaAs and ZnSe. Therefore, the growth temperature (T_g) of GaAs on ZnSe was set relatively low at 400 or 450°C, because these temperatures bring the 2D growth in the atomic level but GaAs grown on ZnSe above 550°C exhibits three-dimensional surfaces (*cf.* chapter 4). Molar flow rates of triethylgallium (TEGa) and TBAs were 10 and 50 μmol/min, respectively. The temperature program and the flow sequence of the source precursors at the GaAs/ZnSe interface are shown in Fig. 5.1. During the interval between the growth of ZnSe and GaAs, only hydrogen was supplied for purging DMSe. The growth of GaAs began with an initial exposure of ZnSe to TBAs. The Ga-initiated growth of GaAs was not examined here because an atomic force microscopy (AFM) observation revealed that the surface of GaAs whose growth was initiated by TEGa was three-dimensional. During the exposure of ZnSe to TEGa, Ga atoms probably deposited to form Ga droplets on ZnSe, resulting in the rough surface. This result is consistent with the result in Sec. 4.2.3, though the growth temperatures are different.

In order to achieve the tunability of the band offsets at compensated neutral interfaces such as those shown in Fig. 1.2, the GaAs/ZnSe interface structures were experimentally

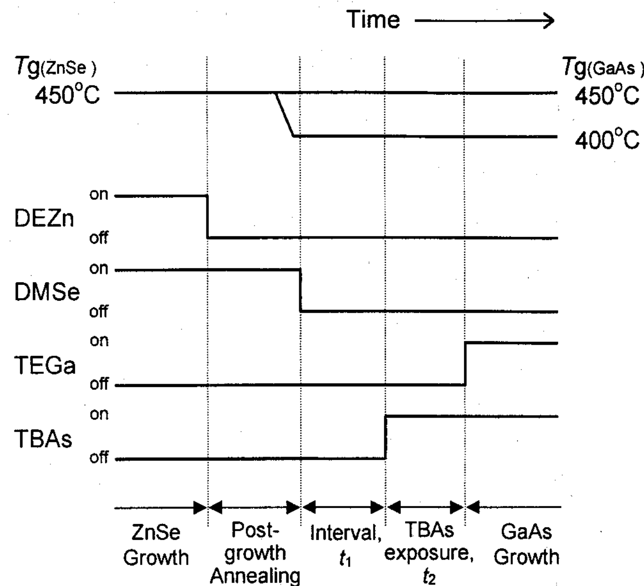

Figure 5.1: The temperature program and the flow sequence of the source precursors at the GaAs/ZnSe interface.

controlled by means of the thermal etching of ZnSe in a hydrogen or a TBAs ambient. Namely, durations of the interval (t_1) and the TBAs-exposure (t_2) were varied as parameters, and the dependence of the band offsets on these durations was investigated. It must be noted that as far as this study is concerned, the durations of the interval and the TBAs-exposure were altered within the limits that the atomically flat surface and, consequently, interface of the GaAs/ZnSe heterostructure can be maintained. This was proved by the AFM observations.

5.3 Control of Band Offsets

5.3.1 XPS measurements

The experimental setup for the XPS measurements and the procedure to extract the band offsets are the same as those in chapter 3. The measurements were performed *ex situ*, and hence the GaAs surface contaminated during the exposure to air was lightly etched with Ar^+ after being loaded into the XPS chamber. The detected signals were $3d$ core levels of Zn, Se, Ga, and As. Since the region detectable by the present XPS measurements is 45 Å from the surface, the ZnSe layer thickness of 100 Å prevents the Ga and As $3d$ photoelectrons generated in the GaAs buffer layer underneath the ZnSe layer

from being detected. Therefore, the obtained Ga and As 3*d* signals are the ones from GaAs on ZnSe. Thickness of the GaAs layers on ZnSe for XPS was 20 – 30 Å, which made it possible to obtain the signals from both sides of the GaAs/ZnSe interface simultaneously. Consequently, the energy separations between core levels, from which the band offsets are estimated (see Fig. 3.3), could directly be estimated.

In chapter 3, possible errors involved in the XPS measurements of ZnSe/GaAs were described. Here, again, those in the GaAs/ZnSe heterostructure are discussed. In order to reveal the influence of chemical shifts due to novel interface structures, the band offsets were estimated by the energy differences between Ga 3*d* and Zn 3*d* signals, and between As 3*d* and Se 3*d* signals. Those energy differences provided the quantitatively consistent results, verifying little contribution of the chemical shifts to the peak positions of the XPS signals, even if those exist. The line shapes for all photoemission signals were not changed, which also supports the above assertion. With respect to strain, on the other hand, since the GaAs/ZnSe heterostructures in this chapter are grown coherently, the effects of the compressive strain in ZnSe on the XPS profiles are completely the same as the case of ZnSe/GaAs and were neglected also in this chapter.

5.3.2 Effects of interval duration

Using Fig. 5.2, we begin by describing the effect of the interval duration (t_1) on the valence band offset. Here, the duration of the TBAs-exposure (t_2 in Fig. 5.1) was set at as short as 2 s so as not to modify the surface properties after the interval. It can clearly be seen in Fig. 5.2 that longer duration of the interval results in larger valence band offsets and that there is no significant difference between the growth temperatures. These characteristics are well explained with consideration of the surface kinetics of ZnSe during the interval.

Since ZnSe is annealed in a DMSe ambient before the interval, the ZnSe surface just after the postgrowth annealing is terminated by Se atoms. Therefore, if the interval duration is short enough to avoid Se desorption, $t_1 = 0$ s for example, the following growth of GaAs brings a mixed As-Se interface through an As-Se replacement reaction. This replacement reaction is required to attain the charge neutrality. The theoretical study, on the one hand, has predicted that the mixed As-Se interface with 50-50 composition possesses the valence band offset of 0.62 eV [2]. This value is close to the experimentally evaluated valence band

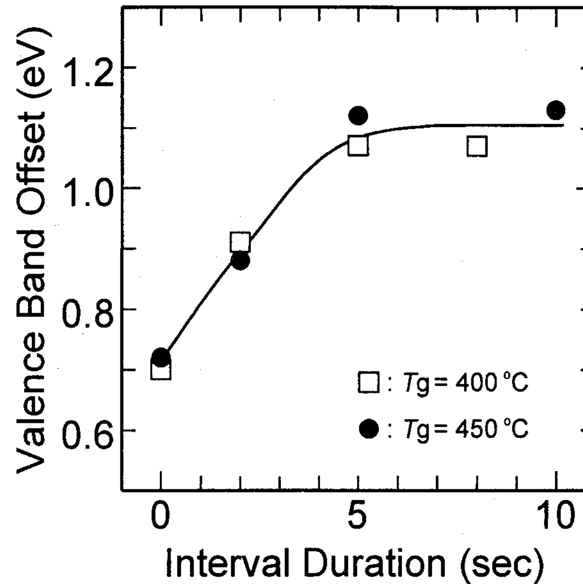

Figure 5.2: Variation of the valence band offsets as a function of the interval duration, t_1.

offset of 0.7 eV (Fig. 5.2) at $t_1 = 0$ s, which suggests that the fabricated interface consists of the mixed As-Se plane with approximately 50-50 composition. The formation of such interfaces is schematically illustrated in Fig. 5.3(a). It is seen in the figure that Ga-Se donor bonds exist at the GaAs side of the interface, while Zn-As acceptor bonds at the ZnSe side. This configuration of the bonds causes electron transfer from GaAs to ZnSe, and consequently forms dipole moments pointing toward ZnSe. With the dipole moments, the valence band offset becomes smaller than that without the interface dipoles.

The variation of the valence band offset during the interval duration between 0 and 5 s indicates that the Se composition at the interface, which was about 50% at $t_1 = 0$ s, was changed; partial desorption of surface Se atoms might take place during the interval duration, resulting in the interface Se composition less than 50%. In this case, the charge neutrality cannot be realized only by the mixture of As and Se on one anion layer and partial replacement of Zn with Ga on the cation layer underneath the mixed As-Se layer should occur. This interface is schematically shown in Fig. 5.3(b). To satisfy the charge neutrality, the number of donating Ga-Se bonds must equal the number of accepting Zn-As bonds. The Ga-Se bonds are formed not only by Ga in GaAs and interface Se, but also by Ga on the Zn plane and underlying Se. Here, the bonds between interface Se and Ga on the Zn plane are being neglected and the reason for this will be described later. From Fig. 5.3(b),

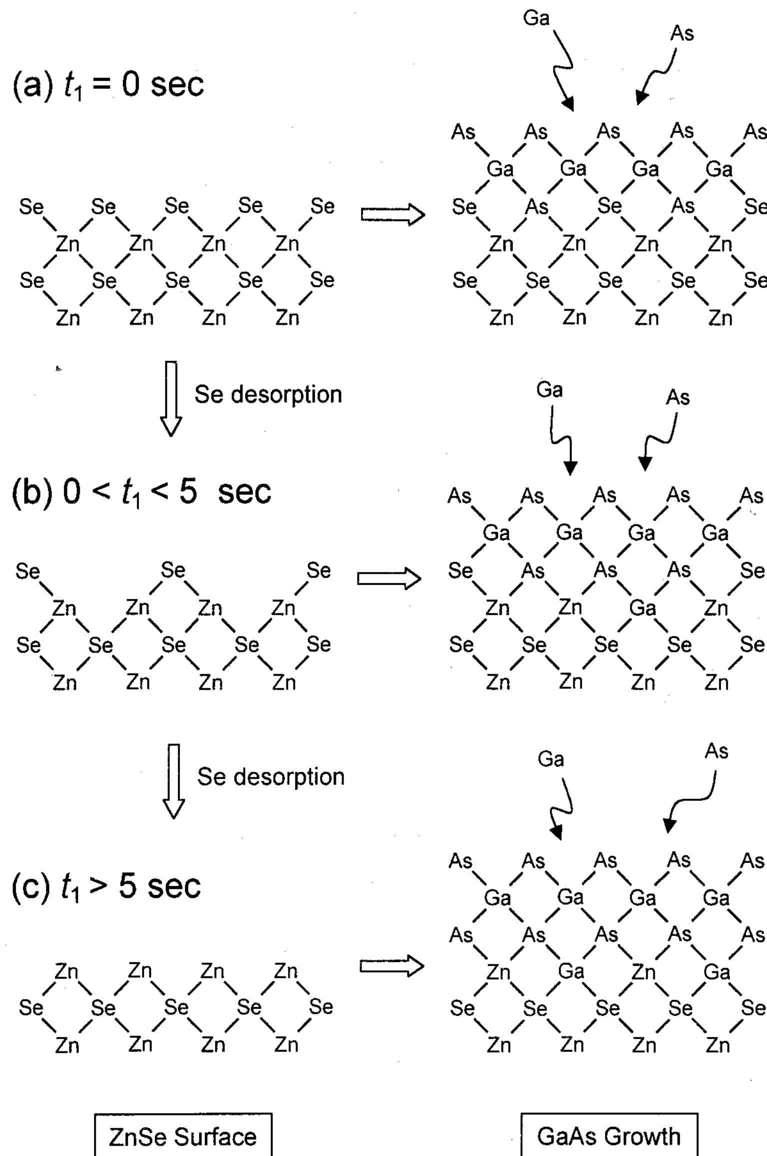

Figure 5.3: Schematic illustrations of formation of the interfaces. Variation due to the interval duration, t_1, is compared; (a) $t_1 = 0$ s, (b) $0 < t_1 < 5$ s, and (c) $t_1 > 5$ s.

it is clearly seen that an interface Se atom is bonded to two Ga atoms in GaAs and that a Ga atom on the Zn plane is bonded to two Se atoms in ZnSe. Therefore, the number of the Ga-Se bonds is calculated as twice of the sum of the number of interface Se and that of Ga on the Zn plane. On the other hand, the Zn-As bonds are formed by interface As and Zn on the Zn plane, as Fig. 5.3(b) shows. Its number is counted by considering that a Zn atom on the Zn plane is basically bonded to two interface As atoms, although the presence of an interface Se atom decreases the number of the Zn-As bonds by two. To summarize, the charge neutrality can be expressed as $2([\mathrm{Se}] + [\mathrm{Ga_{Zn}}]) = 2(1 - [\mathrm{Ga_{Zn}}]) - 2[\mathrm{Se}]$, that is,

$$2[\mathrm{Se}] + 2[\mathrm{Ga_{Zn}}] = 1, \tag{5.1}$$

where [Se] and $[\mathrm{Ga_{Zn}}]$ are the fractional occupancies of Se at the interface and Ga on the Zn plane, respectively [8]. This equation means that, if [Se] is 50%, *i.e.*, $t_1 = 0$ s, there are no Ga atoms on the Zn plane and that the desorption of Se atoms during the interval between 0 and 5 s introduces the same number of Ga atoms onto the Zn plane [Fig. 5.3(b)]. As the number of Se atoms at the interface reduces, the number of the Ga-Se donor bonds at the GaAs side decreases, which weakens the strength of the dipoles and, finally, turns its direction. This change of the strength and direction of the dipoles results in the increase of the valence band offset toward 1.1 eV.

In the above calculation, the presence of the bonds between interface Se and Ga on the Zn plane was neglected. This is because these bonds do not influence the condition for the charge neutrality written by Eq. (5.1). If an interface Se atom makes a bond with a Ga atom on the Zn plane, the number of the Zn-Se bonds at the interface is reduced by one, and a Zn-As bond, which is formed by interface As and Zn on the Zn plane, is induced. As a result, the charge neutrality is preserved. Therefore, Eq. (5.1) was derived with an assumption of the absence of the interface Ga-Se bonds, although actually it can be applied for any interfaces with two mixed atomic layers where atomic configuration is arbitrary.

The interval longer than 5 s, on the other hand, did not influence the valence band offsets, as shown in Fig. 5.2. This is presumably because Se atoms originally being on the ZnSe surface were desorbed completely at the interval duration of 5 s and the surface was terminated by Zn atoms. Since the Zn-terminated surface is more stable owing to the lower vapor pressure of Zn atoms, it is maintained even after the interval longer than 5 s. Since

this situation corresponds to [Se] = 0 in Eq. (5.1), the growth of GaAs on this ZnSe surface results in a mixed Ga-Zn interface with 50-50 composition as schematically illustrated in Fig. 5.3(c). It is obviously seen that the Zn-As bonds are induced at the GaAs side of the interface and that the Ga-Se bonds at the ZnSe side. This bond configuration transfers electrons from ZnSe to GaAs, which is the inverse direction of the electron transfer in the GaAs/Se-terminated ZnSe interface. Therefore, the resultant dipoles are in the inverse direction and the valence band offsets become as large as about 1.1 eV.

In the theoretical analysis, the interface shown in Fig. 5.3(c) has been predicted to possess the valence band offset of 1.59 eV [2]. Although the experimental results obtained in this study differ from the theoretical calculation, the reason for this discrepancy has never been clarified. The variation of the valence band offsets experimentally achieved in chapters 3 and 5, and Ref. [2] ranges from 0.6 to 1.1 eV consistently, implying that there is room for reconsideration in theoretical studies. From the experimental point of view, on the other hand, the discrepancy implies that the interfaces in the present heterostructures are basically close to the simplified model shown in Fig. 5.3(c), but may be modified, for example, by interdiffusion to some extent. In this sense, investigations on the interface atomic configuration in the atomic level will be very crucial.

As was pointed out previously, the behavior of the valence band offsets against the interval duration (t_1) does not depend on the growth temperature, indicating that the rate of the Se desorption from the top surface of ZnSe in the hydrogen ambient is independent of temperatures between 400 and 450°C. The Se desorption from ZnSe occurs through decomposition and evaporation, and its rate is determined by competition between the decomposition and the evaporation rates. Since the vapor pressure of elemental Se is a function of temperature as is well known, the evaporation rate depends on temperature, which does not fit the experimental results. Therefore, the present results are probably governed by the decomposition of Se from ZnSe.

5.3.3 Effects of As exposure duration

We will move to discussion about a role of the duration of the TBAs-exposure (t_2 in Fig. 5.1) in controllability of the valence band offset. The interval duration, t_1, was kept at 5 s, and thus the ZnSe surface before being exposed to TBAs is covered with Zn as verified by Fig. 5.2. Figure 5.4 illustrates variation of the valence band offsets in the

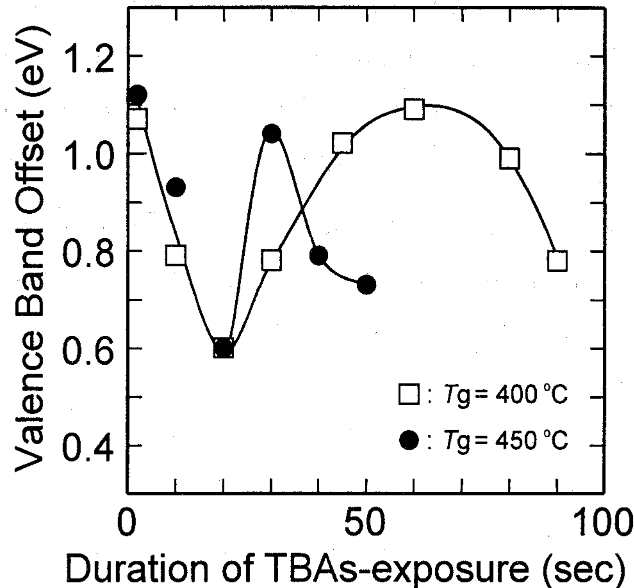

Figure 5.4: Variation of the valence band offsets as a function of the duration of the TBAs-exposure, t_2.

GaAs/ZnSe heterostructures grown at 400 and 450°C as a function of the duration of the TBAs-exposure. As the duration lengthens, the valence band offsets change periodically between 1.1 and 0.6 eV. The amplitudes of the change do not depend on the growth temperatures, whereas the periods do, that is, the higher growth temperature led to the shorter period. For $T_g = 450°C$, the amplitude of the variation seems to be slightly smaller in the second period ($t_2 > 30$ s) and the mechanism for this will be discussed later.

The phenomenon in Fig. 5.4 can be interpreted as follows. In the case of $t_2 = 0$ s, the ZnSe surface prior to the GaAs growth is terminated by Zn atoms. The decrease of the valence band offsets with the increase of t_2 is probably due to a reaction between TBAs and the surface Zn atoms which synthesizes a volatile compound of Zn_3As_2 [9]. Since the compound Zn_3As_2 is rapidly desorbed above 360°C [9], the ZnSe surface and, therefore, the interface tend to be Se-rich. The increase of Se atoms at the interface decreases the valence band offset through the same mechanism described in the discussion with Figs. 5.2 and 5.3. The valence band offsets for both growth temperatures reach the smallest value of 0.6 eV simultaneously when t_2 is 20 s, indicating that the formation and evaporation processes of Zn_3As_2 are independent of temperatures around 400 – 450°C. Compared with the theoretical study [2], the smallest value of 0.6 eV suggests that the interface is the mixed As-Se plane with approximately 50-50 composition. It is probable that, at $t_2 = 20$ s,

the evaporation of Zn_3As_2 is completed and that the ZnSe surface is almost fully covered with Se atoms. Therefore, the following growth of GaAs induces partial replacement of Se by As and results in the mixed As-Se interface in order to satisfy the charge neutrality. This interface structure is similar to that obtained by $t_1 = 0$ s in Fig. 5.2.

For duration longer than 20 s, the valence band offsets increased toward 1.1 eV, suggesting the desorption of the surface Se atoms during the TBAs-exposure. The duration at which the valence band offsets reach 1.1 eV is different for the different growth temperatures, that is, 30 s for $T_g = 450°C$ and about 60 s for $T_g = 400°C$. This means that the Se desorption strongly depends on the temperature. In Fig. 5.2, on the other hand, the Se desorption was not influenced by the growth temperature and it took about 5 s to complete the desorption of a Se atomic layer. The striking difference between these two experiments is the ambient to which the ZnSe surface was subjected; ZnSe was exposed to hydrogen in Fig. 5.2, while to the TBAs ambient in Fig. 5.4. Therefore, we consider at present that some reaction between Se on the ZnSe surface and As in the ambient modifies the condition for the desorption of the Se atoms. Since As can make a bond with Se to form an As_xSe_{1-x} compound, as is often reported [10, 11], this compound is one of the possible origins preventing the desorption of the Se atoms. After reaching 1.1 eV, the valence band offsets decreased again, indicating the occurrence of the formation and evaporation of Zn_3As_2.

The observed variation of the valence band offsets suggests that, regarding a few surface atomic layers, the etching of ZnSe by TBAs is in the layer-by-layer mode. It has been revealed, however, that the ZnSe etched by TBAs to a few tens of nanometers exhibited rough surfaces (chapter 4). Therefore, the tendency of digital etching will be weakened and the periodic change of the valence band offset will be attenuated by longer duration of the TBAs-exposure. It is seen in Fig. 5.4 that, when the growth temperature is 450°C, the amplitude of the second period becomes slightly smaller than that of the first period. This may be a sign of the degradation of the digital etching properties.

The periods of the variation of the valence band offsets derived from Fig. 5.4 were 30 and 60 s for $T_g = 450$ and 400°C, respectively. The period of 60 s for $T_g = 400°C$ is not highly reliable because the change is slow and it is difficult to determine the peak position precisely. According to our model, one period should correspond to the etching of 1 ML (2.8 Å) and, therefore, the etching rates can be calculated from the periods. These were

5.6 and 2.8 Å/min for T_g = 450 and 400°C, respectively. On the other hand, using the results of the etching study in the previous chapter, the etching rates at 450 and 400°C are estimated to be 6 and 1 Å/min, respectively. For T_g = 450°C, these values agree reasonably well, supporting the hypothesis that the variation of the valence band offsets observed in this chapter originates from alternate appearances of Zn and Se atoms on the ZnSe surface through the digital etching. However, one may feel that the difference between the etching rate of 2.8 Å/min at 400°C in this chapter and 1 Å/min in the previous chapter is large. In chapter 4, ZnSe was etched by a few tens of nanometers and the etched depth was measured by ellipsometry. After the etching to such a depth, the ZnSe surfaces become rough as mentioned in the above paragraph, and therefore the accuracy of the rate determined in that chapter is not so high. Furthermore, as described above, the etching rate of 2.8 Å/min obtained here as well is not highly reliable owing to the uncertain peak position in Fig. 5.4. These facts may cause the difference in the estimation of the etching rates and we consider that this difference is within the experimental error.

5.4 Summary

Tunability of the band offsets in GaAs/ZnSe(001) heterovalent heterostructures was successfully demonstrated, while the surface of GaAs grown on ZnSe was kept atomically flat to ensure the formation of the abrupt interface. By changing the exposure duration of ZnSe to the hydrogen ambient and to the TBAs ambient, the variation of the valence band offset from 0.6 to 1.1 eV was achieved. The mechanism behind it was ascribed to the layer-by-layer fashion of the thermal etching in these ambients.

We have already attained the control of the band offsets in the ZnSe/GaAs heterostructures. Therefore, the results in this chapter open a way to fabricate ZnSe-GaAs multilayered structures with the engineered properties.

References

[1] L. A. Hemstreet, C. Y. Fong, and J. S. Nelson, J. Vac. Sci. Technol. B **11**, 1693 (1993).

[2] R. Nicolini, L. Vanzetti, G. Mula, G. Bratina, L. Sorba, A. Franciosi, M. Peressi, S. Baroni, R. Resta, A. Baldereschi, J. E. Angelo, and W. W. Gerrich, Phys. Rev. Lett. **72**, 294 (1994).

[3] A. Kley and J. Neugebauer, Phys. Rev. B **50**, 8616 (1994).

[4] R. G. Dandrea, S. Froyen, and A. Zunger, Phys. Rev. B **42**, 3213 (1990).

[5] K. Kunc and R. M. Martin, Phys. Rev. B **24**, 3445 (1981).

[6] G. Bratina, L. Vanzetti, A. Bonanni, L. Sorba, J. J. Paggel, A. Franciosi, T. Peluso, and L. Tapfer, J. Crystal Growth **159**, 703 (1996).

[7] R. W. Grant, J. R. Waldrop, S. P. Kowalczyk, and E. A. Kraut, J. Vac. Sci. Technol. B **3**, 1295 (1985).

[8] The procedure adopted here to extract Eq. (5.1) is the very same as that of the electron counting model. Regarding the electron counting model, see, for example, M. D. Pashley, Phys. Rev. B **40**, 10481 (1989).

[9] B. Chelluri, T. Y. Chang, A. Ourmazd, A. H. Dayem, J. L. Zyskind, and A. Srivastava, Appl. Phys. Lett. **49**, 1665 (1986).

[10] V. Mastelaro, H. Dexpert, S. Benazeth, and R. Ollitrault-Fichet, J. Solid State Chem. **96**, 301 (1992).

[11] S. R. Elliott and A. V. Kolobov, Philos. Mag. B **61**, 853 (1990).

Chapter 6

Quantum Structures with Engineered Interface Properties

6.1 Introduction

We have demonstrated the capability of controlling the band offsets in the ZnSe-on-GaAs(001) [ZnSe/GaAs(001)] (chapter 3) and the GaAs-on-ZnSe(001) [GaAs/ZnSe(001)] heterostructures (chapter 5) through the interface engineering; the valence band offsets could be tuned from 0.6 to 1.1 eV by manipulating the interfacial atomic configuration through the precise control of the flow sequence of the source precursors at the interfaces. These results opened a way to fabricate various multilayered structures from the ZnSe-GaAs system. For example, the offset divided into both the valence and the conduction bands may lead to formation of quantum structures, while, if the offset is put mainly on either the valence or the conduction band, double heterojunction bipolar or phototransistors with high injection efficiency can be realized.

In this chapter, we fabricate ZnSe-GaAs heterovalent quantum structures in which the band offsets at both sides of the GaAs wells are independently designed, and characterize their properties chiefly originating from heterovalency. The fabricated structures are mostly multiple quantum wells (MQW's) and partially superlattices. When the band offsets at both sides of GaAs are different, the quantum structures should contain an electric field. Since the intensity of the electric field is changeable via control of the band offsets, the properties of the quantum structures are variable as well. So far, the effects of electric fields on the nature of the eigenstates have been investigated using the conventional isovalent quantum structures such as a GaAs-AlGaAs system. If each well in a quantum

structure is sufficiently isolated, which is the situation in a QW structure, the energy gaps will be shifted toward lower energy by the electric field [1]. In the case of superlattices, the electric field causes Wannier-Stark localization [2]. In these studies, however, the electric field was applied externally, for example, by pin and nin structures. On the other hand, a characteristic of the heterovalent quantum structures is that a new parameter of the band offset for designing the electronic properties enables the electric field to be included internally. Furthermore, since the tunability of the offsets depends on the interface dipoles being a function of the interfacial charge distribution, structures that rearrange the charge distribution may also alter the electronic properties. In this chapter, we investigate dependence of the energy states in the ZnSe-GaAs heterovalent quantum structures, which include the *intrinsic* electric field, on the offsets, the well width, and the barrier width to provide an insight into their basic properties. The experimental results obtained by optical-absorption measurement at 22 K are compared with the results of the theoretical analyses using the Poisson and Schrödinger equations.

6.2 Fabrication of ZnSe-GaAs Quantum Structures

determination of growth temperature

The results of chapters 2 and 4 suggest that the growth temperatures (T_g) of the quantum structure should be 450°C. To confirm this, 30 periods of ZnSe (116 Å) / GaAs (45 Å) MQW's were fabricated at 450 and 500°C, and their structural properties were compared by means of double-crystal x-ray diffraction (XRD) using Cu $K\alpha_1$ (1.5405 Å) radiation as an x-ray source. The XRD profiles taken in the vicinity of the GaAs 004 diffraction are shown in Fig. 6.1 together with the theoretical calculation based on the kinematical theory. The full-width at half maximum (FWHM) of the fundamental peak is 38 arcsec for both profiles and this corresponds well to the theoretical value of 35 arcsec, indicating the excellent crystalline properties. However, difference due to T_g is found in the peak intensity. The XRD pattern of the MQW grown at 450°C agrees well with the theoretical curve, while intensity of the satellite peaks in the XRD pattern of the MQW grown at 500°C is weaker. Possible reasons for this are indistinct interfaces and thickness fluctuations from period to period. However, a perturbation of the period will also cause broadening of the width, which does not fit the experimental result. Therefore, the higher

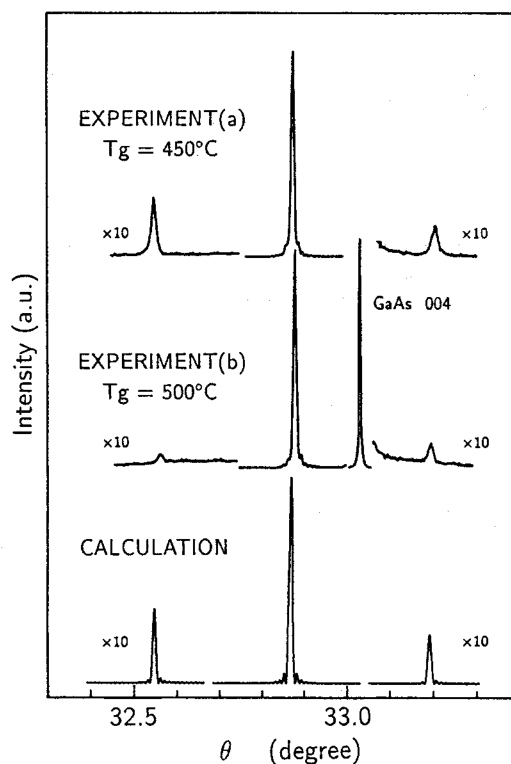

Figure 6.1: The experimental and the calculated XRD patterns of MQW's with the 30 periods of ZnSe (116 Å) / GaAs (45 Å). Variation due to T_g is shown.

temperature growth is thought to have degraded the interface abruptness. From these findings, we can conclude that the growth temperature of 450°C is a desirable temperature to obtain quantum structures with superior structural properties.

the state of the art of the present MOVPE

Before describing the growth procedure of the samples for the optical-absorption measurements, we attempt to reveal the ability of the present metalorganic vapor phase epitaxy (MOVPE) system in fabricating the quantum structures. An interest here is how thin the constituent layers can be made.

The 20 periods MQW with 140-Å-thick ZnSe and 25-Å-thick GaAs was grown at 450°C. The measured double-crystal XRD profile as well as the theoretical calculation is shown in Fig. 6.2. Intense and well-defined satellite peaks can be detected. The relative scattering intensity of the satellite peaks against the fundamental peak and FWHM of 51 arcsec are equivalent to those derived from the simulation. The MQW possesses the high

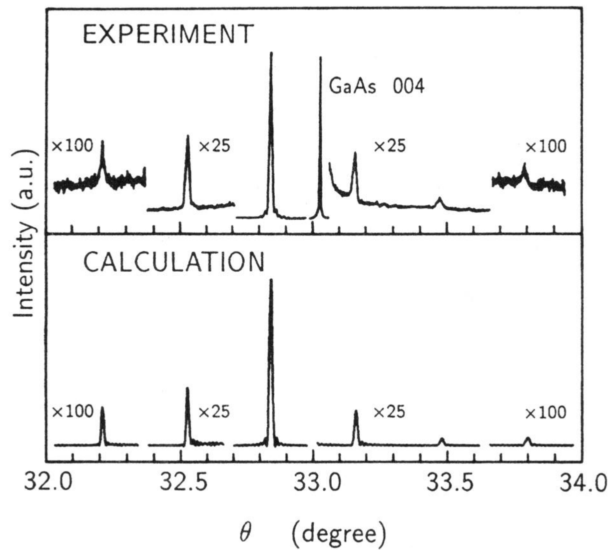

Figure 6.2: Double-crystal XRD pattern of MQW with 20 periods of ZnSe (140 Å) / GaAs (25 Å). The upper and the lower figures are the experimental and the calculated results, respectively.

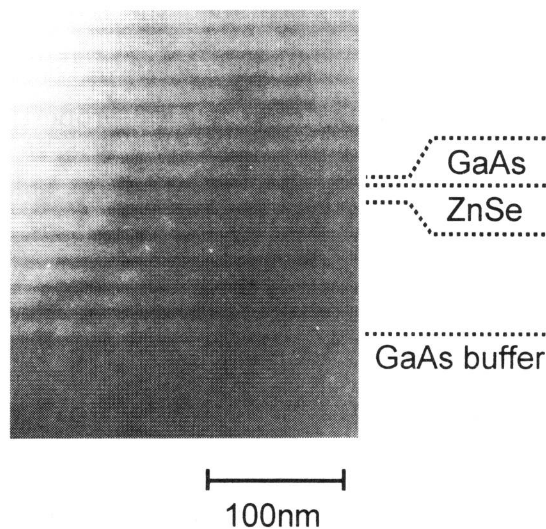

Figure 6.3: Cross-sectional TEM bright field image of the same MQW shown in the previous figure.

crystalline quality and well-defined interfaces. Figure 6.3 is a transmission electron microscope (TEM) bright field image of the (110) cross section of the same MQW. The direct observation by TEM also indicates the successful fabrication of the ZnSe-GaAs MQW. Evidence of abrupt compositional modulation is given by the marked contrast between bright ZnSe and dark GaAs; though the well layer is as thin as 25 Å. Neither threading dislocations nor stacking faults are observed over the entire area, indicating that the lattice mismatch strain is accommodated elastically and that the sample has good crystalline quality. The layer thickness of each material is almost constant from bottom to top [3]. These findings confirm the high degree of the structural quality of this MQW.

A next quantum structure has much thinner ZnSe barrier layers; 100 periods of ZnSe (33 Å) / GaAs (25 Å). It should be noted that these well and barrier widths are the thinnest ever achieved in this material system. The ZnSe layer thickness is thin enough to give rise to interaction of the wave function in each well, and therefore, this quantum structure is a so-called superlattice. Successful construction was confirmed by comparing the experimental XRD pattern with the theoretical calculation, as shown in Fig. 6.4. FWHM of the fundamental peak is 31 arcsec, which proves its good crystalline quality. However, two satellite peaks are broadened and slightly weakened, compared with the theoretical profile.

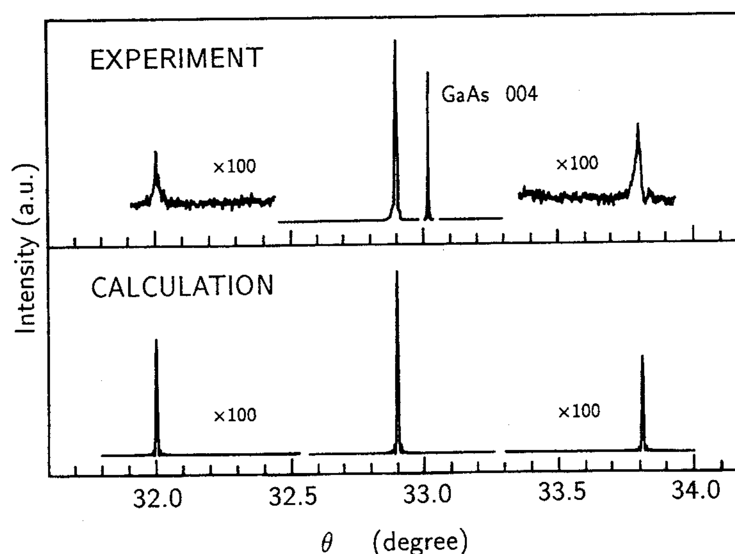

Figure 6.4: Double-crystal XRD pattern of the 100 periods superlattice with ZnSe (33 Å) / GaAs (25 Å).

By decreasing the ZnSe layer thickness from 140 Å (in the MQW mentioned above) to 33 Å, the periodicity was degraded, for example, by thickness fluctuations and/or indistinct interfaces. This result suggests that in the present MOVPE, the lowest limit of the constituent layer thickness in the ZnSe-GaAs quantum structures is larger for ZnSe and that is a few tens of angstrom.

quantum structures for optical-absorption measurements

The sample structure for the optical-absorption measurements is schematically shown in Fig. 6.5. Growth of the samples was initiated by a 1500-Å-thick GaAs buffer layer at 700°C. To obtain an atomically flat surface, post-growth annealing was conducted at 700°C for 10 min in a tertiarybutylarsine (TBAs) ambient. Next a 500-Å-thick ZnSe region was grown at 450°C primarily to act as an etch stop layer for substrate removal. Finally, a ZnSe-GaAs quantum structure was grown at 450°C. The period of the quantum structure was designed so as to make the total thickness of the GaAs wells 600 – 800 Å. The detailed growth conditions are found in chapters 2 and 4. The valence band offsets at both ZnSe/GaAs and GaAs/ZnSe heterointerfaces are controllable. In this study, however, to simplify the discussion, the former was kept constant at 0.6 eV for all samples, while the

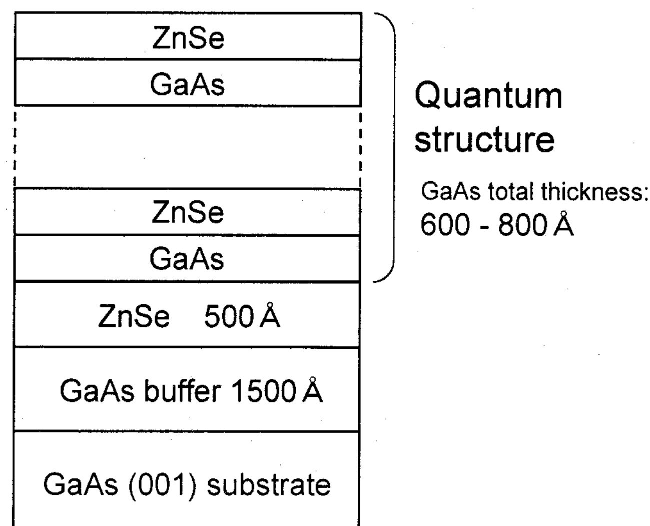

Figure 6.5: Schematic diagram of the ZnSe-GaAs quantum structures fabricated for the optical-absorption measurements.

latter was changed between 0.6 and 1.1 eV. For this control of the band offset, the interval duration between the ZnSe and GaAs growth, during which only hydrogen was supplied for purging the ZnSe source precursors, was set at 5 s, and the GaAs growth was initiated after the exposure of ZnSe to TBAs for 2 – 20 s (see chapter 5 for more details). The influence of this artificial control of the band offsets on the electronic states was assessed by optical-absorption measurement at 22 K.

6.3 Structural Properties

In order to extract differences of the optical properties due to the interface engineering, it is important to clarify the structural properties, because the structural properties may also contribute to the modification of the optical properties of the quantum structures. For this purpose, the surface morphology and the crystallinity were investigated by means of atomic force microscopy (AFM) and XRD, respectively.

6.3.1 Surface morphology

The AFM observation was carried out in air immediately after the growth. There was no evident difference associated with the interface control, and the surfaces for all samples exhibited atomically flat terraces and monolayer steps (2.8 Å in height) as shown in Fig. 6.6. This result suggests that, regardless of the manner to prepare the interfaces, the growths of both ZnSe/GaAs and GaAs/ZnSe are in the two-dimensional growth mode under the conditions employed here and that the interfaces are abrupt.

6.3.2 Crystalline properties

The XRD patterns were taken in the vicinity of the GaAs 004 diffraction. Figure 6.7 shows an example of the XRD profiles, in which both the experimental and the simulated profiles are illustrated. The sample, in this particular case, is the eight periods MQW with the expected dimensions of 110 Å for ZnSe and 100 Å for GaAs. The dimensions evaluated from the comparison between the experimental result and the simulation based on the dynamical diffraction theory were 107 Å for ZnSe and 99 Å for GaAs, which are very close to the designed parameters. In the experimental profile, in addition to a fundamental peak ($n = 0$), well-defined satellite peaks labeled $n = \pm 1$ are clearly detected. The peak intensity

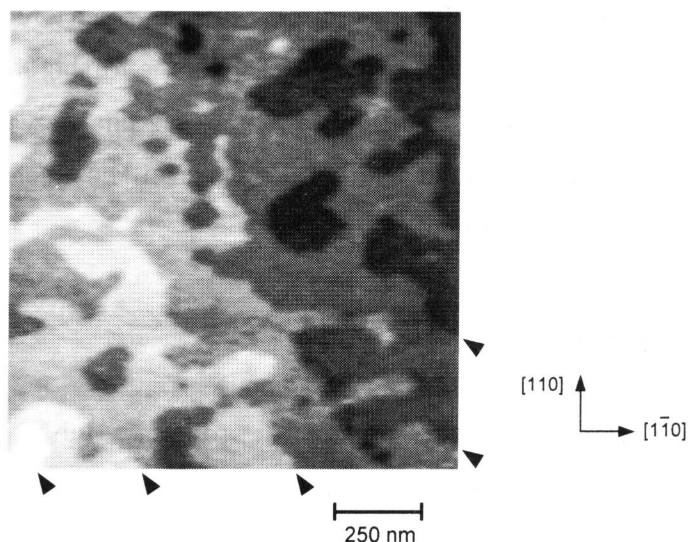

Figure 6.6: Typical AFM image of the surface of the ZnSe-GaAs quantum structures. Arrowheads indicate 1 monolayer steps (2.8 Å in height).

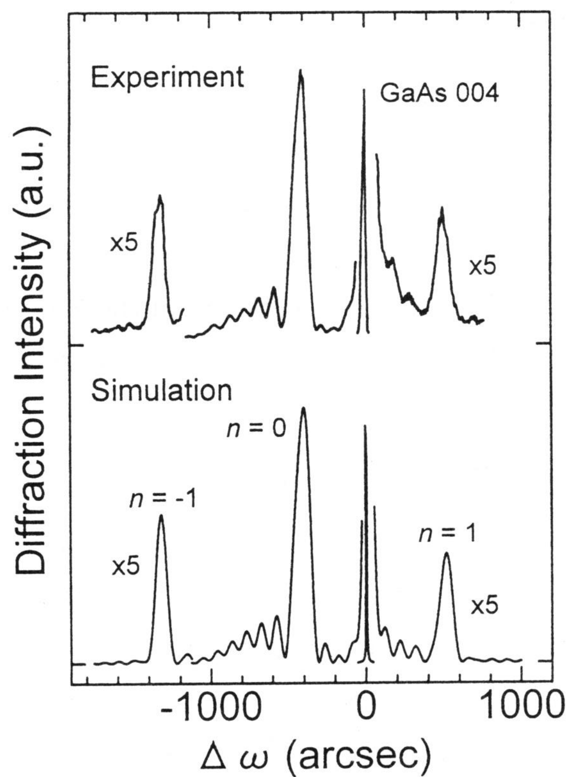

Figure 6.7: An example of the XRD profiles of the ZnSe-GaAs quantum structures. The agreement between the experimental result and the theoretically calculated profile indicates the high degree of the structural perfectness.

ratios between the satellite and the fundamental peaks and FWHM agree quite well with those derived from the dynamical simulation, indicating the high crystalline quality, high periodicity, and high interface abruptness in the ZnSe-GaAs quantum structure. The 500-Å-thick ZnSe etch stop layer, on the other hand, increases the diffraction intensity between −1000 and −500 arcsec, for which the calculation again does agree with the experiment. In the simulation, ZnSe was assumed to be deformed so as to maintain full coherence, and the correspondence with the experimental result supports this assumption. The entire region of the quantum structure is grown coherently on the GaAs substrate with few dislocations. It should be emphasized that fairly good agreement between experiment and simulation was confirmed for all samples, which allows us to interpret the observed optical properties without caring about structural imperfections.

6.4 Optical-Absorption Properties

6.4.1 Theoretical backgrounds

The electronic properties of a quantum structure with an electric field are described by the one-dimensional Poisson equation for the electrostatic potential $\phi(z)$

$$\epsilon_{\mathrm{s}} \frac{\mathrm{d}^2\phi(z)}{\mathrm{d}z^2} = e[-n(z) + p(z) + N_{\mathrm{D}}^{+}(z) - N_{\mathrm{A}}^{-}(z)] \tag{6.1}$$

and the Schrödinger equation for an eigenvalue E

$$-\frac{\hbar^2}{2m^*}\frac{\mathrm{d}^2\psi(z)}{\mathrm{d}z^2} + V(z)\psi(z) = E\psi(z), \tag{6.2}$$

where ϵ_{s} is the dielectric constant, $n(z), p(z), N_{\mathrm{D}}^{+}(z)$, and $N_{\mathrm{A}}^{-}(z)$ are the density of electrons, holes, ionized donors, and ionized acceptors, respectively, m^* is the effective mass, and $\psi(z)$ is the wave function. The potential-energy $V(z)$ in the Schrödinger equation is related to the electrostatic potential by $V(z) = -e\phi(z) + V_{\mathrm{h}}(z)$, where $V_{\mathrm{h}}(z)$ is a step function which accounts for heterojunction discontinuities and is an important parameter in this study.

Strictly, these equations should be solved self-consistently; though for simplicity, the following approximation has been made. The quantum confinement effect was not considered in the Poisson equation, and the carrier concentrations were written in classical formulations, using the Ehrenberg approximation [4], as

$$n(z) = \frac{N_{\mathrm{c}}}{1/4 + \exp\{-[E_{\mathrm{f}} - E_{\mathrm{c}}(z)]/k_{\mathrm{B}}T\}} \tag{6.3}$$

Table 6.1: Physical parameters used for the calculation of the Poisson and Schrödinger equations.

	Dielectric constant	Effective mass (m^*/m_0)	
	(ϵ_s/ϵ_0)	electron	hole[A]
GaAs	12.9[a]	0.067[b]	0.475[c]
ZnSe	9.14[d]	0.16[d]	0.78[e]

[A] Quantities shown are the heavy hole masses along $\langle 001 \rangle$.
[a] Reference [5]
[b] Reference [6]
[c] Reference [7]
[d] Reference [8]
[e] Reference [9]

and

$$p(z) = \frac{N_v}{1/4 + \exp\{-[E_v(z) - E_f]/k_B T\}}, \tag{6.4}$$

where N_c and N_v are the effective density of states for the conduction and the valence bands, respectively, E_f, E_c, and E_v are the energies of the Fermi level, the conduction band, and the valence band, respectively, k_B is the Bolzmann constant, and T is the absolute temperature. Within the limits of this classical approximation, the potential-energy profiles are uniquely determined only by the Poisson equation. Therefore, eigenstates are, then, calculated by solving the Schrödinger equation, where carriers experience the potential profile derived from the Poisson equation. Although this procedure is not self-consistent and may degrade quantitative accuracy, the included error does not seem to be serious owing to the following reasons. If the well width is thick, the classical density of states well approximates that with the quantum effect. Thin wells, on the other hand, induce the substantial difference in the density of states, although the electric field, in turn, does not influence eigenstates remarkably. Therefore, the electronic properties of the heterovalent quantum structures can be outlined by the procedure adopted here with relative easiness.

The physical parameters used for the calculation were listed in Table 6.1.

potential-energy profiles

Since the samples fabricated in this study are multilayered quantum structures, the Poisson equation was solved with the periodic boundary conditions. Figure 6.8 shows some of the calculated potential profiles of the MQW's. The dimensions of the GaAs wells and the

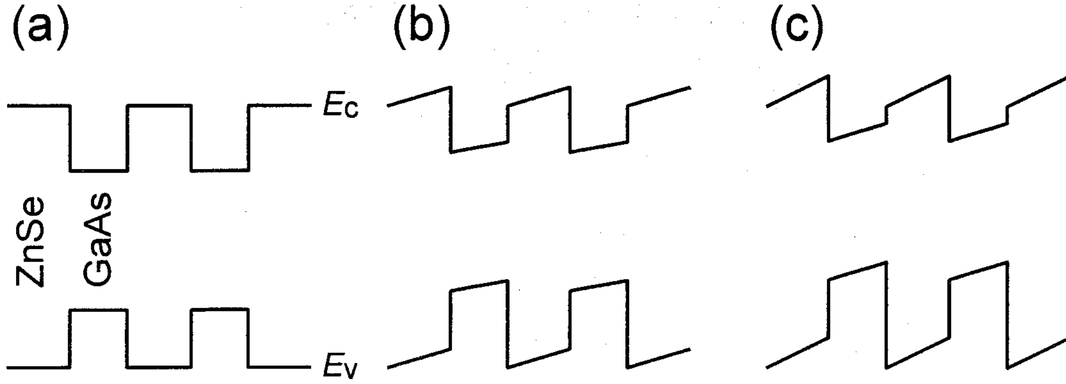

Figure 6.8: Calculated potential profiles of the ZnSe-GaAs heterovalent MQW's with different pairs of the valence band offsets at both sides of GaAs; (a) 0.6/0.6 eV, (b) 0.6/0.9 eV, and (c) 0.6/1.1 eV. The ZnSe and GaAs layers are 110- and 100-Å thick, respectively. E_c and E_v indicate the conduction and the valence band, respectively.

ZnSe barriers are 100 and 110 Å, respectively. The pairs of the valence band offsets at both sides of the GaAs wells are (a) 0.6/0.6, (b) 0.6/0.9, and (c) 0.6/1.1 eV. These structural and physical parameters were chosen, referring to the actually fabricated structures. Here, ZnSe is assumed to be n-type with a donor concentration of 1×10^{11} cm^{-3}, while GaAs is p-type with 5×10^{17} cm^{-3}. These quantities are the experimental results obtained from Hall-effect measurements of thick layers but are not essential, as will be shown later. It is obvious from Fig. 6.8 that the electric field, which corresponds to the inclination of the potential profile, becomes stronger by the increase of the difference in the valence band offsets and that its intensity is approximately uniform in either the ZnSe or the GaAs region.

Based on Fig. 6.8, the average electric fields in the well and the barrier regions were estimated on the assumption that the electric field was uniform in each region. The results are shown in Fig. 6.9, where the valence band offset ΔE_v at one side of GaAs is always 0.6 eV and that at the other side is a variable designated at the horizontal axis. That shown at the upper horizontal axis is the conduction band offset ΔE_c at the same interface where the valence band offset is a variable. The conduction band offset is given by $\Delta E_c = E_g^{ZnSe} - E_g^{GaAs} - \Delta E_v$ with the energy gap E_g. Variation due to the well width is also compared. The intensities of the electric fields are almost proportional to the difference in the valence band offsets and are stronger in MQW's with narrower wells.

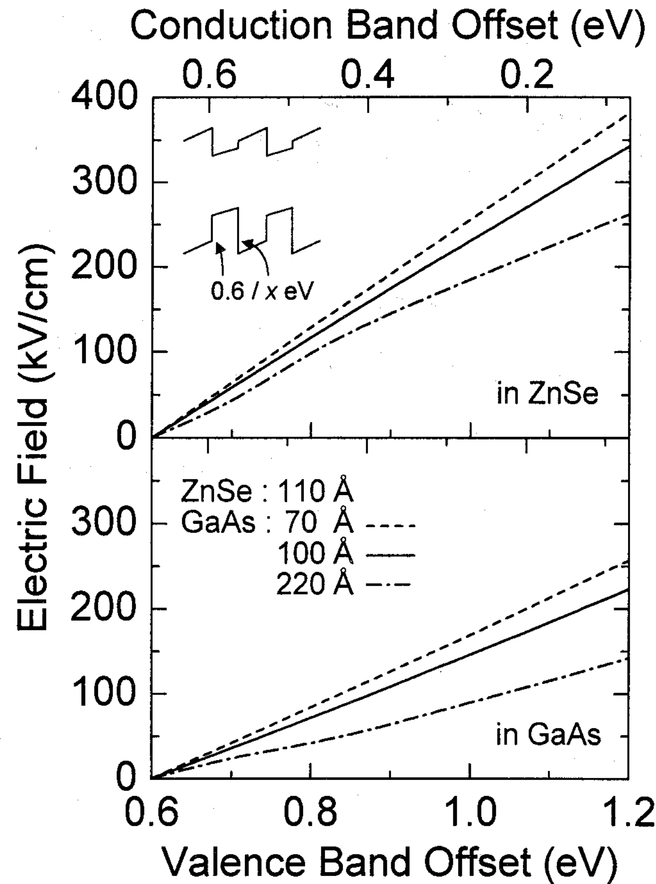

Figure 6.9: Estimated electric fields in ZnSe and GaAs. The dimension of ZnSe is 110 Å and that of GaAs is a parameter. The valence band offset at one side of GaAs is 0.6 eV and that at the other side is a variable shown at the horizontal axis.

As is well known, impurity concentration often influences the potential profile of semiconductor heterojunctions. Surprisingly, however, it was found that the potential profiles of the heterovalent quantum structures hardly depended on the impurity concentration and that those were mainly determined by the difference of the valence band offsets at both sides of the GaAs wells. For example, when the valence band offsets at both interfaces are 0.6 and 1.1 eV, difference of the acceptor concentrations in GaAs of 1×10^{14} and 5×10^{17} cm^{-3} resulted in only a few percent variation of the electric fields, that is, 195 kV/cm and 184 kV/cm in GaAs, respectively. Furthermore, p- and n-GaAs with the same impurity concentration of 5×10^{17} cm^{-3} exhibited the almost identical potential profiles; electric fields in GaAs were 184 kV/cm for p-GaAs, while 183 kV/cm for n-GaAs. The similar tendency was observed by changing the impurity concentration in ZnSe. The

reason for this independence on the impurity concentration is that the potential inclination due to the difference in the valence band offsets is remarkably greater than that induced by donor and acceptor impurities and determines the potential profiles predominantly.

energy eigenstates

Under the presence of the electric field revealed by the Poisson equation, the Schrödinger equation was solved by the variational method [10] to estimate the energy eigenstates. A single QW with ZnSe barriers of infinite width was used as a model for the calculation. This approximation is valid for most of the present quantum structures, because their barrier width is typically about 110 Å and the penetration of the calculated wave function into the ZnSe barrier regions was totally within about 100 Å. Namely, these are MQW's, in which the wave function in each well is thoroughly isolated and hardly interacts with one another.

In the variational calculation, the Schrödinger equation without an electric field, that is, with constant energy potential V_0, is first considered. Suppose the well width is L, and the wave function $\psi_0(z)$ is obtained as

$$\psi_0(z) = \begin{cases} Ae^{k_{\mathrm{ZnSe}}z} & \text{for} \quad z \leq 0 \\ A\dfrac{\sqrt{k_{\mathrm{GaAs}}^2 + (Rk_{\mathrm{ZnSe}})^2}}{k_{\mathrm{GaAs}}}\sin(k_{\mathrm{GaAs}}z + \delta) & \text{for} \quad 0 \leq z \leq L, \\ Ae^{k_{\mathrm{ZnSe}}(L-z)} & \text{for} \quad L \leq z \end{cases} \tag{6.5}$$

with

$$k_{\mathrm{GaAs}} = \frac{\sqrt{2m_{\mathrm{GaAs}}^* E}}{\hbar}, \quad k_{\mathrm{ZnSe}} = \frac{\sqrt{2m_{\mathrm{ZnSe}}^*(V_0 - E)}}{\hbar},$$
$$\delta = \tan^{-1}\frac{k_{\mathrm{GaAs}}}{Rk_{\mathrm{ZnSe}}}, \text{ and } R = \frac{m_{\mathrm{GaAs}}^*}{m_{\mathrm{ZnSe}}^*}. \tag{6.6}$$

The used boundary conditions are $\psi_{\mathrm{GaAs}} = \psi_{\mathrm{ZnSe}}$ and ${m_{\mathrm{GaAs}}^*}^{-1}(\mathrm{d}\psi_{\mathrm{GaAs}}/\mathrm{d}z) = {m_{\mathrm{ZnSe}}^*}^{-1}(\mathrm{d}\psi_{\mathrm{ZnSe}}/\mathrm{d}z)$ at the interfaces ($z = 0$ and $z = L$).

Under electric fields, the wave function is approximated by the product of that without electric fields [Eq. (6.5)] and the following variational wave function, which is basically the same as those in Ref. [10], though was modified to satisfy the boundary conditions

mentioned above:

$$f(\beta, z) = \begin{cases} \exp\left[-\beta\left(\frac{z}{RL} - \frac{1}{2}\right)\right] & \text{for} \quad z \leq 0 \\ \exp\left[-\beta\left(\frac{z}{L} - \frac{1}{2}\right)\right] & \text{for} \quad 0 \leq z \leq L. \\ \exp\left[-\beta\left(\frac{z-L}{RL} - \frac{1}{2}\right)\right] & \text{for} \quad L \leq z \end{cases} \quad (6.7)$$

The energy eigenvalue is determined by minimizing

$$E = \frac{< \psi_0(z) f(\beta, z) | H | \psi_0(z) f(\beta, z) >}{< \psi_0(z) f(\beta, z) | \psi_0(z) f(\beta, z) >} \quad (6.8)$$

in terms of the variational parameter β. In the equation, H is the Hamiltonian of the problem and is expressed as $-(\hbar^2/2m^*)(\mathrm{d}^2/\mathrm{d}z^2) + V(z)$. The energy gap of the quantum structure was estimated from the eigenstates thus obtained, assuming the energy band gap of GaAs at 20 K as 1.521 eV.

Examples of the calculated energy gaps are shown in Fig. 6.10, where the dimension of the GaAs well is a parameter and that of the ZnSe barrier used for the calculation of the potential profiles is 110 Å. Here, the valence band offset was 0.6 eV for one side of GaAs and that for another side was taken as a variable, as is the same as Fig. 6.9. It is clearly seen that larger valence band offsets, which induce stronger electric fields (Fig. 6.9), cause the redshift of the energy gap and that its degree depends on the well width. If the pair of the valence band offsets is the same, a wider well weakens the electric field in GaAs as shown in Fig. 6.9. However, the redshift in Fig. 6.10 is more striking with a wider well. Therefore, it can be concluded that the influence of the electric field appears more explicitly in the quantum structure with wider wells. This is well explained in terms of a spatial shift of the electron and the hole wave functions induced by the electric field. The wave functions after the spatial shift, which occurs more easily in wider wells owing to the weak quantum confinement effect, experience the potential valleys and lower the energy states.

In this study, the periodic potential profile like Fig. 6.8 was considered as a first trial. However, actually, the band offset at each interface in a multilayered structure can be designed independently, and besides, the well and barrier widths that influence the

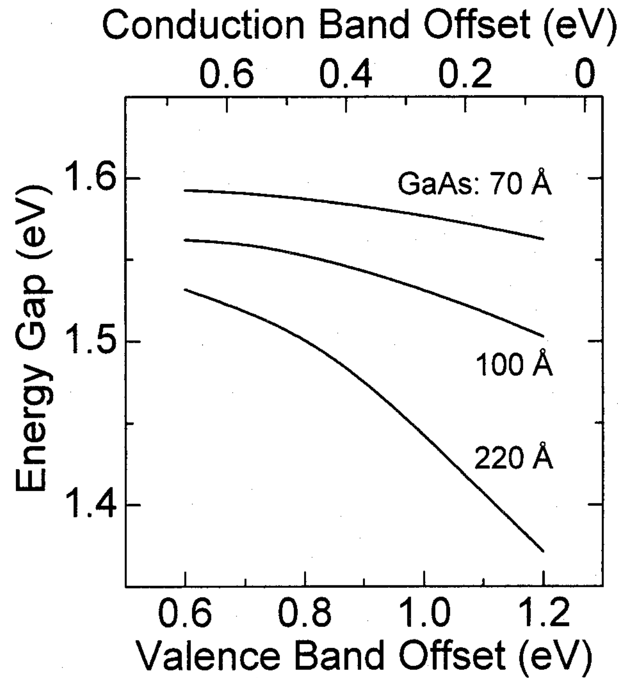

Figure 6.10: Calculated energy gaps as a function of the valence band offset. The dimension of the GaAs well is a parameter and that of the ZnSe barrier used for the calculation of the potential profiles is 110 Å.

intensity of the electric fields are variable. Therefore, various potential profiles can be realized. In this sense, it is crucially important to give a guiding principle for designing the electronic properties of the heterovalent quantum structure. Here, we identify which is most responsible for the redshift, the electric field in the GaAs wells (F_w), that in the ZnSe barriers (F_b), or the band offsets, by examining the contribution of each factor to the energy gap separately. The potential profiles for this calculation were determined irrespectively of the result of the Poisson equation, and the GaAs well width was kept constant at 100 Å.

When F_b was zero and the pair of the valence band offsets was 0.6/1.1 eV, it was found that the energy gap shifted from 1.561 to 1.362 eV by the presence of F_w from 0 to 500 kV/cm, respectively. The positive sign in F_w means that its vector is pointing toward the interface with the valence band offset of 1.1 eV. The redshift was also observed by F_w in the opposite direction, that is, F_w from 0 to -500 kV/cm brought the energy gaps from 1.559 to 1.287 eV, respectively. Under negative F_w, both electron and hole wave functions are pushed to the interfaces with the smaller band offsets, and consequently, penetration into the barrier regions becomes pronounced, compared with that under the positive F_w. This causes the quantitative difference of the energy gaps of 1.362 and 1.287 eV under

±500 kV/cm. However, an important result elucidated by this calculation is that F_w can potentially bring about variation of the energy gap in the order of hundreds meV.

On the other hand, F_b in the range from −500 to 500 kV/cm with zero F_w and the pair of the valence band offsets of 0.6/1.1 eV resulted in a trivial change of the energy gap in the order of sub meV. Although the variation due to F_b is enlarged by the increase of F_w, its order is still meV even with F_w = 500 kV/cm. The reason for the enhancement of the redshift by greater F_w is that the wave functions are spatially shifted toward the well barriers by F_w to be more sensitive to the electric field in the barriers, *i.e.*, F_b.

With respect to the effect of the band offset on the energy gap, the calculation was carried out, keeping the valence band offset at one side of the GaAs well at 0.6 eV and changing that at the other side between 0.6 and 1.1 eV. F_b was assumed to be 0 V/cm. The degree of the energy shift due to control of the band offsets depended on F_w. Larger F_w causes greater energy shift, although, even under F_w of 500 kV/cm, the shift due to the change of the valence band offsets from 0.6 to 1.1 eV was estimated to be only about 15 meV.

The results of these calculations lead us to a conclusion that the offset itself is not important and that the electric field in the GaAs wells (F_w) as a function of the offsets plays a principal role in determining the energy gap.

In the above discussions concerning the potential-energy profiles and the energy eigenstates, the existence of strain, which modifies the energy bands, has been neglected. Here, the validity of this assumption is proved. As verified in Sec. 6.3.2, only the ZnSe layers are distorted tetragonally (coherent growth) in the ZnSe-GaAs quantum heterostructures. Considering the lattice parameter of ZnSe (5.6686 Å) and that of GaAs (5.6533 Å) at room temperature (RT), the strain in ZnSe is compressive. The effect of the compressive strain on the energy band of ZnSe is estimated with the model-solid theory proposed by Van de Walle *et al.* [11, 12]. The detail of the calculation was described in Appendix and here only the result is given. The compressive strain in ZnSe makes the band offsets smaller by 3.6 meV for heavy holes, larger by 10.5 meV for light holes, and larger by 9.0 meV for electrons. Using these values, the Poisson equation was solved again. However, there was entirely no difference in the electrostatic potentials with and without strain. In other words, the change provided to the potential-energy profiles by the strain was only band offsets, and the electric fields in ZnSe and GaAs remained unchanged. This is quite rea-

sonable because, as was mentioned in the previous section, the potential-energy profile is governed chiefly by the difference of the valence band offsets at both interfaces, and the modification of the energy band due to the compressive strain does not alter the difference in the offsets. Then, the Schrödinger equation was solved using the newly calculated potential-energy profile. As is easily deduced, since the electric field in GaAs, which was revealed to be essential for determining energy eigenvalues, is unchanged by the strain, the energy shift seems to be considerably small. Indeed, it was estimated for MQW with 100 Å GaAs to be in the order of meV or less. Compared with the variation of the energy gap shown in Fig. 6.10, this quantity is negligible, which validates the assumption made for the present calculation. We will also neglect the influence of strain on the experimental data.

6.4.2 Optical-absorption measurements

We will move to the discussion on the optical-absorption measurement. For the absorption measurement, the substrate of the samples was removed by a selective NaOH(1N) : H_2O_2 = 1 : 1 (in volume) etching solution at RT. The light from a halogen lamp was irradiated to the samples, and the transmitted light was detected using a cooled charge coupled device (CCD) and a 50-cm monochromator. The intensity of the irradiated light was made as weak as possible so as to avoid unexpected modification of the band alignment due to photogenerated carriers. Under the present experimental setup, no luminescence was observed, and therefore, the detected signals reflect only the absorption properties.

Figure 6.11 shows a typical 22 K absorption spectrum of the ZnSe-GaAs heterovalent quantum structure, which consists of eight periods of 110 Å ZnSe and 100 Å GaAs. The valence band offsets at ZnSe/GaAs and GaAs/ZnSe are 0.6 and 1.1 eV, respectively. Since excitonic absorption peaks were not detected, the following discussion has been done based on the absorption edge, which was defined as the energy determined by extrapolation of linear dependence of the square of the absorbance on irradiated photon energy into zero absorbance. It must be noted that the absorption edge energy ($E_{\rm abs}$) is lower than the energy gap ($E_{\rm g}$) owing to absorption by impurities and/or excitons, that is,

$$E_{\rm abs} = E_{\rm g} - \Delta E_{\rm abs}, \tag{6.9}$$

where $\Delta E_{\rm abs}$ indicates variation caused by the impurity and/or exciton absorption. In this study, however, the contribution from impurities to $\Delta E_{\rm abs}$ is considered to be negligible.

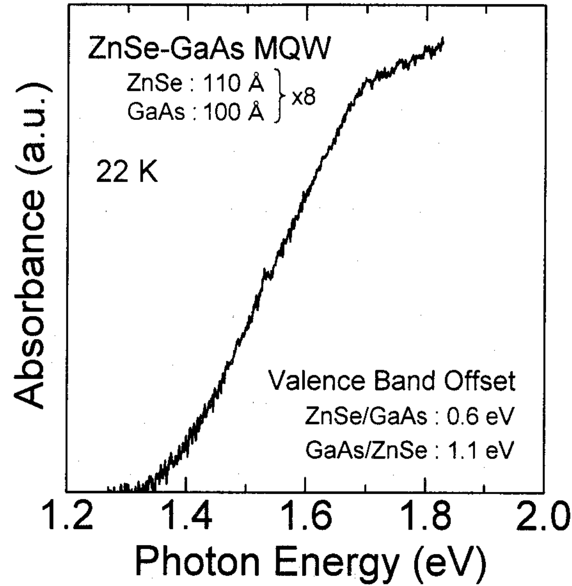

Figure 6.11: Typical absorption spectrum of the ZnSe-GaAs heterovalent quantum structure measured at 22 K. The sample is the eight periods MQW consisting of 110 Å ZnSe and 100 Å GaAs. The valence band offsets at ZnSe/GaAs and GaAs/ZnSe are designed to be 0.6 and 1.1 eV, respectively.

This is because the absorption edge energy of 1150-Å-thick GaAs grown on ZnSe/GaAs was estimated to be 1.518 eV, and the energy difference of 3 meV between the estimated value (1.518 eV) and the energy band gap of GaAs at 20 K (1.521 eV) is close to the exciton binding energy of bulk GaAs (~5 meV). Therefore, in the following, ΔE_{abs} is determined by referring to the exciton binding energies calculated in Ref. [13].

band offset dependence

The absorption edge energies of the MQW's with different pairs of the valence band offsets at both sides of the GaAs wells are compared in Fig. 6.12. The ZnSe barrier thickness was 110 Å for all samples. The valence band offset at the ZnSe/GaAs interface is 0.6 eV as stated before, and that at the GaAs/ZnSe interfaces is a variable indicated at the horizontal axis. Accordingly, for example, the valence band offset of 0.6 eV in the figure means the flatband condition. The result with 220 Å GaAs and the valence band offset of 1.1 eV may be less reliable. Since the electron and hole wave functions are remarkably separated under the structural and physical parameters for this sample [14], the absorption becomes weak, and consequently, the signal-to-noise ratio in the experiment gets worse.

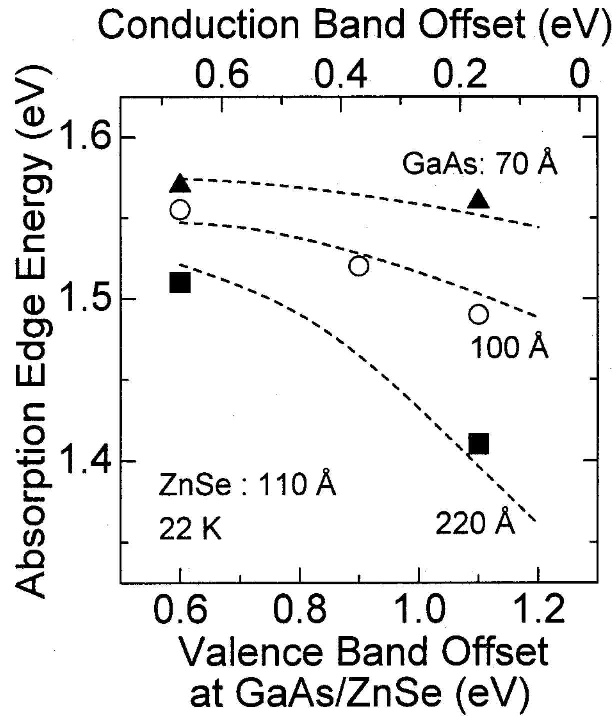

Figure 6.12: The absorption edge energies of the MQW's with different pairs of the valence band offsets at both sides of the GaAs wells. The valence band offset at the ZnSe/GaAs interfaces is constant at 0.6 eV. Thickness of ZnSe is 110 Å for all samples in this figure. The broken lines indicate the theoretically determined absorption energies ($E_{\rm abs}$), which were evaluated by subtracting the exciton binding energies from the energy gaps ($E_{\rm g}$).

It is explicitly seen in Fig. 6.12 that MQW's with larger valence band offsets, which corresponds to larger difference in the valence band offsets at both sides of GaAs, exhibit lower absorption energies and that the redshift becomes more conspicuous in MQW's with wider wells. The broken lines in the figure indicate the absorption energies ($E_{\rm abs}$) calculated from Eq. (6.9), that is, by subtracting $\Delta E_{\rm abs}$ from energy gaps ($E_{\rm g}$) shown in Fig. 6.10. As $\Delta E_{\rm abs}$ in Eq. (6.9), which is equal to the exciton binding energy, 19, 15, and 11 meV were used for MQW's with the well width of 70, 100, and 220 Å, respectively, according to the calculated results in Ref. [13]. It is worth noting that those exciton binding energies are larger than those in the GaAs-AlAs system, owing to the large difference in the dielectric constants between GaAs and ZnSe. Strictly, the exciton binding energy depends on the intensity of the electric field; though, here, it was assumed to be constant at the value without electric fields as a first trial. The reasonable agreement between the experimental results and the theoretical calculations indicates that the electronic properties in the

heterovalent MQW's are well described by the potential profiles shown in Fig. 6.8 and by the energy eigenvalues determined by the profiles. Moreover, it can be concluded that the modification of the exciton binding energy due to the presence of the electric field is within the present experimental resolution. It is interesting to note that the results obtained here prove the capability of controlling the electronic properties of heterovalent MQW's through the control of the band offsets, which differs considerably from isovalent systems.

well width dependence

The quantum confinement effect was examined by the well width dependence of the absorption edges. The samples used for this experiment possess the 110-Å-thick ZnSe barriers. Two series of the samples, that is, with and without difference between the band offsets at both sides of GaAs, were investigated. For the former, the valence band offsets at the ZnSe/GaAs and the GaAs/ZnSe interfaces are 0.6 and 1.1 eV, respectively, which yields the internal electric field. In the latter case, both valence band offsets are 0.6 eV, and thus, there is no electric field.

The results are shown in Fig. 6.13. The broken lines are the theoretically calculated absorption energies with the consideration of the exciton binding energies. Similar to Fig. 6.12, the fairly good agreement between the experiment and the calculation was attained, indicating the achievement of the quantum confinement. Furthermore, it is clearly observed from either the experiment or the calculation that, as the well width is widened, the variation of the energy gap due to the electric field becomes pronounced, as was already pointed out in Sec. 6.4.1. The results here support the conclusion from the band offset dependence of the absorption properties that the electronic properties of heterovalent MQW's are controllable through the interface control.

barrier width dependence

Finally, we describe the barrier width dependence. With decreasing the barrier width, quantum structures are generally converted from MQW's to superlattices in which the wave functions in wells interact with each other to form minibands. In the conventional isovalent quantum structures, formation of the minibands due to the conversion from MQW's to superlattices appears in the absorption properties as a lowered absorption edge. Our interest is what is observed in the heterovalent quantum structures by changing the barrier

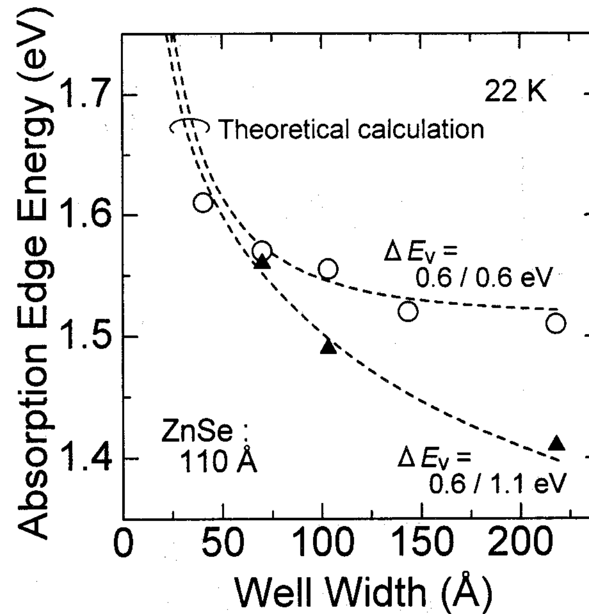

Figure 6.13: Well width dependence of the absorption edges. The ZnSe barriers are 110-Å thick. The pair of the valence band offsets (ΔE_v) at both sides of GaAs is used as a parameter. The broken lines are the theoretically calculated absorption energies with the consideration of the exciton binding energies.

width. In order to elicit the difference between the isovalent and heterovalent quantum structures, different valence band offsets of 0.6 and 1.1 eV were set at the ZnSe/GaAs and the GaAs/ZnSe interfaces, respectively. The dimension of the GaAs wells was 100 Å.

Before showing the experimental details, the theoretical analyses are briefly performed. First, the miniband structures were calculated by the Kronig-Penny model assuming the quantum structures without electric fields. It was demonstrated that the first miniband for electrons was formed with barriers less than 70-Å thick and that its width with the barrier width of 30 Å was 1.5 meV. Since the presence of an electric field localizes carriers and prevents the formation of the minibands, the result above suggests that the calculation process of the Schrödinger equation employed in this study does not include a serious error for the multiple quantum structures with barriers thicker than 70 Å. For superlattices with barriers thinner than 70 Å, the quantitative accuracy is surely degraded, although it is still possible to extract the trend of the energy states against the barrier width by the same technique. This is because the variation of the energy levels due to the conversion into superlattices, that is, due to the formation of the minibands, is relatively small as was estimated to be 1.5 meV for the 30-Å-thick barriers. Thus, we calculated energy

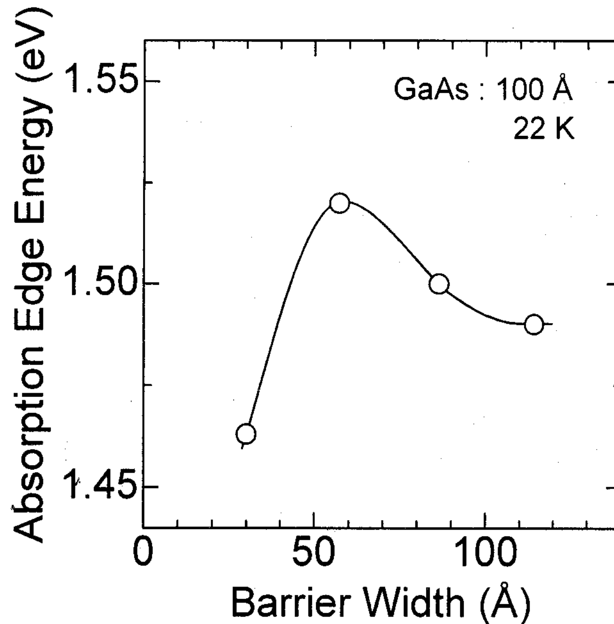

Figure 6.14: Barrier width dependence of the absorption edges. The dimension of GaAs is 100 Å. The originally designed valence band offsets at ZnSe/GaAs and GaAs/ZnSe are 0.6 and 1.1 eV, respectively.

levels even for the superlattices using the same procedure. Consequently, it was found that as the barrier width was reduced from 110 to 30 Å, the electric field in the GaAs regions became stronger and the energy gap shifted monotonously from 1.518 to 1.444 eV. Namely, the theoretical prediction is that redshift will be observed also in heterovalent systems by reducing the barrier width, though that is predominantly caused by the internal electric field, differing from isovalent systems. The redshift due to formation of the minibands will be too small to be observed.

Experimentally, however, the absorption edge energies behaved contrary to the theoretical prediction as shown in Fig. 6.14. As the barrier width decreases from 110 Å, it is once shifted toward higher energy, and then shows the redshift below 50 Å. The observed blueshift due to the decrease in the barrier layer thickness cannot be interpreted by the theoretical analyses so far performed in this study, and therefore, another factor must be considered. According to Figs. 6.9 and 6.10, the blueshift means that the difference of the valence band offsets at both sides of the GaAs wells got smaller to weaken the electric field in GaAs. As a cause for this, we consider at present the charge transfer within the ZnSe region. Let us explain this model using Fig. 6.15. The tunability of the band offsets

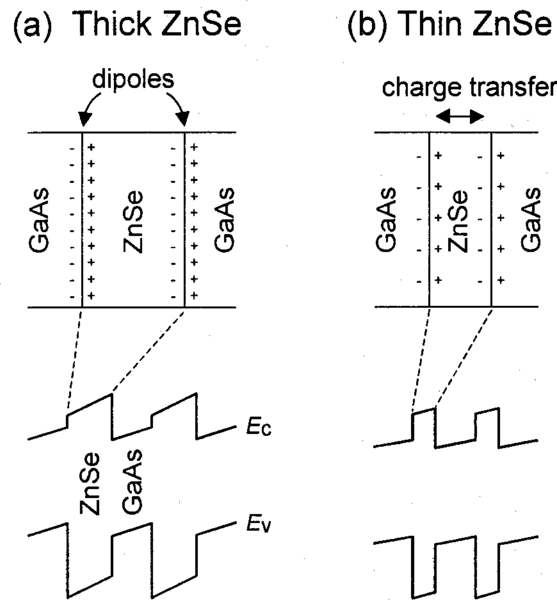

Figure 6.15: A model for the blueshift observed in the barrier width dependence of the absorption edges.

being utilized here is based on the formation of the electronic dipoles at the interface, as described in chapters 3 and 5. These electronic dipoles originate from the charge transfer from donating Ga-Se bonds to accepting Zn-As bonds across the interface. If the ZnSe and GaAs layer thicknesses are relatively thick and each interface is isolated, these dipoles are preserved even after the alternating deposition of ZnSe and GaAs, and the optical properties agree reasonably well with the theoretical calculation as shown in Figs. 6.12 and 6.13. This situation and the resultant potential profile are schematically illustrated in Fig. 6.15(a). In this figure, taking the results of chapters 3 and 5 into account, the dipoles for the valence band offset of 0.6 eV are directed to ZnSe and those for 1.1 eV to GaAs. Thin ZnSe, on the other hand, facilitates the interaction between interfaces and promotes the charge transfer from one side to the other side of the ZnSe barrier. As a result of this charge rearrangement within the ZnSe region, the dipoles at both interfaces tend to weaken each other, which makes the difference of the valence band offsets small as shown in Fig. 6.15(b). Since the small difference of the offsets weakens the electric fields, the absorption energy is shifted toward higher energy. This is the reason for the blueshift observed in Fig. 6.14.

In the above discussion with Fig. 6.15, the sign of the charges at both sides of ZnSe was opposite and the dipoles were in the same direction. However, the discussion can be

extended to the dipoles with arbitrary direction. If the dipoles are in the opposite direction with different strength, the charge transfer occurs from the side with higher charge density to that with lower charge density, and the difference in strength of the dipoles becomes small. Therefore, similar to Fig. 6.15, the electric field is weaker in the quantum structures with narrower barriers, which causes blueshift.

With respect to the redshift below 50 Å, the theoretical analyses stated previously in this section suggest that this is probably due to the electric field. This is because the amount of the observed redshift is 50 – 60 meV, which is much closer to the calculated redshift of ~30 meV than to the width of the first miniband. The reason why the effect of the electric field appears explicitly in the quantum structures with barriers thinner than 50 Å is considered as follows. The final charge distribution is determined not only by the ZnSe thickness but also by other factors such as the charges at the GaAs side of the interfaces and the donor and acceptor bonds at the interfaces. In Fig. 6.14, the charge transfer due to the decrease in the ZnSe thickness will be completed at about 50 Å, and the electric field remained after the charge transfer is strengthened by thinning the barrier width and causes the redshift.

Although the similar charge transfer must take place in the GaAs wells by reducing the GaAs well width, observation of this phenomenon will be difficult because the influence of the electric field on the absorption energy is originally not so remarkable in narrow wells as shown in Fig. 6.13.

The barrier width dependence shown here is one of the unique characteristics of the heterovalent quantum structures, which is never observed with the conventional isovalent systems.

6.5 Summary

ZnSe-GaAs(001) heterovalent quantum structures were fabricated, and their optical properties were assessed by the absorption measurement at 22 K. Dependence of the absorption edge energy on the offsets, the well width, and the barrier width was investigated. The absorption edges were shifted toward lower energy by enlarging the difference of the valence band offsets at both sides of the GaAs wells. This was an indication of the presence of the internal electric field. The well width dependence also provided evidence of the

presence of the electric field. The theoretical calculation of the Poisson and Schrödinger equations well explained these experimental results. In contrast, the barrier width dependence exhibited the anomalous behavior and could not be expressed by the theoretical analyses. This unique characteristic was interpreted in terms of the charge transfer within the barrier region.

References

[1] D. A. B. Miller, D. S. Chemla, T. C. Damen, A. C. Gossard, W. Wiegmann, T. H. Wood, and C. A. Burrus, Phys. Rev. B **32**, 1043 (1985).

[2] E. E. Mendez, F.Agulló-Rueda, and J. M. Hong, Phys. Rev. Lett. **60**, 2426 (1988).

[3] From the analysis of the interference fringe appearing between the Bragg peaks, the thickness fluctuation from period to period was estimated to be as small as 1 – 2 monolayers. For more details, see M. Funato, Sz. Fujita, and Sg. Fujita, Jpn. J. Appl. Phys. **32**, 3396 (1993).

[4] W. Ehrenberg, Proc. Phys. Soc. A **63**, 75 (1950).

[5] A. H. Kachare and W. G. Spitzer, J. Appl. Phys. **45**, 2938 (1974).

[6] G. E. Stillman, C. M. Wolfe, and J. O. Dimmock, in *Semiconductors and Semimetals*, edited by R. K. Willardson and A. C. Beer, Vol. 12 (Academic Press, Inc. New York, 1977), p. 169.

[7] R. A. Stradling, Phys. Lett. **3**, 217 (1966).

[8] P. J. Dean, D. C. Herbert, C. J. Werkhoven, B. J. Fitzpatrick, and R. N. Bhargava, Phys. Rev. B **23**, 4888 (1981).

[9] Calculated from the Luttinger parameters given in P. Lawaetz, Phys. Rev. B **4**, 3460 (1971).

[10] G. Bastard, E. E. Mendez, L. L. Chang, and L. Esaki, Phys. Rev. B **28**, 3241 (1983).

[11] C. G. Van de Walle and R. M. Martin, Phys. Rev. B **34**, 5621 (1986).

[12] K. Shahzad, D. J. Olego, and C. G. Van de Walle, Phys. Rev. B **38**, 1417 (1988).

[13] M. Kumangai and T. Takagahara, Phys. Rev. B **40**, 12359 (1989).

[14] The overlap integral between electron and hole wave functions was calculated to be about 10% of that without electric field.

Chapter 7

Conclusions

This study aimed at exploring the potential of heterovalent heterostructures, which are characterized by electron-excess and electron-deficient bonds at the interfaces, for future applications in optoelectronics. For this purpose, we investigated (1) how to fabricate the heterostructures and (2) how to control the interface properties, and attempted to extract characteristics originating from heterovalency. As the material combination to be studied, the ZnSe-GaAs heterovalent but lattice matched heterostructure was chosen. The growth characteristics during metalorganic vapor phase epitaxy (MOVPE) were clarified and the procedures to tune the band offsets were established in both the ZnSe-on-GaAs (ZnSe/GaAs) and the GaAs-on-ZnSe (GaAs/ZnSe) heterostructures. Using this tunability of the band offsets, the control of the optical properties in the ZnSe-GaAs multilayered quantum structures was accomplished. It should be noted that the tunability of the band offsets and the corresponding tunability of the optical properties cannot be achieved by conventional isovalent material systems. The obtained results are summarized as follows.

In chapter 2, the MOVPE growth of ZnSe/GaAs was described. The growth of ZnSe on the atomically flat GaAs surface was in either the two-dimensional (2D) or the three-dimensional (3D) mode, depending chiefly on the growth temperature. In particular, the growth temperature of 450°C provided atomically flat surfaces, which were favorable surfaces for the atomic level control of the interface and were used in chapter 3. The variation of the growth mode was explained in terms of surface diffusion and desorption of atoms being on the growing surface. Subsequently, the initial nucleation processes during the growth at 450°C were investigated, which turned out to depend on the source precursor starting the ZnSe growth. The cause for this phenomenon was ascribed to the difference of the interface structures. However, the 2D growth was preserved irrespectively of the starting precursors,

different from the molecular beam epitaxy (MBE) in which the Se-initiated growth brings the 3D growth. By increasing the thickness, by which the quasi-homoepitaxial growth is realized, the 2D layer-by-layer growth was clearly observed.

In chapter 3, tunability of the band offsets in ZnSe/GaAs was demonstrated. That was successfully achieved by controlling the local interface composition by means of the Zn- or Se-exposure, or thermal etching of the GaAs surfaces followed by ZnSe growth. The variation of the valence band offsets ranged from 0.6 to 1.1 eV. The surfaces of the ZnSe thin films were kept to be atomically flat, which is indicative of the atomic level control of the interface atomic configuration. In order to elucidate the mechanism for the control of the band offsets, the interface properties were examined structurally by x-ray crystal truncation rod (CTR) scattering measurements and optically by photoreflectance measurements. It was revealed that interdiffusion within a few monolayers (1 monolayer = 2.8 Å) formed the electronic dipoles and that the dipoles bent the energy-band very steeply in the vicinity of the interface. This band-bending, that is, electric field, induced by the dipoles exhibited a strong correlation with the band offsets estimated by x-ray photoemission spectroscopy (XPS), indicating its responsibility for the tunability of the band offsets.

In chapter 4, the MOVPE growth procedures of GaAs/ZnSe were established. First, the flow sequences of the source precursors for GaAs were optimized. The Ga precursor decomposed into Ga metal and deposited three-dimensionally on ZnSe, indicating that the GaAs growth on ZnSe should not be initiated with the Ga precursor. The As precursor, on the other hand, etched ZnSe drastically. The etching mechanism was considered to be related to the formation and evaporation of Zn_3As_2 and As_xSe_{1-x}. With respect to the growth behavior of GaAs on ZnSe, it was found that the behavior strongly depended on the growth conditions such as the V/III ratio and the growth temperature. This was attributed to migration of Ga atoms and/or Ga-related molecules; high growth temperatures ($\geq$ 550°C) and low V/III ratios ($\leq$ 5), which promote migration, resulted in the 3D Volmer-Weber growth mode, while low growth temperatures ($\leq$ 500°C) or high V/III ratios ($\geq$ 10) brought 2D growth. In particular, the surfaces of GaAs grown at 400 or 450°C were atomically flat. The realization of the 2D growth at 400 – 450°C in MOVPE makes a striking contrast to the MBE growth in which the flat GaAs surfaces cannot be obtained without extremely lowering the growth temperature. The variation of the growth modes was applied to fabrication of the ZnSe-GaAs quantum structures with fractional

dimensionality.

In chapter 5, control of the band offsets in GaAs/ZnSe was successfully attained. The etching properties of ZnSe in a hydrogen ambient and in an As precursor ambient were applied to modify the interface atomic configuration. By changing the durations of the etching, the variation of the valence band offset from 0.6 to 1.1 eV was achieved, which was interpreted in terms of the layer-by-layer fashion of the etching. In particular, the etching in the As ambient resulted in the periodic change of the band offsets. This indicated that Zn and Se atoms appeared alternately on the ZnSe surface as a result of the layer-by-layer etching and strongly supported the above interpretation. The surface of GaAs/ZnSe was maintained to be atomically flat during this experiment, which proved the control of the interface atomic configuration in the atomic level.

In chapter 6, the ZnSe-GaAs heterovalent quantum structures were fabricated and their optical properties originating from heterovalency were characterized. By using the results from chapters 2 and 4, the structurally well-defined quantum structures could be fabricated. Thus, we could attribute the observed variation of the optical properties to the control of the band offsets, which was achieved in chapters 3 and 5, without consideration of the influence from structures. The optical properties were characterized by absorption measurements. The optical-absorption edges were shifted toward lower energies by enlarging the difference of the valence band offsets at both sides of the GaAs wells, indicating the presence of the internal electric field. The theoretical prediction based on the Poisson and Schrödinger equations agreed well with the experimental results. It must be noted that this result eloquently illustrates the capability of controlling the optical properties of the quantum structure without changing its structure. Regarding the barrier width dependence, the optical-absorption properties exhibited anomalous behavior that could not be explained by the theoretical analyses. This unique characteristic in the heterovalent quantum structures was ascribed to the charge transfer within the barrier region.

We believe that the present study could contribute to development of the heterostructures in a novel category; the heterovalent heterostructures. Here, for future studies, several suggestions are given. (1) The application of the controllability of the band offsets shown in chapter 6 is a preliminary example. Other applications such as optical switches operated by a light, in which the third-order optical nonlinearity due to the internal electric field is used, might be possible. (2) The properties peculiar to the heterovalent heterostructures

are originating from the interface bonds. In this sense, the introduction of atoms different from the constituents of a heterostructure to the interface may bring novel properties. (3) The material combination studied here was ZnSe-GaAs, although the guiding principle presented in this study can be applied to other lattice-matched heterovalent heterostructures such as ZnSe-Ge, ZnS-GaP, cubic-GaN/3C-SiC, and so on. The studies on those subjects (1) – (3) will successfully expand applicable fields of the heterovalent heterostructures.

Appendix

Band Edges under Strain

For the particular case of ZnSe grown coherently on GaAs along the [001] direction, the strain tensors ϵ_{ij}'s are expressed as

$$\epsilon_{xx} = \epsilon_{yy} = \epsilon = \left(\frac{a_{\mathrm{GaAs}} - a_{\mathrm{ZnSe}}}{a_{\mathrm{ZnSe}}}\right), \tag{A.1}$$

$$\epsilon_{zz} = -2\left(\frac{C_{12}}{C_{11}}\right)\epsilon, \tag{A.2}$$

$$\epsilon_{xy} = \epsilon_{yz} = \epsilon_{zx} = 0, \tag{A.3}$$

where $z \parallel [001]$, a is the bulk lattice parameter of the indicated material, and C_{ij}'s are the elastic stiffness constants. Based on the model solid theory [1, 2], the variations of the conduction band edge ($\delta E_{\mathrm{c}}^{\mathrm{s}}$) and the valence band edges for heavy holes ($\delta E_{\mathrm{v,hh}}^{\mathrm{s}}$) and light holes ($\delta E_{\mathrm{v,lh}}^{\mathrm{s}}$) due to such a biaxial in-plane strain are given by

$$\delta E_{\mathrm{c}}^{\mathrm{s}} = E_{\mathrm{hc}}, \tag{A.4}$$

$$\delta E_{\mathrm{v,hh}}^{\mathrm{s}} = E_{\mathrm{hv}} - E_{\mathrm{s}}, \tag{A.5}$$

$$\delta E_{\mathrm{v,lh}}^{\mathrm{s}} = E_{\mathrm{hv}} - \frac{1}{2}\Delta_0 + \frac{1}{2}E_{\mathrm{s}} + \frac{1}{2}(\Delta_0^2 + 2\Delta_0 E_{\mathrm{s}} + 9E_{\mathrm{s}}^2)^{\frac{1}{2}}, \tag{A.6}$$

where

$$E_{\mathrm{hc}} = a_{\mathrm{c}}(\epsilon_{xx} + \epsilon_{yy} + \epsilon_{zz}) = 2a_{\mathrm{c}}\left(1 - \frac{C_{12}}{C_{11}}\right)\epsilon,$$

$$E_{\mathrm{hv}} = a_{\mathrm{v}}(\epsilon_{xx} + \epsilon_{yy} + \epsilon_{zz}) = 2a_{\mathrm{v}}\left(1 - \frac{C_{12}}{C_{11}}\right)\epsilon,$$

$$E_{\mathrm{s}} = b(\epsilon_{zz} - \epsilon) = -b\left(1 + 2\frac{C_{12}}{C_{11}}\right)\epsilon,$$

Δ_0 is the spin-orbit splitting, a_{c} and a_{v} are hydrostatic deformation potentials of the conduction band and the valence band, respectively, and b is uniaxial deformation potential.

Table A.1: Physical parameters in ZnSe.

Deformation potential (eV)			Spin-orbit splitting (eV)	Elastic constant (10^6 kg·cm^{-2})		Lattice parameter (Å)	
a_c	a_v	b	Δ_0	C_{11}	C_{12}	ZnSe	GaAs
−4.17	1.65	−1.2	0.43	0.826	0.498	5.6686	5.6533

The physical parameters in ZnSe were listed in Table A.1, which are the same as those in Ref. [2]. Using those parameters, the variations of the band edges were calculated to be $\delta E_c^s = 9.0$ meV, $\delta E_{v,hh}^s = 3.6$ meV, and $\delta E_{v,lh}^s = -10.5$ meV. Note that the positive sign means the increase in energy. Therefore, as shown in Fig. A.1, the conduction band offset (ΔE_c) is increased by the compressive strain and the valence band offsets (ΔE_v) for heavy holes and light holes are decreased and increased, respectively.

References

[1] C. G. Van de Walle and R. M. Martin, Phys. Rev. B **34**, 5621 (1986).

[2] K. Shahzad, D. J. Olego, and C. G. Van de Walle, Phys. Rev. B **38**, 1417 (1988).

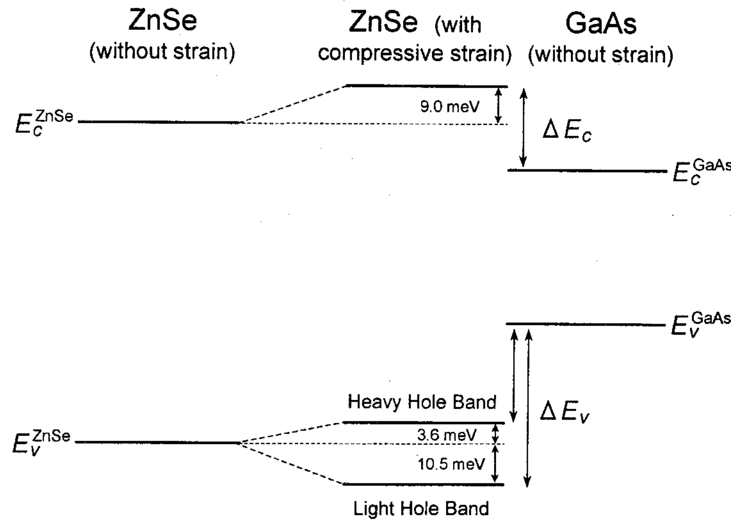

Figure A.1: Schematic illustration of the variation of the energy band diagram due to the compressive strain in ZnSe.

Addendum

List of Publications

I. Full length papers and letters

(1) "Metalorganic vapor phase epitaxial growth and characterization of ZnSe-GaAs multilayered structures"
M. Funato, M. Ishii, P. A. Murawala, O. Tsuji, Sz. Fujita, and Sg. Fujita
J. Crystal Growth **117**, 543 (1992).

(2) "Structural analysis of ZnSe-GaAs quantum wells"
M. Funato, Sz. Fujita, and Sg. Fujita
Jpn. J. Appl. Phys. **32**, 3396 (1993).

(3) "Metalorganic vapor phase epitaxial growth of GaAs on ZnSe; on the flow sequence of source precursors at the interface"
M. Funato, Sz. Fujita, and Sg. Fujita
J. Crystal Growth **145**, 616 (1994).

(4) "Growth behavior of GaAs in metalorganic vapor phase epitaxy onto ZnSe"
M. Funato, Sz. Fujita, and Sg. Fujita
Jpn. J. Appl. Phys. **33**, 4851 (1994).

(5) "MOVPE growth and characterization of ZnSe-GaAs heterovalent heterostructures"
M. Funato, Sz. Fujita, and Sg. Fujita
Bulletin of Materials Science **18**, 343 (1995).

(6) "Formation of an atomically flat surface of ZnSe on GaAs (001) by metalorganic vapor phase epitaxy"

M. Funato, S. Aoki, Sz. Fujita, and Sg. Fujita
Jpn. J. Appl. Phys. **36**, L4 (1997).

(7) "Initial growth behavior of GaAs on ZnSe in MOVPE"
M. Funato, S. Aoki, Sz. Fujita, and Sg. Fujita
J. Crystal Growth **170**, 276 (1997).

(8) "Tunable band offsets in ZnSe/GaAs heterovalent heterostructures grown by metalorganic vapor phase epitaxy"
M. Funato, S. Aoki, Sz. Fujita, and Sg. Fujita
J. Appl. Phys. **82**, 2984 (1997).

(9) "Nucleation processes during metalorganic vapor phase epitaxy of ZnSe on GaAs(001)"
M. Funato, S. Aoki, Sz. Fujita, and Sg. Fujita
J. Appl. Phys. **84**, 1383 (1998).

(10) "Observation of high electric field at ZnSe/GaAs heterointerfaces by fast Fourier transformed photoreflectance"
J. Nukeaw, Y. Fujiwara, Y. Takeda, M. Funato, S. Aoki, Sz. Fujita, and Sg. Fujita
Thin Solid Films **334**, 11 (1998).

(11) "Tunable band offsets via control of interface atomic configuration in GaAs-on-ZnSe(001) heterovalent heterostructures"
M. Funato, S. Aoki, Sz. Fujita, and Sg. Fujita
J. Appl. Phys. **85**, 1514 (1999).

(12) "Energy states in ZnSe-GaAs heterovalent quantum structures"
M. Funato, Sz. Fujita, and Sg. Fujita
Phys. Rev. B **60**, 16652 (1999).

(13) "Engineered interface properties in ZnSSe/GaAs heterovalent heterostructures"
M. Funato, Sz. Fujita, and Sg. Fujita
J. Crystal Growth (accepted).

II. Conference Proceedings

(1) "Fabrication of short period ZnSe-GaAs superlattices by MOVPE"
M. Funato, Sz. Fujita, and Sg. Fujita
Proceedings of the 1992 MRS Fall meeting **281**, 573 (1993).

(2) "Formation of ZnSe/GaAs heterovalent heterostuctures by MOVPE"
M. Funato, S. Aoki, Sz. Fujita, and Sg. Fujita
Proceedings of the 1996 MRS Fall meeting **448**, 107 (1997).

(3) "Monolayer scale analysis of ZnSe/GaAs heterointerface structures by x-ray CTR scattering and interference"
Y. Takeda, K. Fujita, M. Tabuchi, M. Funato, S. Aoki, Sz. Fujita, and Sg. Fujita
Proceedings of the 24th Intern. Symp. Compound Semiconductors (Inst. of Phys., Bristol & Philadelphia, 1998), p. 263.

(4) "Optical absorption in ZnSe-GaAs heterovalent quantum structures"
M. Funato, Sz. Fujita, and Sg. Fujita
Proceedings of the 1998 MRS Fall meeting **535**, 71 (1999).

III. Review articles

(1) "Tunable band discontinuity in ZnSe/GaAs heterovalent heterostructures"
M. Funato, Sz. Fujita, and Sg. Fujita
Oyo Butsuri **66**, 161 (1997). [in Japanese]

IV. Related publications

(1) "Relation between phase stability and mechanical defects in InGa(Al)As/GaAs and ZnSe/GaAs heterostructures under pressure"
T. M. Ritter, B. A. Weinstein, H. M. Kim, C. R. Wie, K. Stair, C. Choi-Feng, and M. Funato
J. Phys. Chem. Solids **56**, 607 (1995).

(2) "Growth of p-type ZnSe by metalorganic molecular beam epitaxy using metal Zn and dimethylselenide"

J. Suda, M. Tsuka, D. Honda, M. Funato, Y. Kawakami, Sz. Fujita, and Sg. Fujita
J. Electron. Mater. **25**, 223 (1996).

(3) "Effects of GaAs buffer layer and lattice-matching on deep levels in Zn(S)Se/GaAs heterostructures"
M. Funato, H. Kitani, Sz. Fujita, and Sg. Fujita
J. Electron. Mater. **25**, 217 (1996).

(4) "A comparative study on deep levels in p-ZnSe grown by MBE, MOMBE and MOVPE"
M. Funato, Sz. Fujita, and Sg. Fujita
J. Crystal Growth **184/185**, 495 (1998).

(5) "Deep states in nitrogen-doped p-ZnSe"
M. Funato, Sz. Fujita, and Sg. Fujita
J. Appl. Phys. **83**, 2563 (1998).